HUMAN HEAD TEMPERATURE AND ELECTRIC FIELD INVESTIGATIONS UNDER ECT

A Thesis submitted by

Marília Menezes de Oliveira, M Eng

For the award of

Doctor of Philosophy

2017

Abstract

Electroconvulsive therapy (ECT) is a non-invasive technique used to treat psychiatric conditions. A high strength low frequency electrical stimulation is delivered through two electrodes. The aim of this work is to develop an ECT finite element human head model to investigate the electric field and the increase in temperature due to the electrical stimulation.

The bio-heat transfer equation combined with Laplace equation and their initial and boundary conditions are used to define the physics of the models. Firstly, finite element spherical human head models are created in COMSOL Multiphysics and the behaviour of the thermal field due to ECT electrical stimulation is analysed. Heterogeneity was considered and thermal anisotropy of the skull layer was applied to the finite element models.

Secondly, a realistic human head model is created using magnetic resonance images (MRI). Similar physics is applied to define the thermal and electrical problems, and the anisotropic conductivity of the skull is considered. The realistic models contain anatomical features and realistic tissue conductive properties. Through these models we investigate the role of stimulation parameters such as: electrode montages, strength of stimulation, temperature behaviour, etc. Later on, another realistic human head model with a brain tumor is created and a diffusion tensor image is included. Based on this model the white matter anisotropy is considered and the effect on the electric field is analysed.

The results show that high temperatures only occur on external areas of the head, such as scalp and fat. The thermal conductivity anisotropy is insignificant from a heat-transferring point of view. However, the electrical anisotropy does need to be included in order to get more accurate outcomes. If ECT was applied to a patient

with a brain tumor, then factors such as tumor location, aggressiveness, electrode montage, etc would need to be considered. Further work can be undertaken through computational simulation to make personal ECT treatment feasible in clinical practice.

Certification of Thesis

This thesis is entirely the work of __*Marilia Menezes de Oliveira*__ except where otherwise acknowledged. The work is original and has not previously been submitted for any other award, except where acknowledged.

Student and supervisors signatures of endorsement are held at USQ.

Peng (Paul) Wen

Principal Supervisor

Tony Ahfock

Associate Supervisor

Yan Li

Associate Supervisor

Acknowledgement

As the latest stage of my educational journey, it is with great pleasure that I would like to acknowledge the kind people who supported me during my bittersweet days.

Firstly, I am thankful to God to give me this opportunity and to Whom I always got strength and Who always makes my way more bright. I am extremely grateful to my principal supervisor, A/Prof. Peng (Paul) Wen. Without his support, encouragement, respect and patience, it would not have been possible to finish. Also, I am extremely thankful to my associate supervisor, A/Prof. Tony Ahfock, for his guidance, encouragement and support, even during late hours. I would like to thank A/Prof Yan Li for her support. I would like to acknowledge the technical and administrative support of the Faculty of Health, Engineering and Sciences and the RedTrain. I would also like to thank my friends and colleagues for their support and encouragement. I would like to thank my financial sponsor, CNPq - Brazil through the Science without Borders.

My special gratitude goes to my parents and my brother, who always gave me unconditional love and support and always believed in me.

List of related publications

The following papers, associated with the research contained in this dissertation, have been published.

JOURNAL PAPERS

OLIVEIRA, M. M.; WEN, P.; AHFOCK, T., 2016. Heat transfer due to electroconvulsive therapy: Influence of anisotropic thermal and electrical skull conductivity. *Computer Methods and Programs in Biomedicine, 133,* 71-81.

SHAHID, S.S. ; SONG, B. ; SALMAN, H. ; **OLIVEIRA, M. M.** ; WEN, P., 2015. Use of electric field orientation as an index for estimating the contribution of model complexity in tdcs forward head model development. *IET Science, Measurement & Technology, 9*(5), 596-605.

PEER-REVIEWED CONFERENCE PAPERS

OLIVEIRA, M. M.; WEN, P.; AHFOCK, T., (2016, October). Bio-heat transfer model of electroconvulsive therapy: Effect of biological properties on induced temperature variation. In *Engineering in Medicine and Biology Society (EMBC), 2016 IEEE 38th Annual International Conference of the* (pp. 3997-4000). IEEE.

OLIVEIRA, M.M.; WEN, P.; AHFOCK, T.; SHAHID, S.S., 2014. 'A Preliminary Study about the Distribution of Temperature Due to Electrical Stimulation in ECT', in International Conference on Complex Medical Engineering: proceedings of the International Conference on Complex Medical Engineering (ICME CME 2014),Taipei, Taiwan.

JOURNAL MANUSCRIPTS UNDER REVIEW/SUBMITTED

OLIVEIRA, M. M.; WEN, P.; AHFOCK, T.. ‘ECT Electrical Field when in the Presence of a Brain Tumor’. Submitted to the journal Physics in medicine and biology.

Contents

Abbreviations

In alphabetical order:

1D	One dimensional
2D	Two dimensional
3D	Three dimensional
AXM_2D	2D axisymmetric model
BC	Boundary condition
BET	Brain extraction tool
BF	Bifrontal
BHTE	Bio-heat transfer equation
BL	Bilateral frontotemporal
CSF	Cerebro-spinal fluid
CT	Computed tomography
DBS	Deep brain stimulation
DC	Direct current
DICOM	Digital imaging and communications in medicine
DTI	Diffusion tensor image
EA	Electroanesthesia
ECS	Electroconvulsive shock
ECT	Electroconvulsive therapy

E-field	Electric field
E_{med}	Median electric field
ES	Electrosleep
FAST	FMRIB's automated segmentation tool
FDM	finite difference method
FE	Finite element
FEAST	Focal electrically administered seizure therapy
FEM	Finite element methods
FEM_3D	3D FEM spherical model
FIRST	FMRIB's integrated registration and segmentation tool
FLIRT	FMRIB's linear image registration tool
FNIRT	FMRIB's non-linear image registration tool
FSL	FMRIB's software library
GM	Grey matter
GradT	Gradient of temperature
IC	Initial condition
ICBM	International consortium for brain mapping
LOL	Left occipital lobe
MRA	Magnetic resonance angiography
MRI	Magnetic resonance image
NIfTI	Neuroimaging informatics technology initiative
PD	Proton density
RCN_1D	1D resistive-capacitive network model
RCN_3D	3D resistive-capacitive network model
RE	Relative error
RFA	Radiofrequency ablation

RFL	Right frontal lobe
RHM	Realistic head model
RHM_06	Realistic human head model – 6 layers
RHM_17	Realistic human head model – 17 layers
ROI	Region of interest
RUL	Right unilateral
SHM	Spherical head model
SHM_04	Spherical human head model - 4 layers
SHM_05	Spherical human head model - 5 layers
SHM_06	Spherical human head model - 6 layers
T	Temperature
T1w	T1-weighted
T2w	T2-weighted
T_{amb}	External temperature
tACS	Transcranial alternating current stimulation
TE	Echo time
tES	Transcranial electrical stimulation
T_{max}	Maximum temperature
TR	Repetition time
tRNS	Transcranial random noise stimulation
tSDCS	Transcranial sinusoidal direct current stimulation
TTField	Tumor treating fields
VC	Volume constraint
WM	White matter

List of Figures

List of Tables

"If you realized how powerful your thoughts are, you would never think a negative thought."

(Peace Pilgrim)

1. INTRODUCTION

1.1. Background

The human brain is the most interesting and unknown organ in the human body. It lies in the cranium, being protected by the skull. The brain gives commands to and receives requests from the entire body through connections among the trunk and limbs through the spinal cord (Standring 2015). It can mainly be divided into frontal, temporal, parietal, occipital and insula.

The human brain is always incognito and it is common to find people with some kind of neurological issues, where frequently, the problem is unknown and the treatment is difficult. Pharmacotherapy is normally used to treat brain diseases, but this is not always effective and, can sometimes cause other problems. Another type of treatment which has been used for decades is transcranial electrical stimulation (tES), where a stimulus is delivered to the scalp or inside the head, directly to the brain. As in all kinds of treatment, side effects can also happen, but studies and practices have demonstrated good, promising and efficient results in many cases.

Transcranial electrical stimulation has been used to treat neurological diseases for many years. These therapies range from non-invasive techniques, such as transcranial direct current stimulation (tDCS), which applies low intensity direct current to the scalp; and invasive techniques, such as deep brain stimulation (DBS), where electrodes are implanted in specific regions of the brain. A variety of therapies have been developed over time. Each treatment has its own unique and fundamental characteristics, and the therapy varies in intensity, duration, frequency and continuity, among other factors.

One of these treatments, which has been used since the 1930s (Guleyupoglu et al. 2013) is known as electroconvulsive therapy (ECT). There are many polemics in the use of this technique, because whereas some people say that this technique can treat and help extreme cases of neurological diseases, others say that this technique is too aggressive, with significant side effects and its use should be ceased. With the purpose of trying to demystify, better understand and make it safer, the focus of this study is on this therapy.

All these techniques use electrical current input and, in the case of electroconvulsive therapy high current is used, so particular care should be taken. As we know, when electrical current passes through a conductor, heat is generated. Temperature (T) increases due to Joule heating and metabolic responses which are a result of electrical stimulation of tissues (Datta, Elwassif & Bikson 2009; Elwassif et al. 2006). Electrical stimulation-induced changes in temperature can profoundly affect tissue function (Elwassif et al. 2006). Moreover, metabolic response occurs in the human head as a result of electrical stimulation. This heat is distributed over body regions by blood circulation and is carried by conduction to the body surface (Fiala, Lomas & Stohrer 1999). Both effects, Joule heat and metabolic response, are causes of temperature increase (Datta, Elwassif & Bikson 2009; Elwassif et al. 2006). How the heat affects the different tissue layers of the head while electroconvulsive therapy is applied has not yet been investigated thoroughly.

There are some analytical and numerical models which explain the basic behaviour of electric field distribution in a volume conductor. It is also possible to find models considering anisotropic electrical conductivity, as seen in the work of Lee et al. (2012). However, limitations are found in the field of ECT, considering the thermal point of view, and considering more abstract phenomena such as the effect of geometric variation, heterogeneous and anisotropic thermal and electrical conductivity of different tissues and temperature effects of biological tissues. Additionally, lack of information is available about the influence of an electric field in the presence of a brain tumor. Due to these limitations, the spatial distribution of temperature, electric field and its gradient has so far not been investigated thoroughly.

Oftentimes it is difficult to analyse in vivo and in vitro measurements due to ethical issues. However, a realistic head model, with its true anatomical features and conductivity behaviour, help us to study these cases and achieve comprehensive results.

Having all these limitations in mind, this study aims to investigate the distribution of temperature and temperature gradient due to high electrical stimulation used in ECT treatments. Beyond that, the models also consider the inhomogeneous and anisotropic thermal and electrical conductivity along the tissues. Magnetic resonance imaging (MRI) and diffusion tensor image (DTI) data are used and, with this, the issues of structural head model details and directional conductivity are addressed respectively. Finite element methods (FEM) possess the ability to consider complex geometries and anisotropic behaviour without discretization errors. Taking this into account, the commercially available FE package COMSOL Multiphysics ® is used to generate and map the thermal and electric field distributions.

With this study, a better understanding of the effects induced by high-stimulation in the thermal point of view is achieved; also, potential damage to any structure of the human head and how this heat influences the neurons and regions of the head is examined. Moreover, it also provides a better understanding of electric field distribution in the human head, in the presence of a brain tumor. The study is implemented using computational simulation and no live or deceased biological samples are used. To validate the results, mathematical models, bio-heat transfer equation (BHTE) linked with Laplace equation applied to electrics and resistive-capacitive network are used.

1.2. Aim and Objectives

The aim of this research is to develop a realistic head model to study how the heat generated due to the electrical input affects the head, how the temperature behaves, the gradient of temperature, any potential damage it might cause, and the effects of electric field and its gradient under ECT. Different techniques are used to include isotropic and anisotropic thermal and electrical conductivities and to have more realistic head models and accurate results. Specifically, the five objectives below are targeted:

1. Realistic human head construction and modelling from thermal and electrical conductive aspects.
2. Investigation of the temperature behaviour in a spherical and realistic human head model under isotropic and anisotropic conductivity conditions.
3. Analysis of the combined effect of temperature and the electrical activities in a human head model.
4. Analysis of the influence of thermophysical parameters and fat layer on the temperature behaviour.
5. The usage of ECT on patients with a brain tumor.

1.3. Research Strategy

This study investigates the influence of thermal and electric fields due to electrical stimulation when electroconvulsive therapy is applied. Spherical and realistic head models will be developed using commercial packages. Different configurations using heterogeneous tissues, isotropic and thermal and electrical anisotropic conductivity and diverse electrode montage, will be considered. At first, a simplified spherical head model is built, as it is easier to construct and understand. From there onwards, a more sophisticated, realistic head model will be developed and constructed using magnetic resonance images. An assumption of linearity between thermal and electrical conductivity was made based on the fact that there is a linearity relationship between their eigenvalues. This assumption will be used to derive the thermal anisotropy on the skull, with thermal and electrical anisotropy conductivity being mathematically applied. Later on, diffusion tensor images will be inserted in the realistic models to consider white matter electrical anisotropy. Also, the presence and influence of a brain tumor will also be considered.

In this study, no human or animal testing has been undertaken, instead, computational simulations are employed to apply the governing bio-heat transfer equation and Maxwell’s equations.

1.4. Thesis Overview

This dissertation consists of eight chapters. The first three chapters provide the research background, a comprehensive literature review about the research and the methodology applied. Chapters 4 to 7 illustrate the diverse cases of the models' design, development, implementation and outcomes in assessing the induced thermal and electric field and their parameters.

Chapter 2 presents an overview of the current transcranial electrical stimulation techniques and their applications. It focuses on electroconvulsive therapy, its usages, properties and parameters, and provides a detailed explanation about bio-thermal models and the sensitivity of the human body to the temperature.

Subsequently, the chapter provides the mathematical background that will be applied in the model developments. Among these formulae are the Maxwell's equation, its simplified quasi-static approximation, the bio-heat transfer equation, the initial and boundary conditions required to define a problem. It also describes the assignment of thermal and electrical conductivity to each of different head tissues.

Chapter 3 describes the techniques and methods to develop the three head models used in this study. It starts with the spherical model and ends with a realistic one. The chapter provides step by step explanations of techniques and methods used in the model development. In addition, the electrode montages are also considered and explained.

Chapter 4 analyses the behaviour of temperature due to ECT electrical stimulation using a simplified four layer spherical model. The bio-heat transfer equation and the Laplace equation are coupled together to solve the problem. Three different electrode montages are considered with two different amplitude inputs. The models are studied using FEM.

Chapter 5 investigates the inclusion and influence of anisotropy thermal conductivity in the skull layer through a five layer spherical head model. The anisotropy is considered and included in two different methods. The models are evaluated and compared with the isotropic ones.

Chapter 6 extends the method used in Chapter 5 considering more layers in a realistic head model. In addition, the influence of including anisotropy electrical conductivity in the skull layer is investigated. Apart from that, the role and effect of biological properties and the influence of fat layer in the thermal behaviour are also explored.

Chapter 7 describes the electric field distribution when ECT stimulation is applied to a patient with a brain tumor. Four diverse tumor grades, varying according to tumor aggressiveness, are conducted; as well as two different tumor locations and three electrode configurations. In addition, white matter anisotropy is assigned from diffusion tensor images and the models with anisotropy are compared with isotropic ones as reference models.

Chapter 8 summarizes the major outcomes and contributions of the study. The chapter also presents current limitations and indicates the future directions in this study area.

2. ELECTROCONVULSIVE THERAPY AND BIO-THERMAL MODELS

2.1. TES and Human Head Model

Transcranial Electrical Stimulation encompasses all forms of research and clinical application of electrical currents to the brain using (at least one) electrodes on the head (Cancelli et al. 2016; Casarotto et al. 2013; Chen et al. 2017; Datta, Elwassif & Bikson 2009; Elwassif et al. 2012; Elwassif et al. 2006; Fertonani & Miniussi 2016; Guleyupoglu et al. 2013; Lee et al. 2012; Peterchev et al. 2012; Wagner, Valero-Cabre & Pascual-Leone 2007). Although not always popular, techniques of transcranial electrical stimulation date back further than one century. At the beginning, it was applied to treat neurological diseases and through time, new methods were invented and the existing ones modified to achieve more accurate results. TES is an alternative to pharmacological treatment in neurological diseases. It can enhance cognitive performance in healthy people and improve clinical conditions in patients (Fertonani & Miniussi 2016).

According to Guleyupoglu et al. (2013), the categories of tES can be divided, historically, into five streams. They were categorized as Electrosleep (ES); Electroanesthesia (EA); Polarizing or direct current stimulation (transcranial Direct Current Stimulation, Transcranial Micropolarization, High Definition transcranial Direct Current Stimulation, Galvanic Vestibular Stimulation); Electroconvulsive Therapy (ECT) and contemporary approaches (transcranial Alternating Current Stimulation (tACS), transcranial Sinusoidal Direct Current Stimulation (tSDCS), and transcranial Random Noise Stimulation (tRNS)).

All these techniques aim to study the behaviour of the brain and provide valuable tools to treat a variety of neurological and psychiatric disorders (Wagner, Valero-Cabre & Pascual-Leone 2007).

One of the inherent problems with these treatments is the need to always consider the correct dosage to be used, as well as the side effects they can cause. Dosage depends on electrode montage and stimulation waveform that is applied trough the electrodes (Guleyupoglu et al. 2013; Peterchev et al. 2010; Peterchev et al. 2012). The electrode parameters include number, position, shape, and composition. Stimulation waveform considers details such as intensity, pulse shape, amplitude, width, polarity, and repetition frequency, duration of and interval between bursts or trains of pulses, and interval between stimulation sessions and total number of sessions (Guleyupoglu et al. 2013).

A human head model is used to simulate different cases of tES problem. These models help investigate and develop those techniques. At first, analytical solutions were developed to calculate spherical homogeneous volume conductors, as seen in Frank (1952). Then, inhomogeneous volume conductors started to be studied like in Salu et al. (1990) and in Rush and Driscoll (1969). The former represented the head as a three-layer spherical model and evaluated the localization of equivalent dipoles in the brain, and the latter proposed a 3-layer spherical volume conductor consisting of scalp, skull and brain, and gave a better understanding of the behaviour of current density distribution inside an inhomogeneous head model. Therefore, De Munck (1988) incorporated a semi-analytical solution to deal with anisotropy in a layered spherical and spheroidal volume conductor; and Zhou and van Oosterom (1992) applied a semi-analytical procedure considering four layer isotropic and anisotropic concentric spherical volume conductor.

Realistic human head models were created from MRI (magnetic resonance) images, enable us to have a better understanding of electromagnetic parameters distribution through different tissue layers. MRI also permits us to verify more appropriate sites to localize electrodes, dosage and duration of the stimulation, among other factors. An example is shown in the work of Bai, Loo and Dokos (2011), in which they modelled a realistic head model to compare the effects of electric field spatial profiles and brain excitation when three different ECT electrode configurations were used.

A detailed high-resolution realistic human and neck head model, including 153 structures, arteries and veins from magnetic resonance angiography (MRA) and diffusion tensor information was developed by Iacono et al. (2015). They applied tACS to illustrate the application. The MIDA model, as it is now called, still provides more details and structural variation than any other model so far developed.

The inclusion of DT-MRI data permitted even more accurate analyses. With more refined geometries of the human head available, it became possible to analyse more factors, such as brain structures and anisotropic conductivity for different tissues. Oostendorp et al. (2008) proposed a method to estimate the potential and current density distribution during tDCS in a five compartment realistic head model. In their study, they included anisotropic electrical conductivity to the skull and white matter.

In the study of Datta et al. (2009), they applied a high spatial resolution MRI derived finite element human head model and resolved cortical gyri/sulci. They compared the spatial focality of conventional rectangular pad (7 x 5 cm^2) and ring (4 x 1) electrode configurations. They suggested that anatomically accurate high resolution MRI based forward models may guide the rational clinical design and optimization for tES techniques. Many other studies can be found which use high resolution human head model (Bai, Loo & Dokos 2011; Datta, Elwassif & Bikson 2009; Lee et al. 2012; Lee et al. 2011; Shahid, Wen & Ahfock 2013).

2.2. Electroconvulsive Therapy

Electroconvulsive Therapy (Figure 2.1) is an intervention used to treat a variety of psychiatric conditions. These disorders include Depression (unipolar and bipolar), Schizophrenia, Bipolar manic (and mixed) states, Catatonia and Schizoaffective disorder (Weiner 2002). This therapeutic intervention applies an electric voltage or current to the scalp through electrodes (Lee et al. 2012). The induced electric field is typically widespread and reaches deep brain regions (Rosa & Lisanby 2012). The patient should receive a muscle relaxant and general anesthesia before the procedure. The stimulation is generated in cycles that vary from 0.5 to 8 seconds of duration, the frequency varies between 20 Hz and 120 Hz, and the pulse currents vary from 500 mA to 900 mA (Weiner 2002). The entire procedure can be completed in approximately 10 minutes.

Figure 2.1. Illustration showing electroconvulsive therapy treatment (NIMH 2016).

Stimulus waveform, electrode placement, and stimulus dosage are factors and parameters that should be considered for the practice of ECT. The waveforms used are the sine wave, partial sine wave, brief pulses and ultra-brief pulses. Each waveform differs in their efficiency to deliver seizures. The leading edge of each phase of the waveform is responsible for neuronal depolarization and seizure induction (Weiner 2002). Seizure threshold may be estimated by determining the minimal electrical dose necessary to elicit a generalized seizure of a specified minimum duration (Sackeim et al. 1994). Electrode placement and stimulus dosage parameters are also important to maximize efficacy and tolerability (Lee et al. 2012; Weiner 2002). These factors can affect the clinical outcome (Weiner 2002).

The physical properties of ECT stimulus affect efficacy and cognitive side effects (Sackeim et al. 1994). Some of the side effects include problems of general anaesthesia, memory loss, possibility of aggravating problems inside the head, possibility of getting uncontrollable fits or status epilepticus (Weiner 2002). Although improvements have been made in ECT throughout time, many questions still need to be answered (Lee et al. 2012). For example, what is the best electrode configuration for the practice of ECT? How do we reduce and avoid side effects? Which are the best stimulus current parameters for maximal efficacy and tolerability? What is the influence of heat transfer in this procedure? etc.

Normally, three types of electrode configurations are used. They are right unilateral (RUL); bilateral frontotemporal (BL); and bifrontal (BF) ECT. Each has its own advantages and disadvantages but there is a lack of information and it is impossible to say which is the most effective or which has fewer side effects (Lee et al. 2012; Rosa & Lisanby 2012; Weiner 2002). Cognitive side effects and efficacy are influenced by electrode placement and stimulus intensity. BL produces more short and long-term side effects than RUL. An example is the development of a transient delirium and amnesia. If the stimulus by RUL is applied just above seizure threshold, its efficacy is reduced, being therapeutically weak; and when applied as suprathreshold stimulation, its efficacy is equivalent to BL ECT, however it is associated with more severe short-term cognitive deficits. Some factors have some predictive value with respect to seizure threshold, such as electrode placement, gender, age, anaesthetic dosage, and concomitant medications (Weiner 2002). Alternative approaches to further improve the focality of ECT, and thereby reduce its cognitive side effects, include novel electrode configurations, like in focal electrically administered seizure therapy (FEAST). In this configuration a large electrode is placed over the parietal region and a small one on the forehead and unidirectional stimulus is delivered (Lee et al. 2012; Rosa & Lisanby 2012).

Ultrabrief pulse has been recently used to further improve the risk–benefit ratio of ECT (Loo et al. 2012). This approach substantially reduces the cognitive side effects without loss of efficacy, although a response may take longer and mid-course dose adjustments may be necessary to ensure efficacy (Rosa & Lisanby 2012).

A study conducted by Swartz (1989) dealing with heat liberation at the electrode-skin interface during ECT stimulus, reported that the skin was the only possible site for an electrical burn with ECT devices from his time. The explanation he gave was that the substantial deep tissue heating (as in the brain) does not occur, because the typical maximum output of an ECT device (100 J at 220 Ω impedance) elevates deep tissue temperature by less than 0.092 ºC. He concluded that if there was a poor electrode-skin contact, then skin burn could occur.

ECT produces strong stimulation in the brain. The E-field distribution varies according to the electrode configuration used, configurations of the model and assigned conductivities (Lee et al. 2016). The inclusion of white matter anisotropy conductivity is another factor that influences the E-field. This influence was investigated by Lee et al. (2008) on the EEG forward solution, by Lee et al. (2011) and Lee et al. (2012) on the electric field strength induced by ECT and by several other authors in diverse areas (Kim et al. 2014; Lee et al. 2016; Seo, Kim & Jun 2015; Shahid, Wen & Ahfock 2013; Shahid et al. 2015). Lee et al. (2011) created an anatomically-realistic finite element human head model incorporating tissue heterogeneity and white matter conductivity anisotropy using structural MRI and DT-MRI data. The white matter conductivity tensors were estimated according to Basser, Mattiello and LeBihan (1994) where the conductivity tensors share eigenvectors with the measured diffusion tensors. They computed the electric field spatial distributions using four electrode configurations (BL, BF, RUL, FEAST). Also, they performed a quantitative comparison of the electric field strength in specific brain regions of interest which was thought to be associated with side effects of ECT (e.g., hippocampus and insula). They found that white matter conductivity anisotropy should be taken into account in ECT electric field models, because neglecting it yields a difference of up to 19 %, 25 % and 34 % in electric field strength in the whole brain, hippocampus, and insula, respectively.

Lee et al. (2012) investigated the electric field (E-field) strength generated by various ECT electrode configurations in specific brain regions of interest (ROIs) that have putative roles in the therapeutic action and/or adverse side effects of ECT. They also characterized the impact of the white matter conductivity anisotropy on the E-field distribution. A finite element head model incorporating tissue heterogeneity and WM anisotropic electrical conductivity based on structural MRI and DT-MRI data was constructed. The spatial E-field distributions were computed with the ECT electrode placements BL, BF, RUL and FEAST. The results show that the median E-field strength over the whole brain is 3.9, 1.5, 2.3, and 2.6 V/cm for the BL, BF, RUL, and FEAST electrode configurations respectively. They also found that neglecting the WM electrical conductivity anisotropy produces E-field strength error up to 18% overall and up to 39% in specific ROIs, motivating the inclusion of the white matter electrical conductivity anisotropy in accurate head models.

When comparing ECT with TMS (transcranial magnetic stimulation) in depression treatment, it has been found that ECT is the most efficacious, but it is difficult for patients to tolerate. The review done by Chen et al. (2017), the efficiency of ECT is 65 %, and, according to the TMS setup used, the efficiency varies from 2 to 25 %. On the other hand, ECT tolerability is only 14 %, while TMS is 16 % to 52 %. However, ECT generates from 3 to 29 times more stimulation in areas related to antidepressant effect, such as thalamus, hypothalamus and hippocampus (Lee et al. 2016).

2.3. Bio-thermal Model

The human body is sensitive to temperature changes, especially the brain (Datta, Elwassif & Bikson 2009; Elwassif et al. 2006). Brain temperature is believed to be dependent primarily on cerebral perfusion and cerebral metabolic rates. Current medical imaging technology permits the measurement of localized perfusion rates during MRI or computed tomography (CT) scans, but it is not currently possible to monitor perfusion continuously over time (Lillicrap et al. 2012). A temperature increase of approximately 1 ºC can lead to profound effects on a single neuron and neuronal network function (Datta, Elwassif & Bikson 2009; Elwassif et al. 2006). Temperatures above 40 ºC in the human body can result in cell damage and tissue ablation (Elwassif et al. 2006). Metabolic processes in the organism try to compensate for this excessive heating in an attempt to preserve the temperature at an acceptable level (Zaridze et al. 2005).

Two areas in which brain and body temperature may have a crucial impact are neurodegenerative and mood disorders. Many failures in temperature control have been observed in psychiatric conditions. Salerian, Saleri and Salerian (2008) have proposed a temperature-dependent biochemical system in humans governed by the Arrhenius rate law. They postulated that due to the exponential relationship between temperature and biochemical reactions, a relatively minor alteration in core body or brain temperature may be of significant therapeutic benefit in combating neurodegenerative disorders and prolonging lifetime. They speculated that this small alteration may be as little as a drop of 1 ºC in core body temperature.

Investigations on the effect of electroconvulsive shock (ECS) on body temperature have been contradictory. A single ECS has been demonstrated to reduce colonic temperature in mice. However, repeated ECS attenuates the hypothermia produced by single ECS. Application of single ECT is hypothermic and it improves mania. Chronic ECT is thermogenic and it improves depression (Salerian, Saleri & Salerian 2008).

The majority of bio-heat models make use of Penne's bio-heat equation (Pennes 1948), which is based on the classic Fourier law and accounts for blood flow through a heat source term that depends on temperature (Bourantas et al. 2014). In different areas it is possible to find the application of bio-heat equation, such as in the human brain (Lillicrap et al. 2012), human and animal eye (Barton & Trembly 2013; Berjano, Saiz & Ferrero 2002; Karampatzakis & Samaras 2010; Scott 1988), human breast (Bezerra, L. et al. 2013; Bezerra, L. A. et al. 2013), neural probe (Christian, Firebaugh & Smith 2012), specific absorption ratio (SAR) (Bernardi et al. 2003; McIntosh, Anderson & McKenzie 2005; Nadobny et al. 2007), human head stimulation (Datta, Elwassif & Bikson 2009; Elwassif et al. 2012; Elwassif et al. 2006).

A healthy human brain was modelled thermally as a 3-concentric spherical model using finite element method by Lillicrap et al. (2012) to investigate the effectiveness of tissue cooling as a result of spatial variations in cerebral blood flow and cerebral metabolic rate. These factors were found to affect the absolute level of tissue cooling achievable, but not the rate of cooling.

A Eulerian approach for the numerical solution of the transient bio-heat transfer equation with temperature-dependent properties was developed by Bourantas et al. (2014). They extended the bio-heat equation in order to incorporate water evaporation and tissue damage during ablation, accounting for temperature-dependent thermal properties of the tissue. This approach treated 3D heat conduction problems within pathological tissues of locally varying conductivity and locally varying blood perfusion rate, viewing them as continuous domains, and solving the corresponding bio-heat differential equation with variable coefficients. In addition, they showed that arbitrary and random conductivity maps can be treated in a straightforward manner with this method in contrast to the flux continuity technique that is not applicable in the case of vaguely defined boundaries.

In the study conducted by Elwassif et al. (2006), they provided information on the thermal effects of DBS using finite element models to investigate the magnitude and spatial distribution of DBS-induced temperature changes. For that, the coupled Laplace equation of an electric field and the Pennes bio-heat transfer equation were solved. The parameters investigated were stimulation waveform, lead selection (two types of Medtronic leads, models 3387 and 3389 DBS lead), brain tissue electrical and thermal conductivities, blood perfusion, metabolic heat generation during the stimulation and lead thermal conductivity/heat dissipation through the electrode. This study did not consider CSF convection and inhomogeneous conditions of tissues. The results showed that temperature increases with electrical conductivity and decreases as thermal conductivity increases. Furthermore, clinical DBS protocols increase the temperature of surrounding tissue by up to 0.8 ºC depending on stimulation/tissue parameters.

Datta, Elwassif and Bikson (2009) provided information on the thermal effects of tDCS using a MRI-derived finite element human head model. A bio-heat model (coupled Laplace equation of an electric field and the Pennes bio-heat transfer equation) were solved to compare the tissue temperature increases of tDCS using conventional rectangular-pad (7 x 5 cm^2) and HD-tDCS using the ring (4 x 1) electrode configurations. The results indicated that clinical tDCS do not increase tissue temperature and 4 x 1 ring configurations leads to a negligible increase in scalp temperature. However, the study did not consider micro architecture of the skin, nor variation in the electrical and thermal properties. A clinical tDCS study (Ezquerro et al. 2016) evaluated the skin redness over a crossover trial. They found mild to moderate erythema after tDCS-induced stimulation.

Another study of the thermal effects of DBS was conducted by Elwassif et al. (2012). They developed a heat transfer finite element method simulating DBS incorporating the realistic architecture of Medtronic 3389 leads. The temperature changes were analysed considering different electrode configurations, stimulation protocols and tissue properties. The results were then validated using micro-thermocouple measurements during DBS lead stimulation in a saline bath. FEM results indicated that lead design (materials and geometry) may have a central role in controlling temperature rise by conducting heat. Apart from that, a temperature increase was found to depend on root mean squared voltages rather than waveform details, and the electrode voltage attenuation was assumed to be inherently reversible capacitive (or reversal faradaic) and thus with no power dissipation (this reversibility is indeed expected for a chronically implanted device). They showed how modifying lead design could effectively control temperature increases. Also in the DBS field, Iacono et al. (2013) modelled a millimetric resolution and multiscale head model to analyse the accuracy of numerical modelling of a radio-frequency field when a patient has a DBS electrode implanted. However, they computed only an electric field and local SAR, and a thermal evaluation was not considered.

It is also found in the literature review that the time-domain finite-difference method was applied to the thermal area such as Bernardi et al. (2003) and Nadobny et al. (2007). The former computed the electromagnetic field (frequency ranges between

10 and 900 MHz) inside a detailed anatomical heterogeneous human body model using the finite-difference time-domain method. The corresponding temperature increase was evaluated through an explicit finite-difference formulation of the bio-heat equation. The thermal model was composed by a controlling and controlled system, which took into account the thermoregulatory system of the human body, and was validated through a comparison with experimental data. This study aimed to investigate the relation between limits settled in the safety standards and the thresholds for the induction of adverse thermal effects. While Nadobny et al. (2007), performed an investigation of magnetic resonance (MR)-induced hot spots in a high-resolution human model. The study analysed the temporal SAR mode (steady imaging and intermittent imaging); the simulation procedure (related to given power levels or to limiting temperatures); and different thermal tissue properties including temperature-independent and temperature-dependent perfusion models. The electromagnetic and thermodynamic studies were carried out in simulations.

Studies considering anisotropic thermal conductivity are found in the study of both human and animal eyes. Berjano, Saiz and Ferrero (2002) presented a theoretical model for the study of cornea heating with radio-frequency currents. Their numerical model allowed the study of the temperature distributions in the cornea, by solving a coupled electric-thermal problem, and to estimate the dimensions of the lesion in the cornea. They analysed the effect of temperature influence on the tissue electrical conductivity; the dispersion of the biological characteristics; the anisotropy of the cornea thermal conductivity; the presence of the tear film; and the insertion depth of the active electrode in the cornea. Their results suggested that these effects have a significant influence on the temperature distributions and thereby on the lesion dimensions. Both their study and the work of Trembly and Keates (1991) suggested that conductivity is larger in the longitudinal direction (parallel to the corneal surface) than transverse direction. The study done by Berjano, Saiz and Ferrero (2002) involved temperature profile geometry with a more ellipsoidal shape (width/depth ratio of 1.3) and they concluded that there is a direct relation between maximum temperature (T_{max}) and the temperature profile dimensions. In the study of Karampatzakis and Samaras (2010) they concluded that the introduction of a tangential component of thermal conductivity larger than the transverse one led to a smoother temperature variation along the vertical axis of the corneal surface. Also in the study of Barton and Trembly (2013) they stated that the anisotropy of the thermal conductivity of the cornea might be known, in order to quantify the balance of heat transfer toward the epithelial and endothelial layers and parallel to them.

2.4. Quasi-static Approximation and Bio-heat Transfer Equation

When the frequency is low, from direct current (DC) to 10 kHz, biological material exhibits strong resistivity behaviour. Therefore, Maxwell’s equation can be simplified to the quasi-static approximation (Bai, Loo & Dokos 2013; Ferdjallah, Bostick & Barr 1996; Malmivuo & Plonsey 1995; Shahid 2013). According to Ohm’s law and supposing electric field strength, E, throughout a passive volume conductor model, has the Laplace partial differential equation:

$$\boldsymbol{\nabla} \cdot (-\boldsymbol{\sigma}\boldsymbol{\nabla} \boldsymbol{V}) = \mathbf{0} \quad \textbf{or} \quad \boldsymbol{\nabla} \cdot \begin{bmatrix} \boldsymbol{\sigma_{xx}} & \boldsymbol{\sigma_{xy}} & \boldsymbol{\sigma_{xz}} \\ \boldsymbol{\sigma_{yx}} & \boldsymbol{\sigma_{yy}} & \boldsymbol{\sigma_{yz}} \\ \boldsymbol{\sigma_{zx}} & \boldsymbol{\sigma_{zy}} & \boldsymbol{\sigma_{zz}} \end{bmatrix} \begin{bmatrix} \boldsymbol{\partial V/\partial x} \\ \boldsymbol{\partial V/\partial y} \\ \boldsymbol{\partial V/\partial z} \end{bmatrix} = \mathbf{0} \textbf{ in } \boldsymbol{\Omega} \qquad (1)$$

where σ and V are the electrical conductivity and the scalar electric potential in a volume Ω.

The electrical conductivity is a scalar number in the case of isotropic volume conductors. For anisotropic conductors, σ is a tensor, where it is possible to consider its preferential directions of current flow (Bai, Loo & Dokos 2013; Shahid 2013).

Pennes (1948) formulated a simplified bio-heat transfer equation (BHTE), with the assumption that heat transfer in tissues occurs in the capillaries and they are in good thermal balance with the surrounding tissues. BHTE is heat conduction, with specific terms for the generation of heat, due to blood perfusion and to metabolic heat. The equation is shown below:

$$\boldsymbol{\rho c \frac{\partial T}{\partial t} = \nabla(k\nabla T) + \omega\rho_b c_b(T_a - T) + Q_m} \tag{2}$$

where ρ: density (kg/m^3), c: heat capacity ($J/(kg.^oC)$), k: thermal conductivity ($W/(m.^oC)$), T: temperature (^oC), T_a: arterial blood temperature (^oC), ω_b: blood perfusion rate ($1/s$), Q_{met}: metabolic heat source (W/m^3), and the subscript *b* denotes blood (Bezerra, L. et al. 2013; Datta, Elwassif & Bikson 2009; Silay, Dehollain & Declercq 2008). The term from the left hand side is related to the rate of stored energy in the tissue mass that balances the equation. The first term from the right hand side is related to the rate of input and output energy; the second term is an additional amount related to heat transfer from blood flow, that is, the energy added or removed due to the convective blood flow into and out of the tissue; and the last term is the generation of metabolic heat (Berger, Goldsmith & Lewis 1996; Christian, Firebaugh & Smith 2012).

The thermal conductivity is also a scalar number in the case of isotropic volume conductors. For anisotropic conductors, k is a tensor (Equation 3), where it is possible to consider its preferential directions of current flow (Lewis et al. 1996).

$$\boldsymbol{k = \begin{bmatrix} k_{xx} & k_{xy} & k_{xz} \\ k_{yx} & k_{yy} & k_{yz} \\ k_{zx} & k_{zy} & k_{zz} \end{bmatrix}} \tag{3}$$

In transcranial electrical stimulation, current is applied through the electrodes. The electrical stimulation generates heat which increases the temperature and the temperature variation can also occur along the tissue of the head. Taking this into consideration, the physics applied involves heat transfer and electrical potential simultaneously (Datta, Elwassif & Bikson 2009; Elwassif et al. 2012; Elwassif et al. 2006):

$$\boldsymbol{\rho c \frac{\partial T}{\partial t} = \nabla(k\nabla T) + \omega\rho_b c_b(T_a - T) + Q_m + \nabla|\sigma\nabla V|\ .} \tag{4}$$

2.4.1. Initial and Boundary Conditions

Both Maxwell's and bio-heat transfer equations need specifications of the required initial (IC) and boundary conditions (BC) (Figure 2.2) to completely formulate the problem. For the electrical physics, the exposed boundaries (Γ_e) are considered electrically insulated and are represented by Neumann boundary conditions:

$$\boldsymbol{n}\cdot\boldsymbol{J}|_{\boldsymbol{\Gamma_e}} = \mathbf{0} \qquad \textbf{or} \qquad \boldsymbol{n}\cdot(\boldsymbol{\sigma\nabla V})|_{\boldsymbol{\Gamma_e}}=\boldsymbol{0}. \tag{5}$$

The inner boundaries (Γ_i) are expressed by the continuity of the normal component of the current density between regions of different conductivity:

$$(\boldsymbol{n}\cdot\boldsymbol{J_1})|_{\boldsymbol{\Gamma_i}} = (\boldsymbol{n}\cdot\boldsymbol{J_2})|_{\boldsymbol{\Gamma_i}} \qquad \textbf{or} \qquad [\boldsymbol{n}\cdot(\boldsymbol{\sigma\nabla V_1})]|_{\boldsymbol{\Gamma_i}} = [\boldsymbol{n}\cdot(\boldsymbol{\sigma\nabla V_2})]|_{\boldsymbol{\Gamma_i}} \tag{6}$$

The exposed surface of the cathode (Γ_S) is assigned the Dirichlet boundary ($V=0$ *volts*) condition, whereas, the exposed surface of the anode (Γ_S) can be assigned with either the Dirichlet ($V=V_0$ *volts*) or the Neumann ($n\cdot J = J_n$ A/m^2) BC, where V_0 is the fixed electrode voltage and J_n is the surface current density normal to the electrode surface.

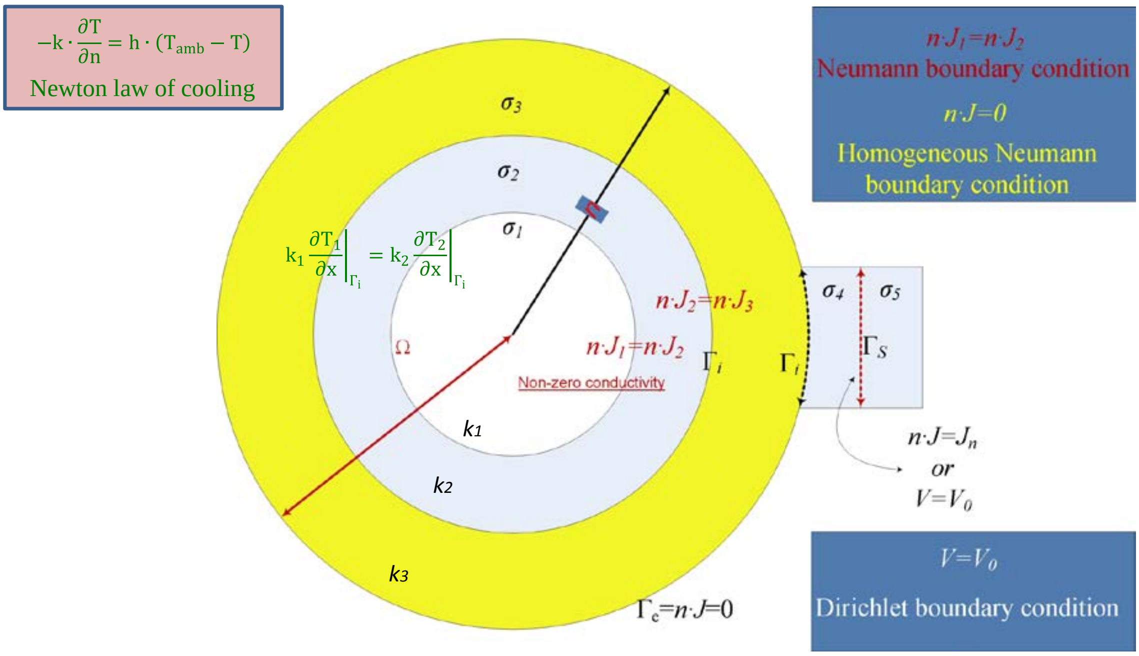

Figure 2.2. Model showing thermal and electrical BC.

For the thermal physics, convection occurs in the external surface of the head model (Γ_e), and thus, heat flux is assigned to the external BC:

$$-\boldsymbol{k} \cdot \frac{\partial \boldsymbol{T}}{\partial \boldsymbol{n}} = \boldsymbol{h} \cdot (\boldsymbol{T}_{\boldsymbol{amb}} - \boldsymbol{T}). \tag{7}$$

where h is the heat transfer coefficient and T_{amb} is the external temperature.

This equation is also known as Newton law of cooling. In the interfaces of the head conduction occurs between two layers and equation 8 can be assigned:

$$\boldsymbol{k}_1 \frac{\partial \boldsymbol{T}_1}{\partial \boldsymbol{x}}\bigg|_{\Gamma_i} = \boldsymbol{k}_2 \frac{\partial \boldsymbol{T}_2}{\partial \boldsymbol{x}}\bigg|_{\Gamma_i} \tag{8}$$

2.5. Electrical and Thermal Conductivity Representations

2.5.1. Anisotropic Electrical Conductivity

Some regions of the head present anisotropic electrical conductivity (De Munck 1988; Marin et al. 1998; van den Broek et al. 1998; Wolters et al. 2006). The expression that gives the anisotropic electrical conductivity is found in the literature and is usually given in local coordinates as:

$$\boldsymbol{\sigma}_{\boldsymbol{skull}} = \begin{bmatrix} \boldsymbol{\sigma}_{\boldsymbol{T}} & \mathbf{0} & \mathbf{0} \\ \mathbf{0} & \boldsymbol{\sigma}_{\boldsymbol{T}} & \mathbf{0} \\ \mathbf{0} & \mathbf{0} & \boldsymbol{\sigma}_{\boldsymbol{R}} \end{bmatrix} \tag{9}$$

where σ_{SKULL} is a second rank symmetric tensor $(\sigma_{SKULL}^{T} = \sigma_{SKULL})$ and positive definite, and σ_T and σ_R represent the conductivity in tangential and radial direction, respectively.

There are certain methods and approaches to calculate the electrical conductivity from the diffusion weighted MRI. One is a linear relationship that relates the eigenvalues and the tensor (Haueisen et al. 2002):

$$\boldsymbol{\sigma = \frac{\sigma_e}{d_e} D} \tag{10}$$

where σ_e and d_e are the effective extracellular conductivity and diffusivity, respectively; D is the diffusion tensor; and the intracellular conductivity is assumed to be negligible. Another approach is the volume constraint (VC) (Wolters et al. 2006) which considers that eigenvalues must retain their geometric mean, and thus, the volume of the conductivity tensor:

$$\boldsymbol{\frac{4}{3}\pi\sigma_R(\sigma_T)^2 = \frac{4}{3}\pi\sigma_{iso}^3.} \tag{11}$$

A third approach is obtained combining equations (10) and (11) and using a matrix to represent the diffusion tensor in a voxel belonging to the WM (Hallez et al. 2008):

$$\boldsymbol{\frac{d_1}{\sigma_1} = \frac{d_2}{\sigma_2} = \frac{d_3}{\sigma_3}} \tag{12}$$

Another method is the Wang constraint (Wang) (Wang, Haynor & Kim 2001), where the product of radial and tangential conductivity should remain constant and be equal to the square of the isotropic conductivity:

$$\boldsymbol{\sigma_R\sigma_T = \sigma_{skull}^2.} \tag{13}$$

2.5.2. Anisotropic Thermal Conductivity

Nadobny et al. (2007) presented a time-dependent finite-difference (FD) scheme that uses an explicit treatment of temperatures and temperature gradients to solve the BHTE (Equation 2).

In this approach, the BHTE is discretized by applying a forward-intime, central-in-space (FTCS) explicit FD scheme, as follows:

$$\boldsymbol{T^{\tau+1}} \cong \frac{\boldsymbol{T^{\tau} \cdot C + D^{\tau} + B^{\tau}}}{\boldsymbol{A^{\tau}}} \tag{14}$$

where $A^{\tau} = \omega^{\tau} \rho_b c_b + \rho c/\Delta t$, $B^{\tau} = \omega^{\tau} \rho_b c_b T_b$ and $C = \rho c/\Delta t$. τ is the consecutive number of the time step with the length Δt. D^{τ} is the discretized conductive term for $div(\kappa grad T)$ which is dependent on the temperature gradients *Gx*, *Gy* and *Gz*. The conductivities $\kappa_{x/y/z}$ are calculated via series connections of the original (nonaveraged) conductivity values κ in neighbouring cubes. Therefore, they are direction dependent being numerically induced anisotropy near the thermal interfaces.

To avoid staircase errors, the exterior boundaries need to be written in vector formulation (Nadobny et al. 2007):

$$\vec{\boldsymbol{q}} \cong -\boldsymbol{\kappa} \frac{\partial \boldsymbol{T}}{\partial \boldsymbol{n}} \vec{\boldsymbol{n}}^{\boldsymbol{O}} = -\boldsymbol{\kappa} \cdot \vec{\boldsymbol{G}}_{\boldsymbol{n}} \cong \boldsymbol{h} \cdot (\boldsymbol{T} - \boldsymbol{T}_{\boldsymbol{ext}}) \cdot \vec{\boldsymbol{n}}^{\boldsymbol{O}} \tag{15}$$

where $\vec{q}$ is the conduction heat flux vector, $\vec{n}^{O}$ is the unit surface normal vector, and $\vec{G}_n$ is the normal temperature gradient vector.

2.5.3. The Relation between Thermal and Electrical Conductivity

A linearity between thermal conductivity tensor and electrical conductivity tensor is found in the literature (Khundrakpam, Shukla & Roy 2010). The model for the relationship between electrical and thermal conductivity (Figure 2.3) is based on the effective medium approach for two-phase anisotropic media. The relationship of the effective transport tensor to the microstructure is written as:

$$\frac{[\boldsymbol{\alpha_{eff}}]}{\boldsymbol{\alpha_e}} = [\boldsymbol{R}^{(i)}][\boldsymbol{P_\alpha}] \tag{16}$$

where α denotes either thermal or electrical conductivity; the subscripts eff and e denote tensors to the microstructure and transport coefficients in the host phase (basic interstitial matrix), respectively; $[R^{(i)}]$ is a concatenated series containing microstructure information; and, $[P_\alpha]$ is a concatenated series of α. Therefore, it is possible to obtain a cross-property relationship between the two transport tensors:

$$\boldsymbol{\kappa_v} = \boldsymbol{a_1}(\boldsymbol{\sigma_v} \pm \boldsymbol{c_1}) \tag{17}$$

where κ_v and σ_v are the eigenvalues of the thermal conductivity tensor and electrical conductivity tensor, respectively, while a_1 and c_1 are numerical constants.

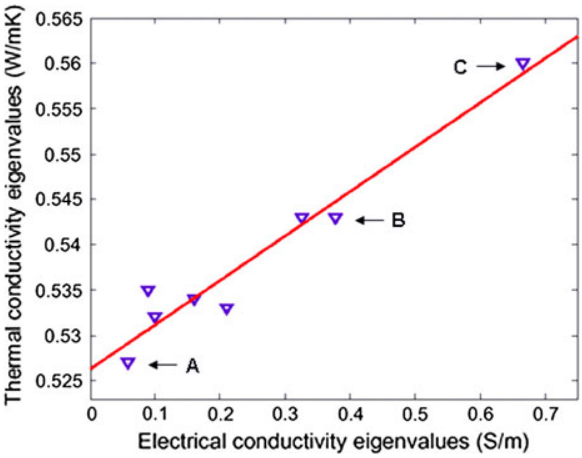

Figure 2.3. Experimental validation of cross-property relationship between thermal conductivity and electrical conductivity values of various tissues. Electrical and thermal conductivity eigenvalues (data points from left to right: white matter, grey matter, cerebral cortex, cerebellum, spleen, liver, kidney and heart) (Khundrakpam, Shukla & Roy 2010).

These electrical approaches are used to assess the effects of directional electrical conductivity on E-filed distribution under ECT; and the thermal approach is going to be used to calculate the effects of anisotropic thermal conductivity on temperature variation under ECT. Moreover, the influence of the temperature effect of biological tissue on the electrical conductivity will be verified. This procedure and verification has never been used previously in ECT analysis.

2.6. Discussions of Reviewed Works

ECT has been detailed studied under the electrical perspective, as can be found in the literature (Bai 2012; Bai et al. 2012; Bai, Loo & Dokos 2011; Casarotto et al. 2013; Lee et al. 2016; Lee et al. 2012; Lee et al. 2011; Loo et al. 2012; Peterchev et al. 2010; Rosa & Lisanby 2012; Sackeim et al. 1994; Swartz 1989; Weiner 2002). From the simplistic models to more realistic geometries, the consideration of isotropic tissues and electrical anisotropy tissues, diverse electrode placement and configuration of the electrical input, the electrical stimulation and its effects has been researched in the ECT practice. However, there is a gap when concerning to the thermal point of view. There is no information related to the behaviour of temperature generated due to that electrical stimulation. Therefore, in this research, both the thermal and electric field resulted from ECT electrical stimulation are investigated.

The electric field studies (De Munck 1988; Rush & Driscoll 1969; Salu et al. 1990; Zhou & van Oosterom 1992) started with simple spherical geometries. Afterwards, more complex realistic geometries and parameters are included (Bai, Loo & Dokos 2011; Datta et al. 2009; Iacono et al. 2015; Lee et al. 2016; Lee et al. 2012; Oostendorp et al. 2008; Shahid, Wen & Ahfock 2013). Following that way, at first, a simplified spherical model is considered and the behaviour of temperature is studied. Afterwards, thermal and electrical anisotropy conductivity is implemented. Electrical anisotropy conductivity is applied in several tES techniques, under different implementations (De Munck 1988; Hallez et al. 2008; Lee et al. 2011; Marin et al. 1998; Seo, Kim & Jun 2015; Shahid, Wen & Ahfock 2013; Suh, Lee & Kim 2012; van den Broek et al. 1998; Wang, Haynor & Kim 2001; Wolters et al. 2006). On the other side, thermal anisotropy conductivity is implemented in other areas of application as well, such as human and animal eyes. Moreover, the implementation of thermal anisotropy to study tES practices, including ECT stimulation, is not found in the literature. Also, the implementation of thermal anisotropy conductivity coupled with electrical anisotropy conductivity applied to tES techniques is not found in the literature. However, Khundrakpam, Shukla and Roy (2010) have correlated thermal and electrical diffusion tensors. Later on, realistic geometries are considered in the analysis of thermal and electric field due to ECT electrical stimulation.

The behaviour of the electric field when in the presence of a brain tumor, during the ECT stimulation, has also been investigated in the present work.

2.7. Chapter Summary

A literature review of transcranial electrical stimulation, electroconvulsive therapy and bio-thermal models has been covered in this chapter. It has also provided a background to the electrical and thermal physics that will be applied in the models in this study, including an explanation of different methods of anisotropy. Lastly, it introduces an alternative method for head modelling, the resistive-capacitive network.

3. DEVELOPMENT OF HUMAN HEAD MODEL

This chapter introduces the processes and models that are developed and used in this study. Three types of human head model are considered: spherical; realistic; and resistive network models. These models are developed for different purposes. Some are simplified to investigate specific questions as a simpler model makes the results more focused and easier to interpret. On the other hand, a realistic model provides a more convincing answer. The accuracy, analysis and comparison of the performance of the different models introduced in this chapter will be conducted in subsequent chapters.

3.1. Spherical Head Model Development

Three different spherical head models (SHM) are developed. Figure 3.1 shows a flowchart with steps for the development of these models. The first is the four layers spherical head model (SHM_4) built using the package COMSOL *Multiphysics*® 4.1 (COMSOL Inc.). The diameter of the external layer is selected as an average size of an adult human head of 21 cm. The layers' radial thicknesses are 1 cm each and the inner layer radius is 9 cm. Each layer is considered to represent one type of tissue in the human head such as scalp, skull, cerebro-spinal fluid (CSF) and brain, in outer to inner order, respectively.

The second spherical head model consists of five different layers (SHM_5), with the brain being separated into grey matter (GM) and white matter (WM). From external to internal, the layers are: scalp; skull; CSF; GM and WM, respectively. Once again, the outer layer was considered as 21 cm. Each layer's radial thickness is 1 cm and the inner layer diameter is 17 cm. This model is also built with the assistance of the software COMSOL *Multiphysics* ® 4.4 (COMSOL Inc.).

The third spherical head model (SHM_6) has six layers. In this model, a layer of fat is added. Once more, each layer represents one different type of tissue, and they are, in outer to inner order: scalp; fat; skull; CSF; GM and WM. For this model, the external layer was assigned an 18.4 cm diameter, which correlates to the size of the six layers realistic adult human head model developed and described in Section 3.2. The thicknesses of each layer are also changed to: 5.6 mm; 3.75 mm; 7.08 mm; 3 mm; 3 mm and 69.57 mm respectively based on the reference (Deng, Lisanby & Peterchev 2011).

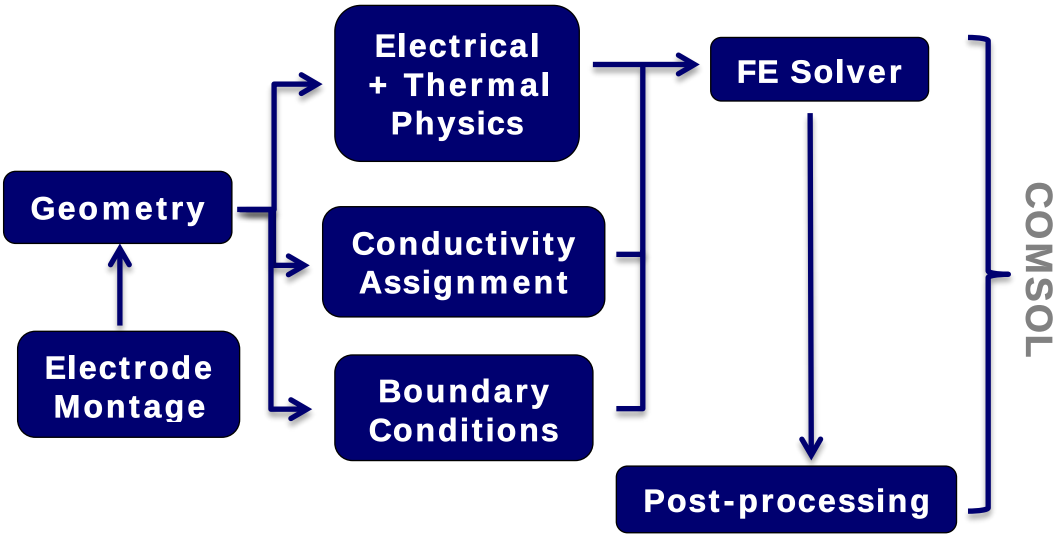

Figure 3.1. Flowchart to develop spherical head models.

3.2. Realistic Human Head Models

The realistic human head models (RHM) are developed based on magnetic resonance images (MRI) and diffusion tensor imaging (DTI) (if anisotropy is considered). Here, a detailed description is provided because of the complexity of the process and the model.

3.2.1. Magnetic Resonance Images

Computerized tomography (CT) was the only technique available to clinicians to study the human brain before the 1980s. It used radiation doses and was insensitive to many types of lesions. After the 1980s, MRI was introduced in preference to CT scans.

MRI is a widely accepted imaging technique used to study and analyze the brain. This technique applies a strong magnetic field through an object. The idea is to align the protons of water and thus be able to map different tissues. In short, in order to generate an MRI, magnetic field gradients are applied and a coordinate system is encoded onto the object, causing the generation of a MR image (Boulby; & Rugg 2003). It is known that each tissue contains a different quantity of water, and that is what provides the contrast in the images. For example, the brain contains more water in its constitution compared to the skull, a bone structure. The research, up to now recognizes MR techniques as being safe to the human body.

Different types of images constitute the MRI; proton density (PD); T1-weighted (T1w) and T2-weighted (T2w). PD, also known as spin density, relates to the concentration of MRI-visible protons in tissue. Most of them are localized in water and, practically, they can be seen when the acquisition has a short TE (echo time) and long TR (repetition time). If the tissue has edema, normally it will have an increase in PD, and after the treatment, a reduction in PD occurs (Tofts 2003). Changes in PD are often correlated to T1w changes. The signals of T1w are usually inversely associated to the longitudinal relaxation time T1 in a nonlinear way. Biophysical properties of tissues are intrinsic to T1w. The importance of T1w is for tissue characterization, contrast agent uptake studies and to measure blood volume and perfusion. In normal tissues, T1w values are associated to macromolecule concentration, water binding and water content. Therefore the contrast in the brain is caused by myelin making WM have a shorter T1w than GM (Gowland; & Stevenson 2003). On the other hand, T2w describes the process decay of the nuclear signal, determining how long it is possible to measure the nuclear signal for. It is used mainly for qualitative diagnostic purposes (Boulby; & Rugg 2003).

3.2.2. Diffusion Tensor Imaging

A variant from MRI is the Diffusion-Weighted Imaging (DWI) that is based on tissue water diffusion rate (Kingsley 2006a; Soares et al. 2013). Diffusion relates to the Brownian motion of a fluid. When the diffusion has no preferential direction to move and is the same everywhere, it is called isotropic. However, in some structures the diffusion is preferential in certain paths, which is known as anisotropy. In order to measure the anisotropy, that is the relative diffusion coefficient of water molecules in different directions, diffusion tensor imaging is used (Kingsley 2006a). DTI contains axonal organization of the brain and directional information of fibrous structure, such as white matter and muscles (Mori & Zhang 2006; Vilanova et al. 2006). It started to be used in the mid 1990s with Basser, Mattiello and LeBihan (1994).

With DTI, it is possible to calculate the direction and amount of water diffusion, known as 'tensor'. In this way, by using DTI, it is possible to deduce properties of the diffusion in each voxel, such as molecular diffusion rate (mean diffusivity (MD) and apparent diffusion coefficient (ADC)), preference direction of diffusion (fractional anisotropy (FA)) and axial and radial diffusivity (Kingsley 2006c; Soares et al. 2013). Therefore, with DTI, the possibility of investigating structural and anatomical features of internal tissues, such as WM, in a non-invasive way is introduced (Pujol et al. 2015).

In order to acquire the information provided by DTI, it is necessary to perform a complex workflow to treat the images. Some of the techniques used to process diffusion images include: reduction of artifacts, distortions and motion correction; image quality control and image processing; tensor estimation; visualization and quantitative analysis, among others (Kingsley 2006a, 2006b; Soares et al. 2013). The pipeline used in the present work to include WM anisotropy through DTI is described below in Section 3.2.5.

3.2.3. MRI Image Processing for Model Construction

In order to develop 3D geometries from MRI images, it is necessary to follow a systemic process. A brief explanation of the procedure is shown in Figure 3.2. The first step is the registration of images, where the T1 and T2 images need to be registered together. There are a few software packages able to get this job done, like FMRIB's Software Library (FSL) (Smith et al. 2004), 3D Slicer, MedInria, ScanIP. We used FSL and ScanIP in our work. Afterwards, it is necessary to conduct segmentations of the image. In this procedure, different types of tissues are identified and masks are created. Once the tissues and regions of interest are recognized and segmented, they are put together to construct the 3D geometry. The keys for 3D geometry construction are to respect the position and place of each tissue piece. Furthermore, through FE (finite element), the meshes are generated. Then the meshed model is ready to be exported to a FE software package, where the physics of the problem is applied and calculations are carried out. Finally, the results need to be further processed in a post-process procedure. The whole procedure is shown in the flowchart below.

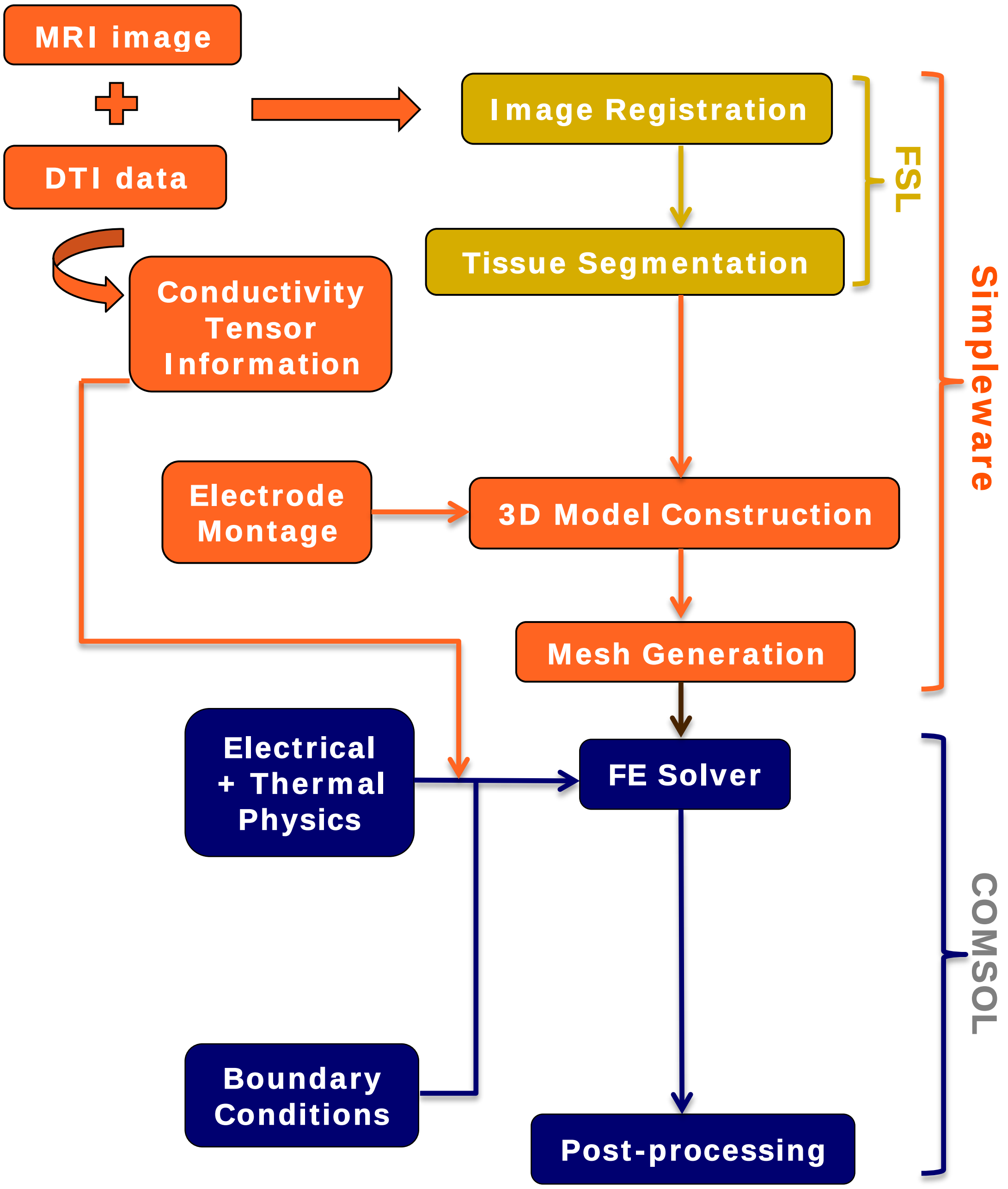

Figure 3.2. Flowchart showing the development of a realistic head model.

3.2.3.1. Image Registration

Within MRI datasets, the reconstruction of a 3D volume from the 2D images datasets is realized in order to obtain a correct 3D visualization and morphometric analysis (Positano 2005), thus recognizing a model-based object. In this process, a technique called image registration is required to align images. The images are mapped spatially and in relation to intensity. This is done in order that they stay in the same coordinate plane and, if there are any differences or feature overlaps, it is easier to visualize (Kostelec & Periaswamy 2003).

Methods of registration are characterized by four distinctive components and their diverse combinations. The four components are: feature space; search space; search strategy and similarity metric. The *feature space* is the step used to find common features among the images that can help to align the landmarks. The *search space* is the type of transformation $T(x)$, $f(x)=g(T(x))$, which should be used in order for two images to be aligned. It is a mapping of locations correlating the points of one image to new locations in another image. There are different types of transformation that can be chosen, such as rigid body, rotation plus translation, affine, projective, perspective and global polynomial. The type of transformation selected will influence the algorithm's registration nature. The *search strategy* defines the type of technique or method (Linear Programming techniques, relaxation method, etc.) that is going to be used during each step, after the first transformation is defined. Tied in with the search strategy comes the *similarity metric*, where a quantification of the transformations is realized. In this step the differences between the transformed source image and the target image will be quantified, with different choices available to ty and achieve that, such as mean-squared error and correlation (Brown 1992; Kostelec & Periaswamy 2003).

In short, a reference image and a floating image (image to be registered according to the reference image) are defined. A similarity function is evaluated among the images; hereafter an optimization algorithm evaluates the best transformation function, which will transform the floating image. If the result is acceptable, the registration is complete, otherwise, a new transformation is performed (Positano 2005).

Within FSL, two main functions may be used for the registration process. Both are fully automated tools, robust and accurate for brain image registration: the FMRIB's linear image registration tool – FLIRT, and the FMRIB's non-linear image registration tool – FNIRT (Jenkinson et al. 2002). These functions perform an alignment with the MNI152 space.

3.2.3.2. Tissue Segmentation

Image segmentation is intended to classify an image into homogeneous regions. These regions need to have a semantical meaning, boundaries that do not overlap and similar attributes, like texture, intensity, color and depth.

The tissue segmentation of MRI is going to divide and specify tissue types and anatomical structures. In the brain, one of the most important features for its segmentation is the intensity. There are a few methods which can be used to segment the brain, such as manual segmentation, methods based in intensity, atlas and surface, and hybrid segmentation methods (Despotović, Goossens & Philips 2015).

Prior to the MRI segmentation and besides the image registration and the brain extraction, it is important to realize the bias field correction (intensity inhomogeneity). It is a low-frequency artifact that causes a variation in the smooth signal intensity within tissues of the same physical properties. This is generated due to spatial inhomogeneity of the magnetic field. The FMRIB’s automated segmentation tool – FAST, from FSL, does the bias field correction and realizes generic tissue-type segmentation.

3.2.4. Realistic Head Modelling Development

Two realistic head models are used in this research. In the first case, model RHM_06, the geometry is built from MRI acquired from the available database *BrainWeb* (McConnell Brain Imaging Center). The images are based on the average of 27 co-registered MRI data from the same subject, generated by a MRI simulator. The images have a resolution of 1 mm^3 isotropic voxel and contain 181x181x217 slices in the transverse, sagittal and coronal axes. The T1 was generated using SFLASH with TR = 18 ms (repetition time), flig angle = 30º and TE = 10 ms (echo time). The T2 was acquired using dual echo spin echo, late echo with TR = 3300 ms, flip angle = 90º and TE = 35 ms (dual echo spin echo) and 120 ms (late echo). PD was obtained with dual echo spin echo, early echo with TR = 3300 ms, flip angle 90º and TE = 35 ms and 120 ms (Aubert-Broche, Evans & Collins 2006). In this case, the head model generated consists of six tissue layers; scalp; fat; skull; CSF; GM and WM. Figure 3.3 shows segmentation of these tissues.

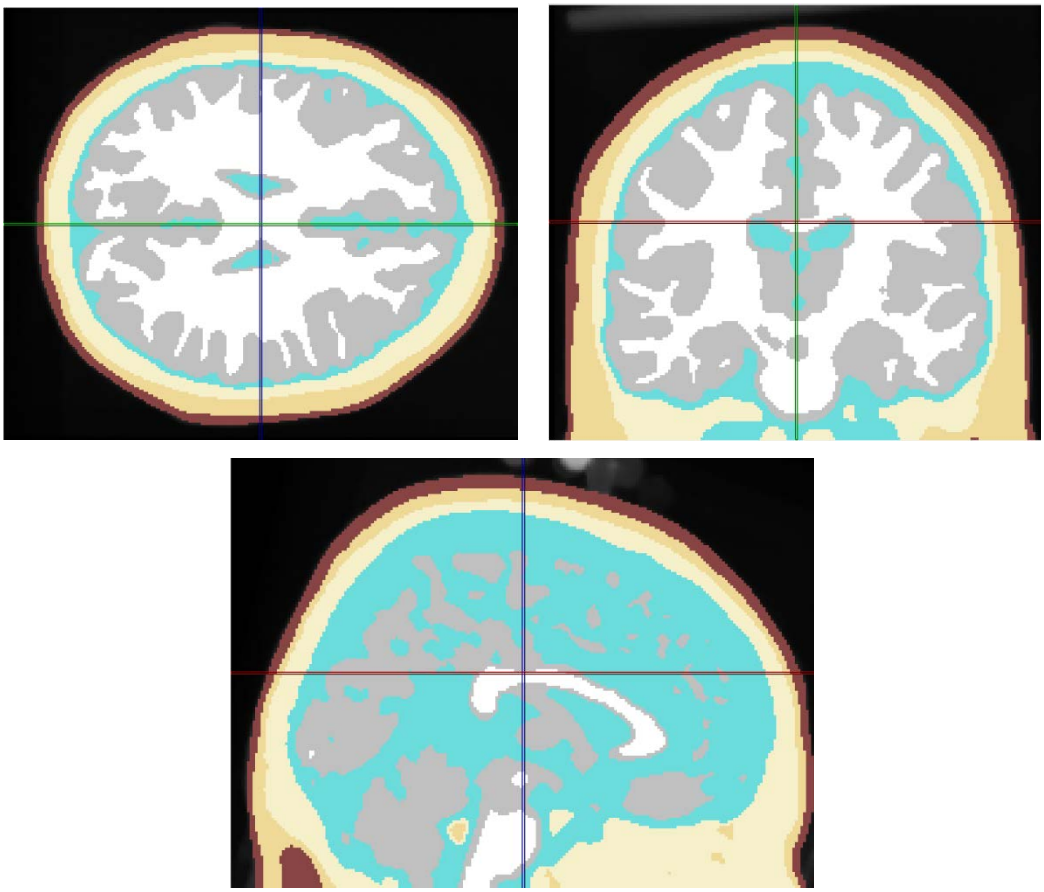

Figure 3.3. Model RHM_06, segmentation of six tissue layers for the images acquired from Brainweb; (a) transversal (b) coronal and (c) sagittal planes.

For the second model, RHM_17 model, the MRI was acquired from the available LONI ICBM database. The subject is the MNI_0591. The images were acquired with a 1.5 T Siemens scanner using GR pulse sequence. The MRI has a resolution of 1 mm^3 and 256x256x175 slices, with 1 mm thickness, TR = 22 ms and TE = 9.199 ms (*ICBM: International Consortium for Brain Mapping* 2014). For this set of images, the model generated consists of 17 tissue layers.

In the head model development, prior to the registration of images, a reorientation and a brain extraction through the FSL function fslreorient2std and BET (Brain Extraction Tool) (Smith 2002) are conducted. The purpose is to put the images in the same space coordinate and to separate brain regions from non-brain regions that are going to help in the registration and segmentation steps. Also, the skull stripping is realized using BET. FAST and BET, are used to generate the following masks: scalp, skull, CSF, GM and WM. Afterwards, the FLIRT tool is used. The T1 image is selected as the reference image and the T2 is the floating image. The transformations applied are rigid-body and affine.

In the tissue segmentation, semi-automatic tools from FSL and Simpleware are used. T1 images are used to identify and segment scalp, fat, skull, CSF, GM, WM, and, for the second model, eyes (sclera, lens, muscles), muscles of mastication; while T2-weighted and Proton Density are used to classify inner skull and CSF boundaries.

FAST and BET, are used to generate the following masks: scalp; skull; CSF; GM and WM. Posteriorly, fat is semiautomatically generated using the ScanIP module from Simpleware 4.3 (Simpleware Ltd.).

For the second model, the FMRIB’s integrated registration and segmentation tool – FIRST, from FSL, is used for the segmentation of subcortical brain structures, therefore, the mask for regions such as thalamus, brainstem, hippocampus, amygdala, putamen, pallidum, caudate, are generated. To run FIRST, the inputs used are the T1 image and a model provided from FSL. It registers the image to the MNI152 template and fits the structure models to the image and boundary corrections.

Once the tissues had been segmented, 17 in this model, several semi-automatic and manual corrections needed to be done. At first, a CAD+ module (Simpleware Ltd.) is used to put all the tissue masks together as a whole head model. Thereafter, the masks are exported to ScanIP, where automatic image processing techniques are used to correctly place one tissue adjacent to another and better smooth the layers. Techniques such as dilate, erode, Gaussian filter and FloodFill are used. Later on, some manual corrections are required to remove any floating islands.

3.2.5. Inclusion of WM Anisotropy through DTI

White matter anisotropy was included in the model RHM_17. DTI images from the subject MNI_0591 are acquired from the LONI ICBM database. The images were acquired with a 1.5T Sonata Vision Siemens scanner using SE/EP pulse sequence. The DTI has a resolution of 2.5 mm^3 and 96 x 96 x 2100 slices, with 2.5 mm thickness, TR = 8000 ms, TE = 94 ms and 90º of flip angle (*ICBM: International Consortium for Brain Mapping* 2014).

The images were processed to convert diffusion information into conductivity information. The pipeline used in this study followed these references: (Bai 2012; Leigh Morrow 2016; Tromp 2015) and is described here. The acquired images were in DICOM (Digital Imaging and Communications in Medicine) format. At first, it was necessary to convert the images to a usable format. Because FSL will be used, the images were converted to NIfTI (Neuroimaging informatics Technology Initiative) through the software dcm2nii from MRIcron (Rorden, Karnath & Bonilha 2016). Hereafter, the quality of the data was examined using fslinfo and fslview by FSL. The images have a dimension of 96 x 96 x 60 and 35 volumes in total, from which 5 volumes were acquired without diffusion weighting. Afterwards, the images were corrected due to distortions.

Eddy currents are one type of distortion caused due to changes in the magnetic field. They are electrical current loops induced within conductors. The function eddy_correct from FSL will remove eddy currents and simple head motion. After that, it is necessary to do some gradient direction rotation at b-vector file. Therefore, a script was used that realizes eddy_correct and b-vector rotation at the same time (Glasser 2009). Afterwards, BET was applied in order to remove any non-brain tissues and dtifit was used to fit the tensors. In this step, the outputs were the three eigenvalues and eigenvectors and the fractional anisotropy (Figure 3.4). These results were used in a Matlab script adapted from Bai (2012) to transform diffusivity information in conductivity information. Once the conductivity is acquired, this information is imported for modelling in COMSOL.

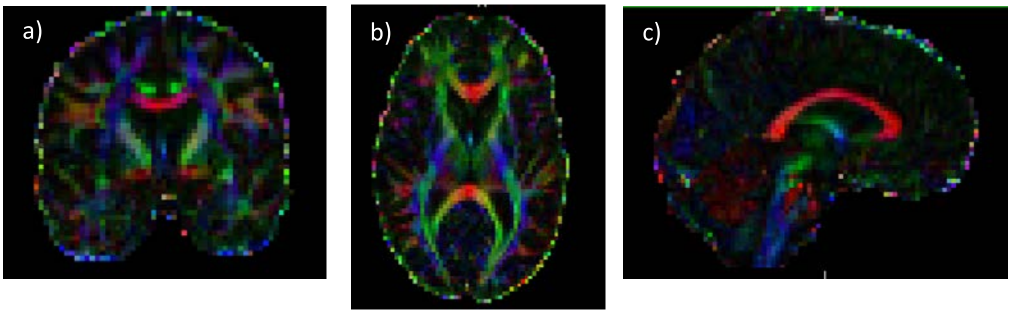

Figure 3.4. The directional fractional anisotropy of subject MNI_0591, in the planes (a) coronal, (b) axial and (c) sagittal. The encoded RGB colour scheme means red (right-left), green (anterior-posterior) and blue (superior-inferior).

3.3. Electrode Modelling

Three conventional electrode configurations (BF, BL, RUL) normally used during the practice of ECT are modelled (Figure 3.5). They are constructed within CAD+. The mask of the electrodes is subtracted from the scalp mask, in order that the electrodes are able to be geometrically placed over the scalp tissue.

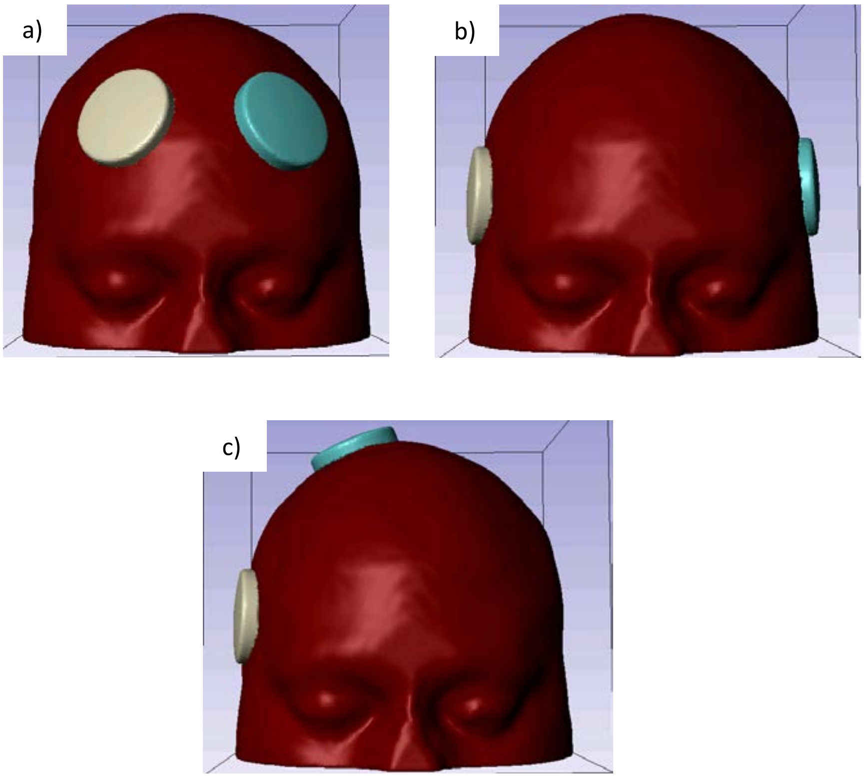

Figure 3.5. ECT electrode montage (a) bifrontal - BF, (b) bilateral frontotemporal - BL and (c) right unilateral – RUL.

BF and BL placements are bilateral stimulation, whereas RUL is unilateral. For SHM, circular electrodes with 5 cm diameter are built within COMSOL. For RHM, the electrodes are built in the software CAD+ (Simpleware Ltd.). Steel is considered as the electrode material, with $\sigma = 9.8 \times 10^5 (\mathrm{S/m})$ and $\mathrm{k} = 42\ (\mathrm{W/(m.K)})$. In RHM, the placements of the electrodes are as follows: for BF electrode configuration, both electrodes are localized 5 cm above the outer angle of the orbit, parallel to the sagittal plane (Lee et al. 2012); for BL, both electrodes are positioned 2.5 cm above the midpoint of the line that connects external canthus and tragus, at the frontotemporal position (Casarotto et al. 2013; Lee et al. 2012; Weiner 2002); and for RUL, the electrodes are positioned on the right hand side of the head, one 2.5 cm to the right of vertex (active) and the other in the same position as right BL placement (Lee et al. 2012). Analogous electrode positions are chosen in the case of SHM.

The electrolyte gel is largely displaced when the electrodes are pressed against the scalp. Its aim is to stabilize the impedance of the electrode-scalp interface (Lee et al. 2012). This is already considered in the computational model. Thus, in this study, the gel is not directly modelled.

3.4. Mesh Generation

The generation of a mesh is the pre-requisite to apply the finite element method. It represents a discretized geometry being expressed into small units of simple shapes. In the models generated in this work, it also represents the electric and the thermal properties of the head volume conductor. The mesh is generated using the package COMSOL and using the tetrahedral technique. To choose the size of the mesh, a convergence analyses is conducted. For the SHM with five layers, considering that it is a simplified model, not much difference was found when doing the mesh analysis. The mesh used consists of 48,349 tetrahedral elements. For the six layers SHM, the adopted mesh consists of 93,171 tetrahedral elements.

For the RHM, the mesh was generated under the umbrella of ScanIP. A convergence analysis is conducted. The chosen mesh has the compound coarseness set to -22, which has the following parameters: characteristic lengths with target minimum and maximum edge length of 2.04 and 4.96 mm respectively and target maximum error (distance remeshed surface is allowed to move from original mesh) of 0.1 mm; surface constraints with surface change rate of 44 and target number of elements across a layer of 0.78; volume elements generation with internal change rate of 30 and quality optimization cycles of 5; an additional quality improvement with metric scaled Jacobian of 0.1; and maximum off-surface distance, that is, fraction of local edge lengths of 0.2. These specifications generate meshes that consist of approximately 2 million tetrahedral elements (RHM_06). Figure 3.6 shows an image of the mesh generated, on the external layer and the electrodes. Finally, the mesh model file is exported to COMSOL Inc., where the physics and boundary conditions are applied. Each model took approximately 17 minutes to run in a 32 GB ram, 4-core laptop workstation.

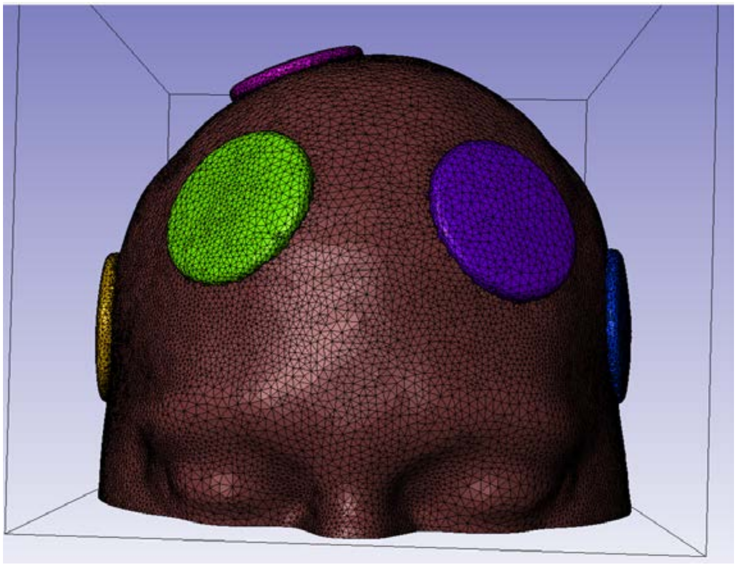

Figure 3.6. Mesh generated for RHM, showing scalp and electrode position.

3.5. Chapter Summary

The development of the human head models used in this study is introduced. It begins with simpler spherical head models, where the geometry parameters and configurations of the spherical models are explained. As examples, three spherical models are described in detail. The most popular realistic head models derived from MRI are also developed. As part of the realistic head model development, a brief explanation about MRI and the image process used to construct the head model is provided. The main procedures such as image registration, tissue segmentation, mesh generation and computation are also explained. Table 3.1 summarizes the types of models used in the present work and their parameters. Also, the modelling of the electrodes is covered at the end.

Table 3.1. Summary of the human head models.

MODEL	ACRONYM	SOFTWARE MODELLED	PHYSICS - METHOD	FUNCTION
Spherical human head model - 4 layers	SHM_04	COMSOL	Thermal + electrical – FEM	T_{max} behaviour; comparison among electrode configuration
Spherical human head model - 5 layers	SHM_05	COMSOL	Thermal + electrical – FEM	Inclusion of thermal skull anisotropy
Spherical human head model - 6 layers	SHM_06	COMSOL	Thermal + electrical – FEM	Inclusion of thermal and electrical skull anisotropy
Realistic human head model – 6 layers	RHM_06	FSL + Simpleware + COMSOL	Thermal + electrical – FEM	Realistic model with thermal and electrical skull anisotropy
Realistic human head model – 17 layers	RHM_17	FSL + Simpleware + COMSOL	Thermal + electrical – FEM	Inclusion of DTI (WM anisotropy) and brain tumor

4. BIO-HEAT TRANSFER MODEL OF ECT: ISOTROPIC SPHERICAL MODEL

4.1. Introduction

The idea of this study is to investigate the temperature increase due to ECT electrical stimulation. In this chapter, simple spherical time-dependent head models are built and considered. In these models, the Pennes bio-heat transfer equation and the Laplace equation of electric field are solved to simulate how the ECT affects temperature. The behaviour of temperature and the maximum temperature are investigated.

4.2. Methods

4.2.1. Spherical Head Model

The head model considered in this part is a simplified one. A spherical four layers head model (SHM_04) is built using the software COMSOL *Multiphysics* ® 4.1 (COMSOL Inc.). The diameter of the external layer is considered to be 21 cm; and the thickness of scalp, skull and CSF are 1 cm each. The mesh is generated using the finite element model method, which is also used for the calculation of such problems.

Each layer is considered to represent one different tissue of the human head: scalp; skull; CSF and brain. The electrical and thermophysical properties (Collins et al.

2004; Datta, Elwassif & Bikson 2009) of these tissues are considered according to Table 4.1, where k and σ are the thermal and electrical conductivity, respectively; ω_b is the blood perfusion rate, Q_{met} is the metabolic heat source, ρ is the density and c is the heat capacity.

Table 4.1. Electrical and thermophysical properties of head tissues.

	k (W/(m.K))	***σ*** (S/m)	***ρ*** (Kg/m3)	***cp*** J/(Kg.K)	***Qm*** (W/m3)	***ωb*** (1/s)
Scalp	0.39	0.465	1125	3150	363	0.00143
Skull	1.15	0.01	1850	1300	70	1.43e-4
CSF	0.61	1.654	1000	4200	0	0
Brain	0.57	0.2	1035.5	3680	10437	0.08

The electrode configurations considered for all models are the ECT conventional BF, BL and RUL as described in the previous section.

The electrical conductivity assigned to the electrode is 9.8×10^5 S/m. The electrolyte gel is largely displaced when the electrodes are pressed against the head. Its purpose is to stabilize the impedance of the electrode-scalp, which was already assumed in the computational model (Lee et al. 2012). Therefore, in this model no electrolyte gel is applied to the electrode surface.

4.2.2. Heat Transfer Model

The physics applied to these models involves heat transfer and electrical potential simultaneously. The bio-heat transfer equation is combined to Laplace equation (Datta, Elwassif & Bikson 2009; Elwassif et al. 2006) (Equation 4), as described in Section 2.

$$\rho c \frac{\partial T}{\partial t} = \nabla(k\nabla T) + \omega\rho_b c_b (T_a\text{-}T) + Q_m + \nabla|\sigma\nabla V| \,. \qquad (4)$$

In this equation, T is the local temperature of the tissue, c_b is the specific heat of the blood and T_a is the arterial blood temperature.

For the thermal physics, time dependent domain is applied. The range simulated varies from 0 to 8 s (ECT safety values).

4.2.3. Initial and Boundary Conditions

Initial and boundary conditions are necessary for defining and solving the heat and electrical problems. IC and BC used in the models are described in Section 4.2.3.1 which states the conditions for the thermal physics, and Section 4.2.3.2 which describes the electrical physics.

4.2.3.1. Thermal Physics

For the thermal physics, heat flux (Newton's law of cooling) (Equation 7) is assigned to the external boundaries of the head model for the external BC:

$$\text{-}k \cdot \frac{\partial T}{\partial n} = h \cdot (T_{amb}\text{-}T). \qquad (7)$$

where h is the heat transfer coefficient, assigned as $4 W/m^2.{}^oC$; and T_{amb} is the external temperature, assigned as $24\ {}^oC$. In the interfaces of the head tissues, conduction occurs between two layers. Furthermore, the following parameters from are applied: $\rho_b = 1050\ Kg/m^3$, $c_b = 3600\ J/(Kg.{}^oC)$ and $T_a = 36.7\ {}^oC$. The initial temperature is assigned as T_{amb} at electrodes and $37\ {}^oC$ at tissue layers (Datta, Elwassif & Bikson 2009).

4.2.3.2. Electrical Physics

For the electrical physics, the exposed boundaries are considered electrically insulated and are represented by Neumann BC, $n \cdot (\sigma\nabla V) = 0$. In the inner boundaries, between regions of different tissues, continuity of the normal component of the current density occurs. The exposed surface of the cathode is assigned Dirichlet ($V = 0$ volts) BC, whilst the exposed surface of the anode is assigned Dirichlet ($V = V_0$ volts) BC (Datta, Elwassif & Bikson 2009), where V_0 is the input potential, set as a sinusoidal waveform with frequency of 57.36 Hz (Casarotto et al. 2013). The value of potential is equivalent to 500 mA or to 800 mA peak current on the exposed surface of the anode (Lee et al. 2012).

4.3. Simulation

The simulation results show an increase in the temperature around the areas where the electrodes are located (Figure 4.1). It is expected intuitively that a point should experience the maximum temperature. For all these configurations and simulations, a temperature graph is plotted against time for that point (Figure 4.2). Also, a line was traced from this point to the opposite side of the head model and to the middle (Figure 4.3). The temperature graph is plotted against the arc length for different times. Figure 4.4 shows the graph for times of 0 s, 2 s, 4 s, 6 s and 8 s. In this way, it is possible to analyze the behaviour of temperature through the different layers of the head.

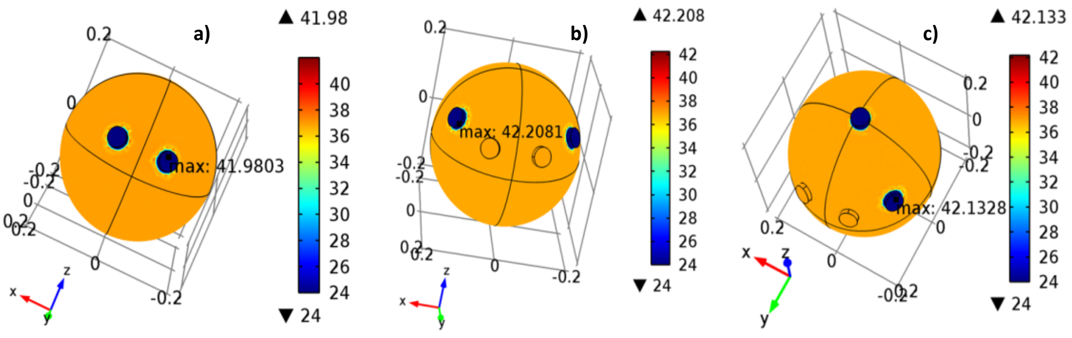

Figure 4.1. Spherical head model – SHM_04 a) BF, b) BL and c) RUL configurations showing the temperature distribution at 8 s.

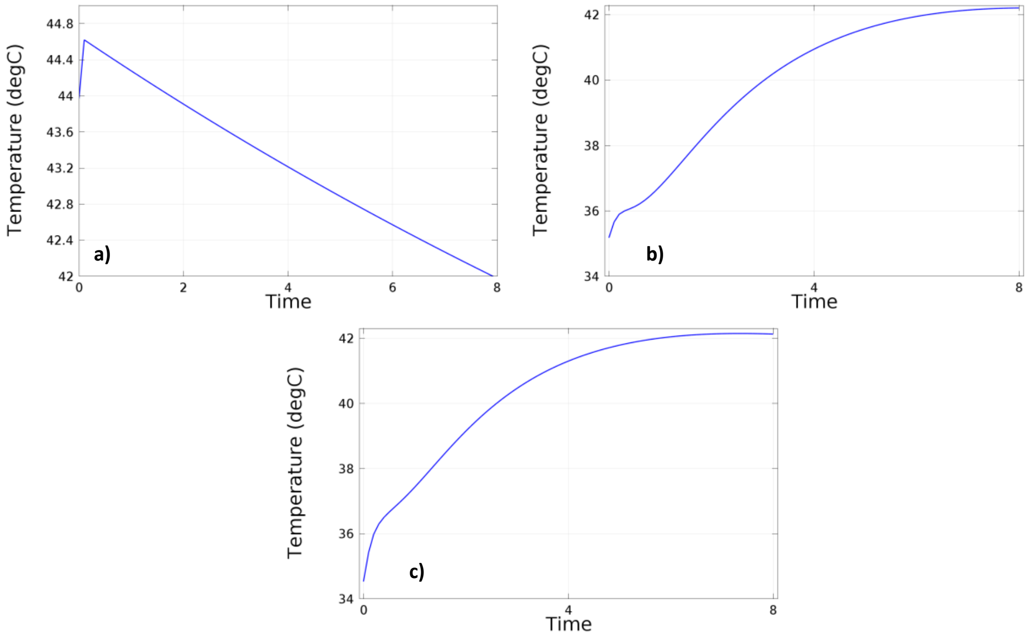

Figure 4.2. Graphic of temperature (ºC) along the time (s) for the point of maximum temperature, for 800 mA. a) BF, b) BL and c) RUL.

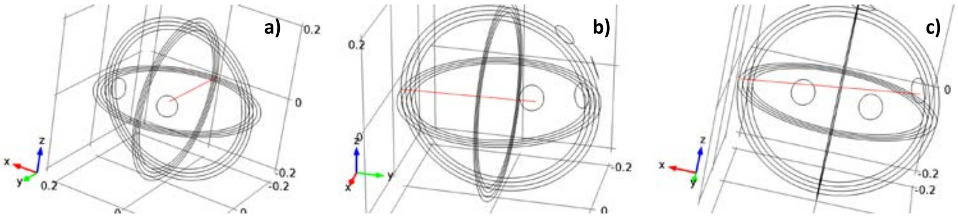

Figure 4.3. Wireframe of the spherical head model showing the position of the line used to analyse the temperature in the configurations a) BF, b) BL and c) RUL. The first point of this line represents the maximum temperature.

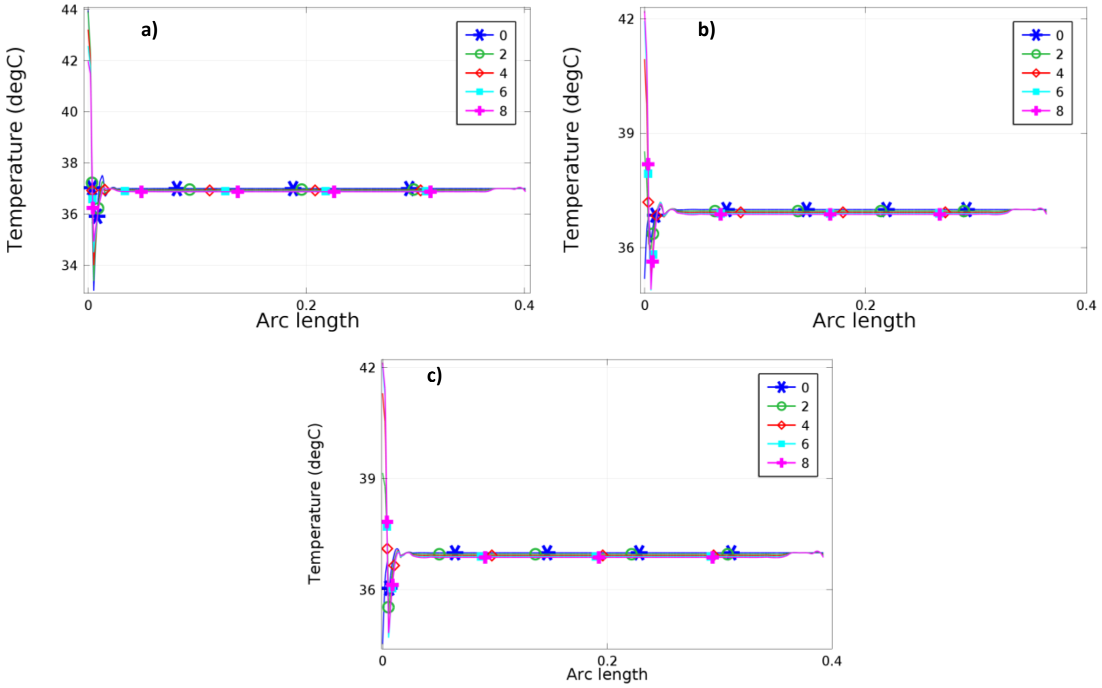

Figure 4.4. Graphic of Temperature (ºC) along the arc length (Figure 4.3) showing the distribution of temperature in 5 different times 0 s, 2 s, 4 s, 6 s and 8 s. a) BF, b) BL and c) RUL.

In the case of 800 mA input with the BF configuration, the maximum temperature reached is 44.6 ºC on the scalp. The temperature on the skull, CSF and brain oscillated slightly but remained around the body and blood temperatures.

In the case of BL configuration, the temperature increases gradually and the maximum temperature reached is 42.21 ºC on the scalp. On the other layers of the head, such as skull, CSF and brain, the temperature stayed close to the body and blood temperatures.

For the RUL configuration, the maximum temperature rises gradually and reaches 42.13 ºC in 8th seconds, being the maximum temperature. As in the other configurations, the skull, CSF and brain layers demonstrate a temperature close to the body and blood temperatures. For the case of 500 mA peak current, the maximum temperature reached is 42.12 ºC in 8 seconds.

In Figure 4.1 b) and c), the electrodes used in the BF configurations are shown. These were considered to be thermally and electrically isolated.

4.4. Discussions

This simulation study investigates the distribution of temperature due to electrical stimulation in the practice of ECT and finds that brain temperature is not increased. Only localized scalp temperature produces a significant rise, but still within safety limits.

The magnitude of temperature increases is critically dependant on the electrical and thermal properties and stimulation settings. The temperature up of 44.6 ºC for the BF configuration on the scalp, decreases when it reaches the skull layer. This is due to the skull having an electrical conductivity 46.5 % smaller and a thermal conductivity almost three times bigger than the scalp. In that respect, these two layers work together to protect and isolate the brain from electrical shock and high temperatures. The same behaviour occurs with the BL and RUL configurations. In our study, we can see that the temperature of the brain is not affected by electrical stimulation at all.

Comparing the input amplitudes applied in the RUL configuration, in the case of 500 mA peak current, the maximum temperature reached is 42.12 ºC; while for the case of 800 mA, the maximum temperature is 42.13 ºC. Given this 0.01 ºC almost imperceptible difference, it seems that the input amplitude does not influence the temperature distribution. However, according to Elwassif et al. (2012), the temperature increase depends on the root-mean-square voltage applied and it is not waveform detail dependent.

The BL and RUL configurations exhibit a similar performance, when compared with the BF configuration, as shown in Figure 4.2 b) and c). This could be due to the proximity between the electrodes given that the electrodes at BF are much closer than at BL and RUL. Also, the BC applied to the electrodes making the temperature there be equal to 24 ºC and the short distance between the electrodes at BF configuration, explains the drop at Figure 4.2 a.

Apart from electrical stimulations, temperature increase can also result from neuronal activation associated with behavioural conditions, and pharmacological drugs can significantly increase the brain temperature (Elwassif et al. 2006). Our model in this study is a simplified one and the influence of anaesthesia, all thermal boundary conditions (e.g. radiation, respiratory heat loss) and other parameters such as electrical and thermal tissue inhomogeneity, were not considered. The difference in electrode configurations is also going to influence different parts of the head in a realistic head model, as observed by Datta, Elwassif and Bikson (2009).

As the temperature moves above 40 ºC, this can cause damage and tissue ablation (Elwassif et al. 2006). Such high temperatures inflicted on the scalp should be analysed further to guarantee that the practice of ECT is safe.

4.5. Conclusions

In this chapter, thermo-electrical spherical models (SHM_04) show the temperature behaviour when electrical stimulation is applied. Two different input currents are considered. The simulations show that the temperature of the brain is not affected by the electrical stimulation and the highest temperatures happen only on the scalp layer in local electrode areas. The models built here are simplified isotropic spherical models. In the following chapters, anisotropic and realistic geometries will be considered for further analysis. An alternative technique is used to represent the spherical models. It was developed as a resistive-capacitive network and works as a part-validation for the FEM models. The description for this technique is shown in Appendix I.

5. SPHERICAL HEAD MODEL WITH ANISOTROPIC THERMAL CONDUCTIVITY IN SKULL

5.1. Introduction

The influence of anisotropic thermal skull is examined using a five layers spherical head model of ECT. The forward solutions are computed for both isotropic and anisotropic conductivity of a spherical head model using finite element analysis. The results are evaluated using the temperature (T) and temperature gradient (GradT - ∇T) within these tissues.

As a general rule, some regions of the head, according to the structure of the tissue, are good heat conductors and others are not. The temperature behaviour should be evaluated according to its thermal conductivities. As the first trial, a simplified spherical head model is used in this study, where the skull has anisotropic heat conductivity. The simulated study demonstrates heat transferrance and temperature changes in each of these head tissues.

5.2. Methods

5.2.1. Modelling Details

A spherical head model with five layers, model SHM_05, (Figure 5.1) is used. The details of the SHM_05 model is presented in Chapter 3, Section 3.1. The head tissues included in this model are: scalp; skull; CSF; GM and WM. The mesh is generated using COMSOL software and the tetrahedral technique. There are a total of 48,349 tetrahedral elements in the model.

The thermo-electrical model is described using the BHTE equation with the Laplace equation, as described in Section 2.4. The electrical and thermophysical properties are shown in Table 4.1.

Both thermal and electrical IC and BC are assigned, as described in Section 2.4.1. For the thermal BC, heat flux (Equation 7) is applied externally, with $h = 4\ W/m^2.\ °C$ and $T_{amb} = 24\ °C$. Conduction occurs in the interfaces between the layers. Initial temperature (T_0) is considered to be $36.7\ °C$. The parameters for blood perfusion are assigned as $\rho_b = 1050\ Kg/m^3$, $c_b = 3600\ J/(Kg.°C)$ and $T_a = 36.7\ °C$ (Datta, Elwassif & Bikson 2009).

For the electrical physics, the external boundaries are considered electrically insulated (Equation 5) and continuity (Equation 6) occurs in the inner boundaries. The exposed surface of the anode is assigned Dirichlet ($V = V_0\ volts$) BC, where V_0 is the input potential set as a sinusoidal waveform with 60 Hz of frequency and amplitude equivalent to 500, 650 and 800 mA. Whereas, the exposed surface of the cathode is assigned the Dirichlet boundary ($V = 0\ volts$) condition.

The electrodes modelled in these models are BF, BL and RUL, as defined in Section 3.3.

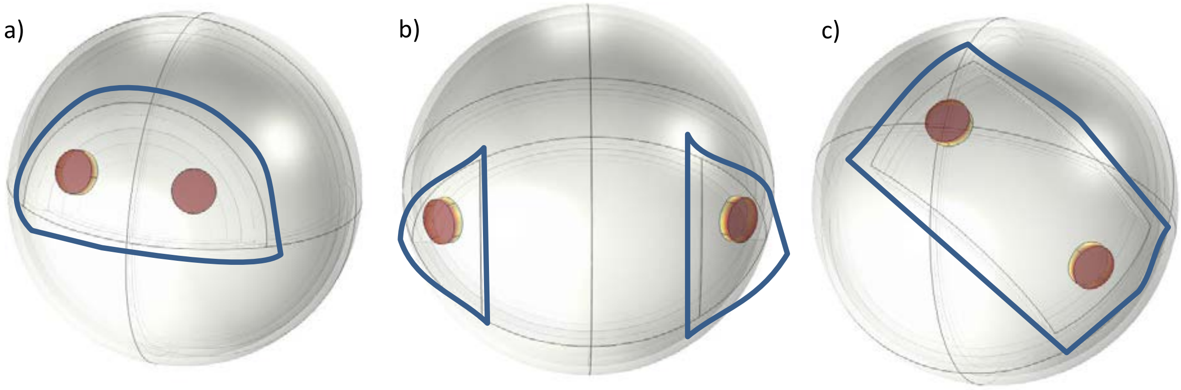

Figure 5.1. Spherical head model with five layers, for different electrode montages (a) BF, (b) BL and (c) RUL. The region marked in blue specifies the ROI.

5.2.2. Thermal Skull Anisotropy Conductivity

According to De Munck (1988); Marin et al. (1998); Rush and Driscoll (1968); van den Broek et al. (1998), the skull has an electrical anisotropy ratio of 1:10. Wolters et al. (2006) considered a wide range of values to estimate the overall effect of electric and magnetic fields and studied the influence of anisotropic tissue conductivity on forward EEG and MEG.

Section 2.5.3 shows that there is a linear relationship (Equation 17) between electrical and thermal conductivity tensors. Therefore a correlation based in VC (Equation 11) and Wang (Equation 13) was imposed to calculate the radial and tangential anisotropy conductivity. In the same manner, for VC, the volume of the thermal conductivity tensor is maintained, given that the geometric mean of the eigenvalues is preserved, i.e.,

$$\frac{4}{3}\pi k_R (k_T)^2 = \frac{4}{3}\pi k_{iso}^3. \tag{18}$$

Likewise, for Wang, the product of radial and tangential conductivity stays constant and equal to the square of the isotropic thermal conductivity, i.e.,

$$k_R k_T = k_{skull}^2, \tag{19}$$

where k_R and k_T are the radial and tangential thermal conductivity, respectively.

This assumption was made because there is no available information on thermal anisotropy conductivity of the head. The analysis considers the known common isotropic thermal conductivity, valued as *k = 1.15 W/m.K* (Datta, Elwassif & Bikson 2009), and uses VC (Equation 18) and Wang (Equation 19) to set up the eigenvalues for the anisotropic case. A wide range of values considered are shown in Table 5.1. The electric conductivity is maintained as a constant isotropic, because the purpose is to analyze the heat transfer behaviour.

Table 5.1. Simulated values for the skull thermal conductivity tensor eigenvalues for the VC and Wang. Units of k in W/m.K.

Ratio	**Skull tensor eigenvalues**			
	Volume Constraint		Wang Constraint	
	k_R	k_T	k_R	k_T
1:1 (iso)	1.15	1.15	1.15	1.15
1:2	0.725	1.45	0.829	1.595
1:5	0.393	1.965	0.515	2.568
1:10	0.2478	2.478	0.364	3.632
1:100	0.0533	5.33	0.115	11.5

5.2.1. Measures for Analysis

The maximum temperature (T_{max}) with respect to time is selected as one of the measures for analysis. A radial line, starting from the position where T_{max} happened, is used to study the behaviour of temperature.

A ROI (Figure 5.1) is defined to evaluate the behaviour of *T* and of *GradT* near the electrodes, reaching all five layers. Furthermore, descriptive statistics of the magnitude of *GradT* (median, 25th and 75th percentiles, maximum and minimum) are calculated from ROI.

The relative error (RE) of *GradT* is also employed to provide the relative difference between isotropic and corresponding anisotropic solutions. This statistical measurement is defined as below:

$$\boldsymbol{RE} = \sqrt{\frac{\sum_{i=1}^{n}\left(\nabla T_i^{iso} - \nabla T_i^{aniso}\right)^2}{\sum_{i=1}^{n}\left(\nabla T_i^{aniso}\right)^2}} \tag{20}$$

where n is the number of samples in the respective ROI and ∇T^{iso} and ∇T^{aniso} the ith component of ∇T in the isotropic and anisotropic cases, respectively (Lee et al. 2012).

5.3. Simulations and Results

The SHM_05 models generated in COMSOL are used to analyse the thermal field behaviour due to ECT electrical stimulation. The results for the three electrode montages and the range of thermal anisotropy skull conductivity are shown below.

5.3.1. Maximum Temperature

At first, the behaviour of temperature along time was evaluated. Only a slight linear increase in the temperature occurs, as ECT has been a safe practice for decades. T_{max} situated in the skull is calculated and compared among the isotropic and anisotropic cases for the three electrode configurations and the three different electrical inputs (500 mA, 650 mA and 800 mA). For all montages, the T_{max} is reached at the 8th second, and as soon as the input current increased, the temperature also rose.

The BF and BL configurations demonstrate a similar behaviour, where the isotropic case has the maximum temperature. In these cases, as long as the thermal anisotropy ratio is increased, the temperature dropped slightly, whereas for the RUL configuration, the opposite occurred. The maximum temperature is reached at the maximum ratio (1:100) and the isotropic model has the minimum increase. Applying both the volume constraint and Wang constraint, the T_{max} of 36.72 ºC, 36.76 ºC and 36.84 ºC are reached for the inputs of 500 mA, 650 mA and 800 mA, respectively, for each electrode configuration. Figure 5.2 shows the behaviours of the T_{max} in the skull, over time, for the three electrode configurations using Wang constrain.

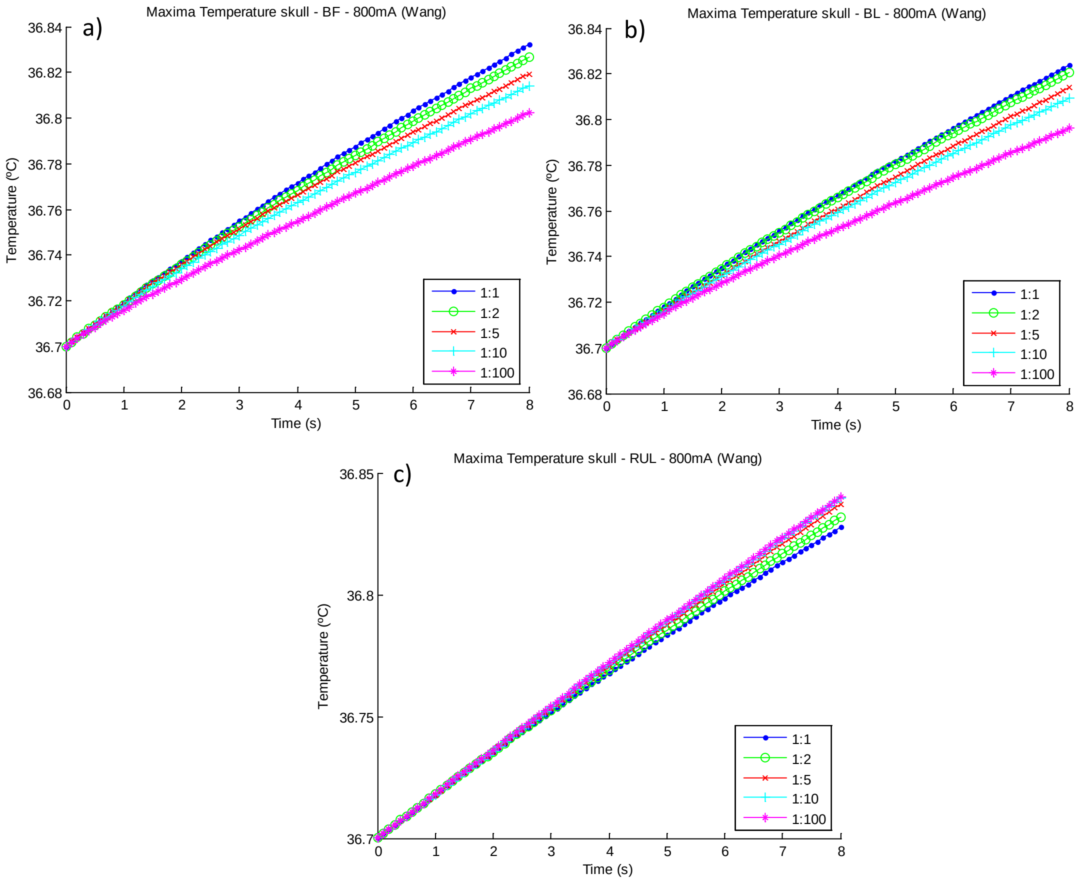

Figure 5.2. Plot of the point of maximum temperature in the skull, over time, for isotropic and anisotropic (Wang) cases, for the three electrode configurations (a) BF, (b) BL and (c) RUL. Shown here for 800 mA.

According to the current input applied, different increases in temperature happen. In the skull T_{max} in a 8 second period a linear increase in the temperature is observed. Applying 500 mA input, an increase of approximately 0.05 % happens, for both VC and Wang constrains. For 650 and 800 mA input, the increase is of, approximately, 0.14 % and 0.35 %, respectively.

For the short period of ECT time, only a slightly increase in the temperature occurs. Even though, according to the electrode configuration and the value of thermal conductivity used, the rise is different. The percentage difference of temperature related to T_0 is evaluated. The BF isotropic case, for all the inputs, is the one which has the biggest increase. That is not surprising, given that the electrodes are closer from each other. For the isotropic cases, the RUL is the one with higher increase in temperature. Moreover, the smallest temperature increase happened for all BL cases as shown in Figure 5.3a.

When comparing the percentage difference among isotropy and anisotropies (Figure 5.3b), for VC, BL had the lowest increase in temperature, except the case of ratio 1:100. For that last case, RUL has the smallest temperature rise while BF has the biggest. However, for the others anisotropy ratio (1:2, 1:5 and 1:10), RUL has the highest T increase. For Wang cases (Figure 5.3c), BF who had the highest rise; while RUL had the smallest increase, except at ratio 1:2, that was BL.

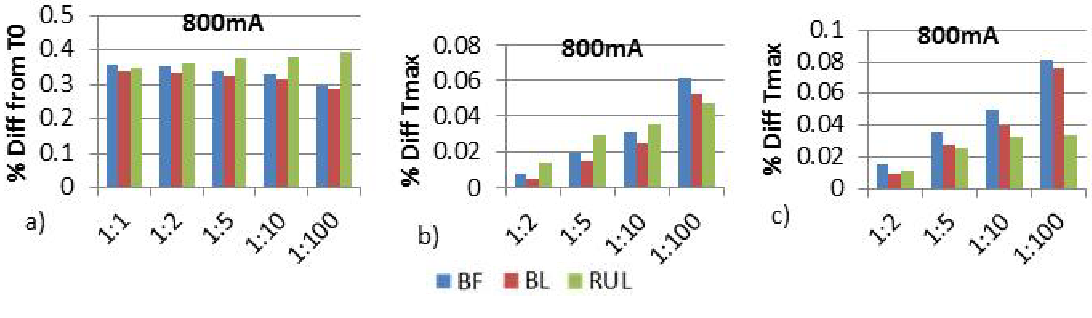

Figure 5.3. Percentage difference from T_{max} at t = 8 s comparing with T_0 (a); and isotropic x anisotropic analysis (b) for volume constraint and (c) for Wang constraint. Shown here for 800 mA input case. The behaviour for inputs 500 mA and 650 mA are equivalent.

5.3.2. Gradient of Temperature

Figure 5.4 shows the descriptive statistics of the temperature gradient magnitude for ROI of skull and CSF at t = 8 s with VC. Considering the skull as anisotropic, it is going to influence the gradient of temperature in the skull and CSF layers. The values in the scalp, GM and WM layers, have inconsiderable variations when the thermal conductivity value is modified.The same applies in the entire ROI (graphics not shown here).

At the skull layer, the highest values occur for the isotropic case and the smallest values occur for the largest ratio, in the BF and BL montages. The RUL behaviour is not linear; it has the biggest value in the ratio 1:5, whereas the smallest value occurs in the ratio 1:100. The CSF layer, when compared with the skull, has the opposite behaviour for BF and BL montages. In these cases, the isotropic case has the smallest magnitude and, as soon as the anisotropy ratio increases, the magnitude also rises. For RUL, the isotropic case has the highest *GradT*, however the minimum value is at the ratio 1:10.

A comparison between skull and CSF with VC is shown in Figure 5.5. The behaviour of magnitude of *GradT* while increasing the anisotropy ratio, is opposite, when comparing these two layers. *GradT* skull rises, while CSF decreases, and vice-versa. The demeanour for Wang is equivalent.

The magnitude values for CSF with Wang constraints are larger than for VC; whereas the magnitude values for the skull are smaller with Wang's constraint applied and higher for VC. The highest magnitude of *GradT* occurs in the scalp, which reaches approximately 221.65, 200.47 and 823.82 K/m at BF, BL and RUL, respectively. While the minimum values occur in the WM, they reach values between 8.77 to 12.39 K/m.

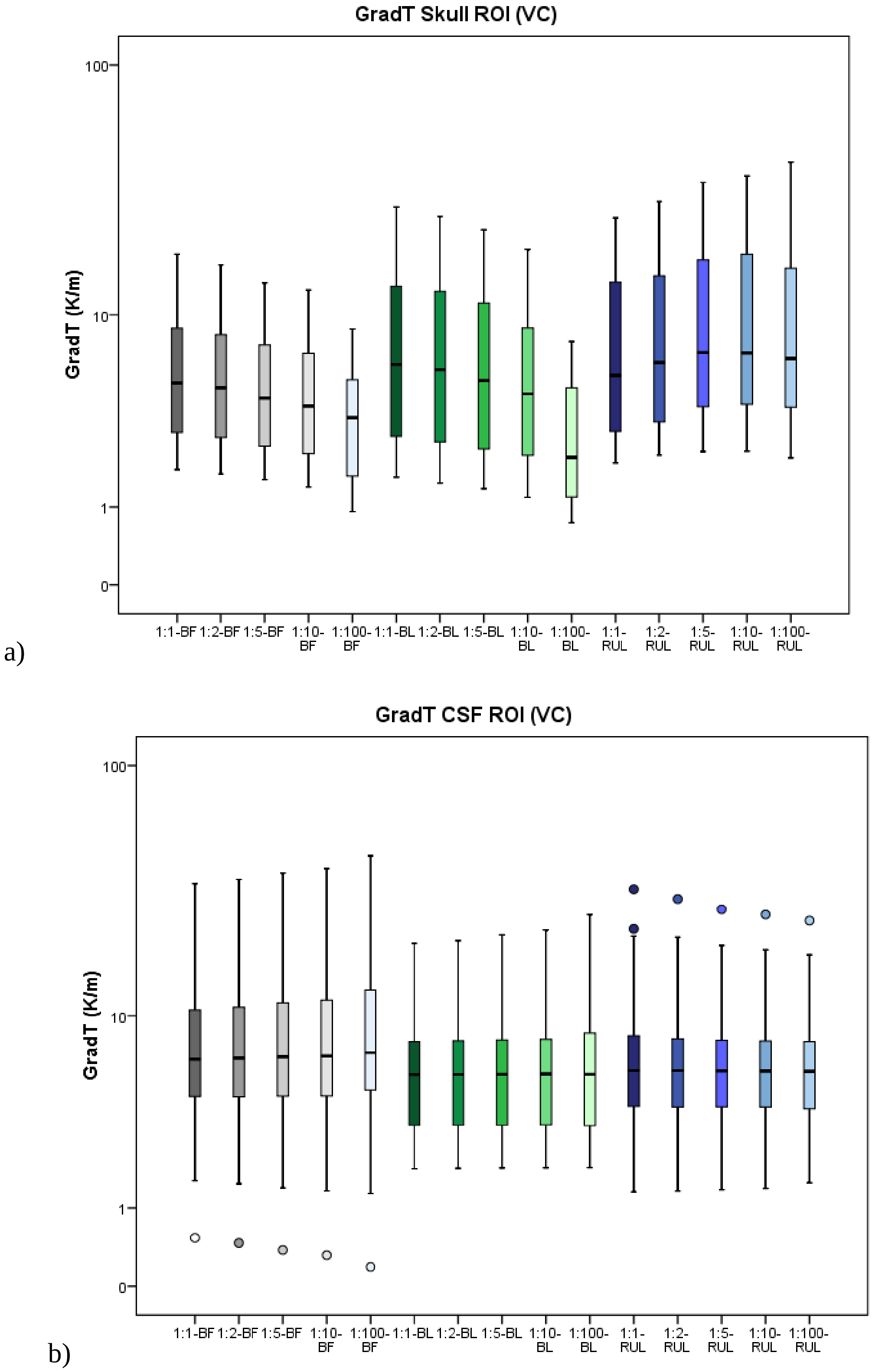

Figure 5.4. Descriptive statistics of magnitude of GradT for (a) skull and (b) CSF. BF (grey), BL (green) and RUL (blue); isotropic to anisotropic goes from darker to lighter colour tone. VC 800 mA input at t = 8 s.

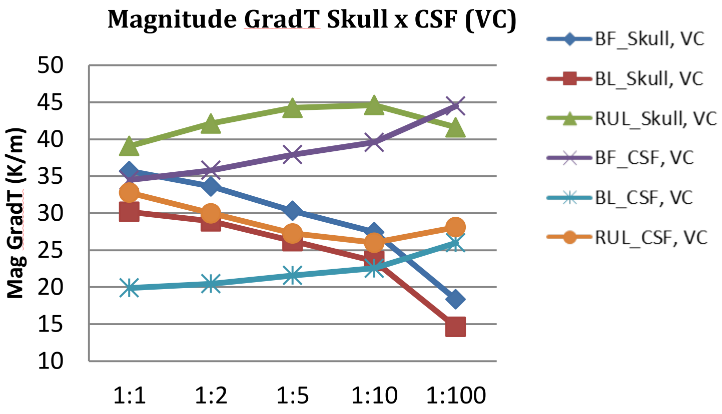

Figure 5.5. Graphic of magnitude of *GradT (K/m)* in function of anisotropy ratio showing comparisons between skull and CSF layers; VC 800 mA input at t = 8 s.

Figure 5.6 shows the descriptive statistics of *GradT* directional at ROI skull for isotropic and anisotropic models, for each electrode configuration, at t = 8 s with VC. While Figure 5.7 shows the maximum value of the previous data, a comparison between Wang and VC is made. As seen, Wang and VC have similar behaviours in all cases. However, VC exhibits bigger values than Wang. The isotropic case is the one with the highest temperature gradient, and the magnitude value decreases provided the anisotropic ratios increase. This occurred in all cases, with the exception of RUL *GradTz*, which has an opposite demeanour - isotropic had the lowest value and the 1:100 had the highest. Also, the maximum magnitude occurs in the latter example.

For *GradTx* (Figure 5.7a) and *GradTz* (Figure 5.7c), RUL has the biggest values, followed by BL and, lastly, BF montage. However, *GradTy* (Figure 5.7b) behaves differently. BF montage has the highest magnitude increase while BL and RUL have similar values.

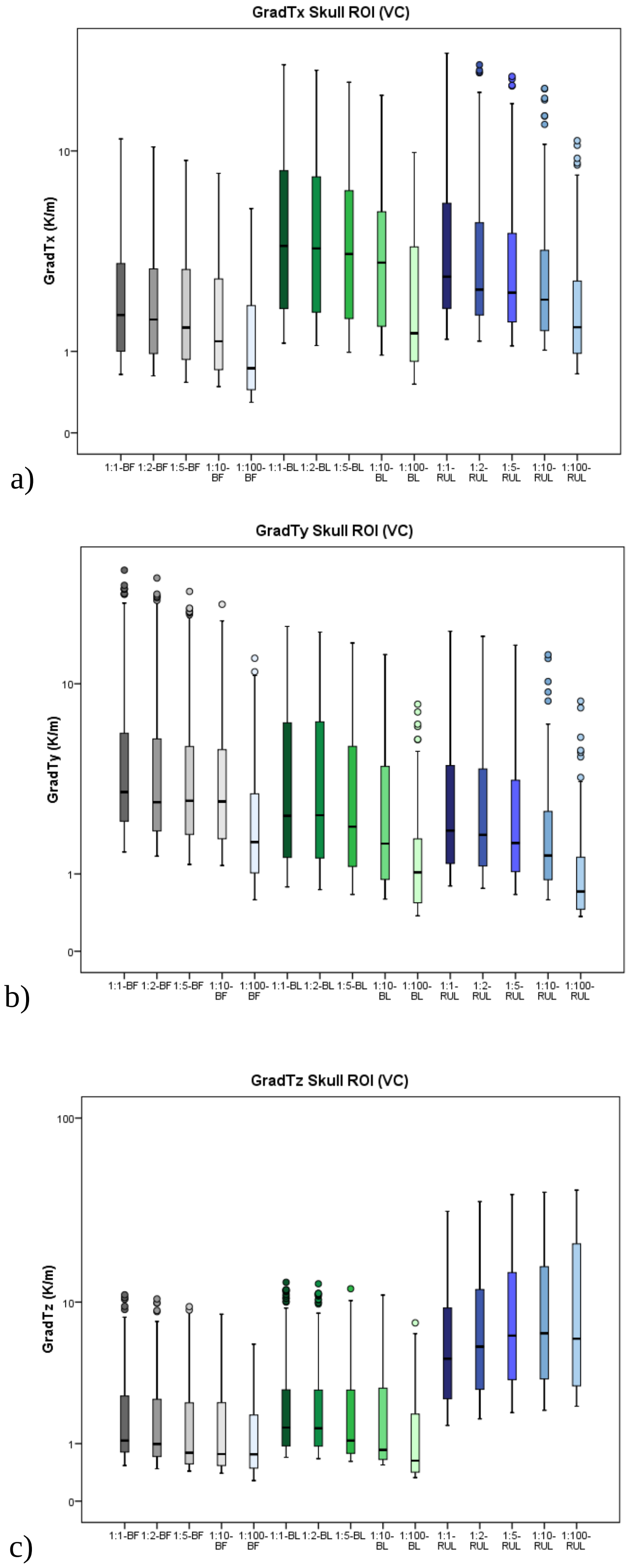

Figure 5.6. Descriptive statistics of GradT directional (a) GradTx, (b) GradTy and (c) GradTz, at ROI skull. BF (grey), BL (green) and RUL (blue); isotropic to anisotropic goes from darker to lighter colour tone. VC 800 mA input at t = 8 s.

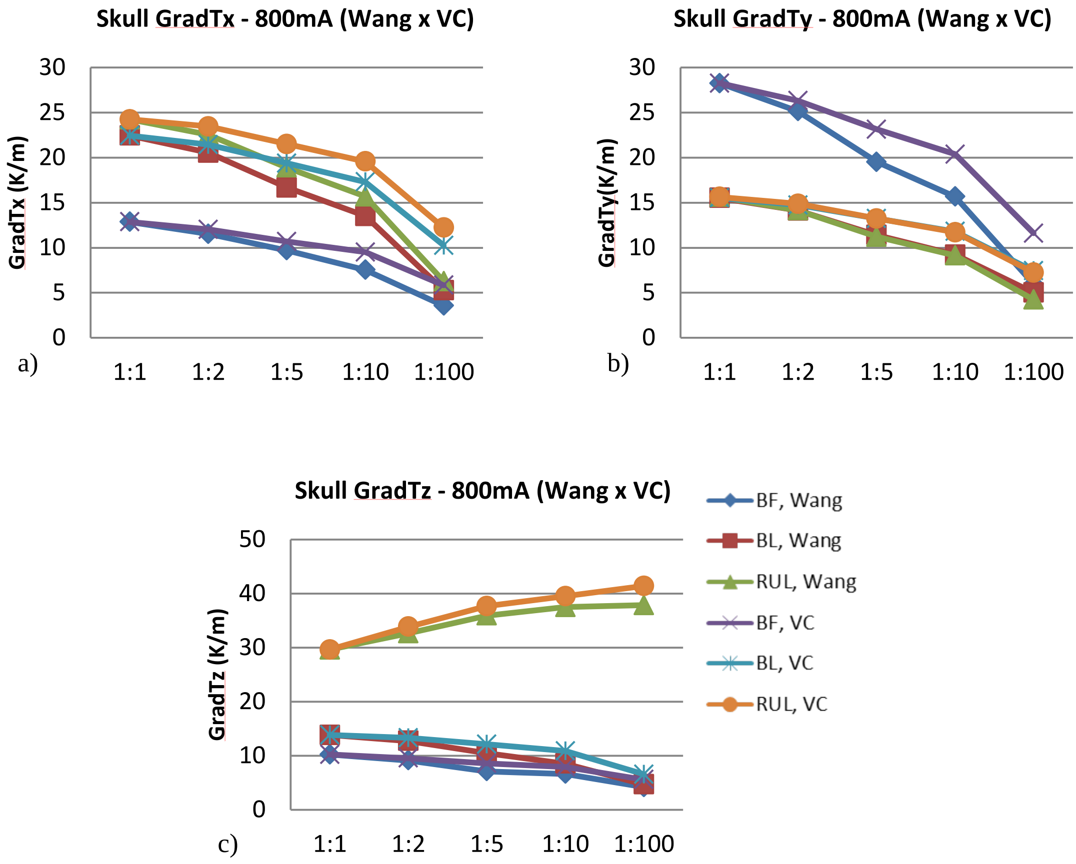

Figure 5.7. Graphic showing the behaviour of GradT directional maximum (K/m) in function of anisotropic ratio. Comparison between Wang and VC is made. Input of 800 mA at t = 8 s. (a) GradTx, (b) GradTy and (c) GradTz.

In order to illustrate the behaviour of *T* and *GradT*, coloured figure maps are plotted (Figure 5.8), in the BF case with VC. The images show all tissue layers in the region close to the electrodes. The hot spots (in red) occur on the scalp in regions close to the electrode. Internal tissues have no increase in temperature (blue regions). The contour map shows the magnitude of *GradT*. In general, the *GradT* decreases as long as the anisotropy ratio is increased. The E-field is represented by white arrows. No difference can be observed.

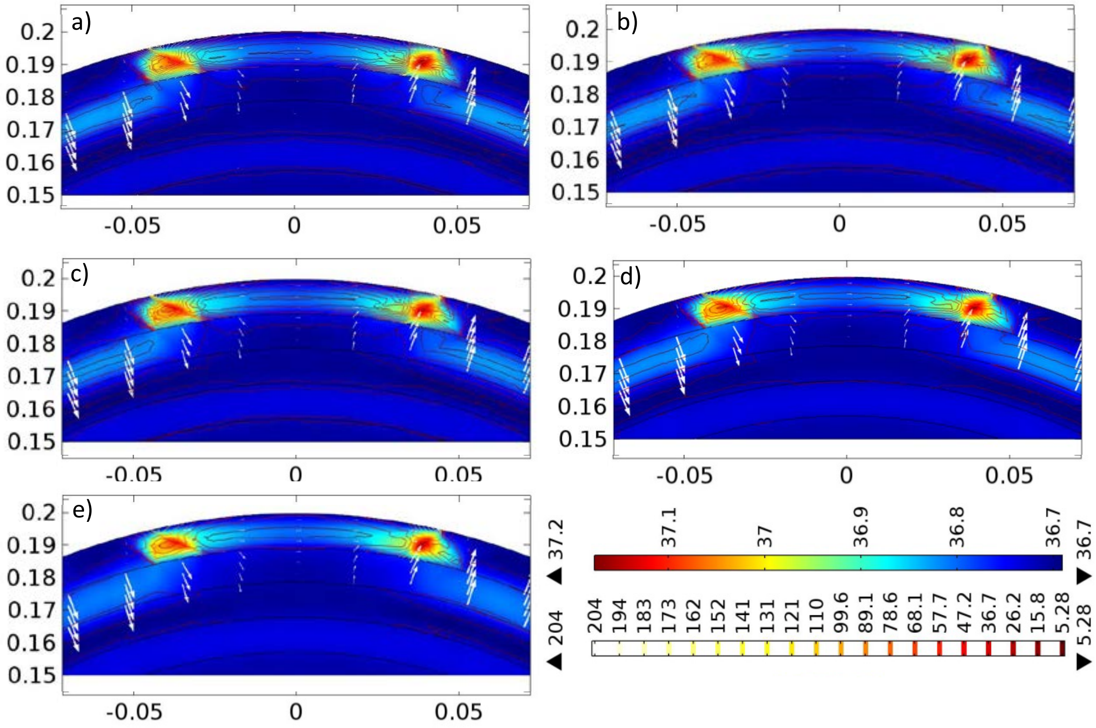

Figure 5.8. Comparison of the isotropic and anisotropic model simulations in the ROI for BF (VC, 800 mA input). The false color map shows T_{max} (°C) behaviour, the contour plot shows the GradT (K/m) and the white arrows the E-field for the cases (a) 1:1 (isotropic); and anisotropic for rations (b) 1:2, (c) 1:5, (d) 1:10 and (e) 1:100.

The REs of the magnitude of *GradT* for all ROI and for each layer of ROI are shown in Figure 5.9, for each electrode configuration and all four analysed ratios at t = 8 s, when Wang is applied. Although no relevant difference is found when calculating the descriptive statistics, it is important to note that the RE among the skull anisotropy cases, the *GradT* is affected in each layer of the model. As represented in this figure, in each case the shape is similar, where the smallest ratio (1:2) has the lowest error and, provided the σ_T/σ_R ratio is increased, RE has larger values. Also, RUL configuration is the one least prone to error, whereas BF has the highest increase of all. The exception to this rule occurs at ratios 1:5, 1:10 and 1:100 for the entire ROI, where BL has the biggest rise.

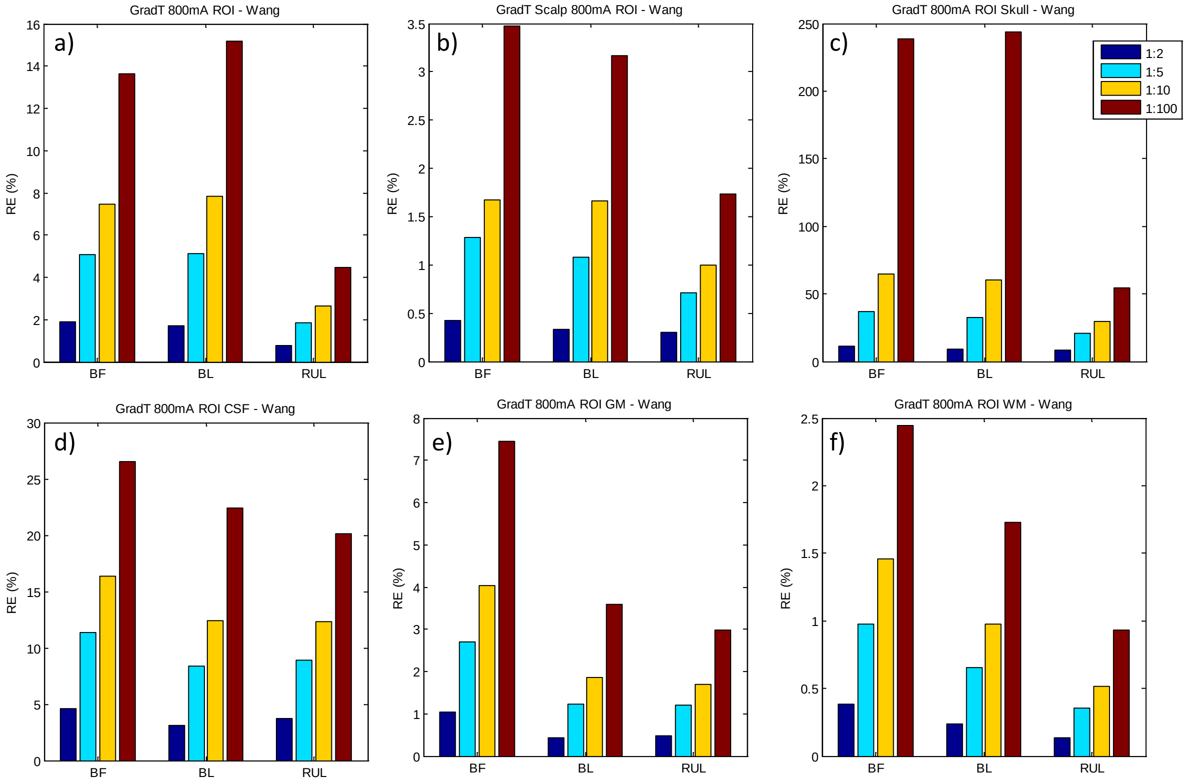

Figure 5.9. Relative error of gradient of temperature magnitude for the entire ROI (a) and each layer of the model (b) scalp, (c) skull, (d) CSF, (e) GM and (f) WM for each electrode configuration and all the anisotropic ratios (1:2, 1:5, 1:10, 1:100). Shown here for Wang constraint, 800 mA.

The skull is the most affected layer, where RE varies from 8.4 to 243.9 %. After the skull, CSF is the second layer with the most relative error when anisotropy is considered. CSF RE reaches a range from 3 to 26.3 %. This range is even bigger than the relative error from the entire ROI, which has percentage ranges of 0.8 to 15.2 %. The GM layer has a range of 0.4 to 7.4 %; scalp 0.3 to 3.5 %; and finally, WM 0.1 to 2.4 %.

GradT directionality (*GradTx*, *GraTy*, *GradTz*) behaviour is also analysed, as shown in Figure 5.10. As long as the σ_T/σ_R ratio increases, RE rises. Analysing from the perspective of the electrode montages, for Wang' contraint, the BL and RUL has the biggest RE along the x direction, and the BF has the maximum RE along the y direction. It appears that when the value of thermal conductivity increases (x and y are the tangential and bigger values) the RE (compared to the reference, isotropic) rises.

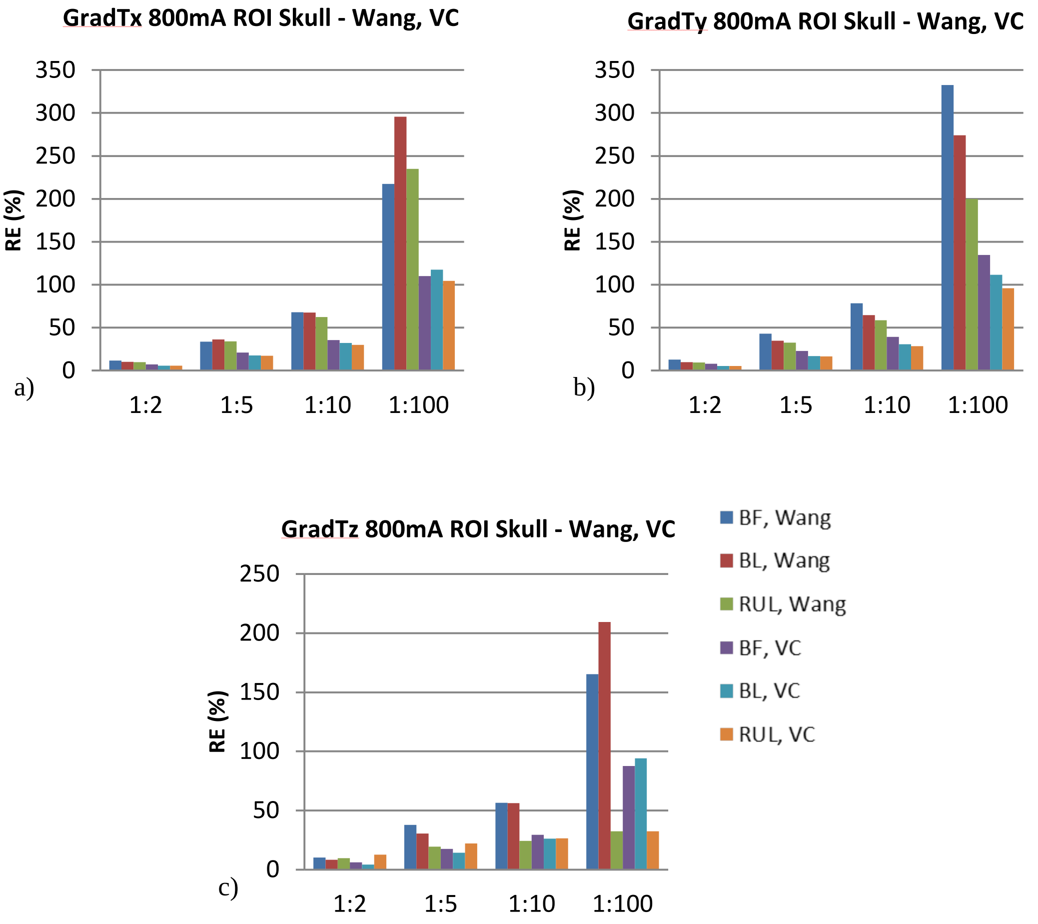

Figure 5.10. Comparison between relative error of maximum gradient of temperature from skull, for Wang and Volume constraint, 800mA input, t = 8 s. (a) *GradTx*; (b) *GradTy*; and (c) *GradTz*.

For VC, the BF and BL have the highest RE for *GradTy* and *GradTx*, respectively; while RUL has the biggest RE at *GradTz* for the smallest anisotropic ratio (1:2 and 1:5) and at *GradTx* for 1:10 and 1:100. Analysing RE over the perspective of the anisotropic ratios, the BF electrode montage at the y direction has the highest RE, for all ratios, for both Wang's constraint and VC; except for the smallest ratio from VC that is the RUL configuration along the z direction.

Comparing RE with both constraints, in general, Wang’s constraint is the one with the biggest RE in all cases. When analysing each *GradT* directionality and each anisotropic ratio, along the x direction the BF (Wang) has the biggest RE for 1:2 and 1:10 and the BL (Wang) for 1:5 and 1:100; the BF (Wang) shows the highest value at y direction and also the largest most significant from all simulations. Finally, along z direction BF (Wang) for 1:5 and 1:10, BL (Wang) for 1:100 also have the highest RE; and the smallest ratio is the RUL (VC).

5.4. Comparisons and Discussions

In this study, the aim is to analyse the behaviour of temperature distribution in the different tissues when anisotropy thermal conductivity is considered in the skull. A five layer spherical head model is used. Also, a ROI situated nearby the electrodes, where the heat transfer is more prominent, is considered (Figure 5.1). The variations according to the electrode montage used and the thermal anisotropic values considered are observed.

The BF and BL seem to have the same type of behaviour where the T_{max} occurs in the isotropic case, and the value decreases as long as the anisotropic ratio increases. The RUL has an opposite demeanour. Therefore, it is possible to affirm that the T_{max} values are influenced by the values of the tensor eigenvalues. These results reinforce the findings of Berjano, Saiz and Ferrero (2002), with regard to the study of the cornea. They claimed that there was a direct relation between T_{max} and the temperature profile dimensions. In their study, they considered an ellipsoidal shape with width/depth ratio of 1.3. From their results, it is possible to hypothesise that the thermal conductivity is inversely proportional to the temperature, when analysed at the same point and time. Studying radiofrequency ablation (RFA), Watanabe et al. (2010) found similar results.

In addition, in the present study the electrode montage also played an important role. As demonstrated in Figure 5.2, the BF and BL behaved totally different to RUL.

Studies (Bai et al. 2012; Bai, Loo & Dokos 2011; Lee et al. 2011; Utz et al. 2010) of E-field also show an influence according to the electrode montage used. The current flow and current density also suffered variations.

The results here showed that the *GradT* magnitude demonstrated different and opposite behaviour for skull and CSF when the anisotropic ratio is increased. With the parameters simulated, k_{skull} is 1.91 times bigger than k_{CSF}. It seems that the value of the thermal conductivity is also important in making changes in *GradT*.

It also found a variation in the directionality of *GradT* due to skull thermal anisotropy. These results are also dependent on the electrode montage. For the BF and BL configurations, the smaller values are for *GradTz*; whereas for RUL, a smoother decline happens vertically (Figure 5.6). These findings agree with other studies related to the cornea. As stated by Berjano, Saiz and Ferrero (2002) and Trembly and Keates (1991), the anisotropic thermal conductivity of the cornea influenced the temperature distribution. They suggested that conductivity was larger in the longitudinal direction (parallel to the corneal surface) than in the transverse direction. To support this, in the study of Karampatzakis and Samaras (2010), they stated that the introduction of a tangential component of thermal conductivity larger than the transverse component leads to a smoother temperature variation along the vertical axis. It is known that the skull electrical anisotropy smears out and weakens the electric field (Wolters et al. 2006).

Barton and Trembly (2013) state that the anisotropy of the thermal conductivity of the cornea must be known, in order to quantify the balance of heat transfer toward the epithelial and endothelial layers and parallel to them. It is also known that the temperature distribution is influenced by the anisotropy conductivity on the cornea, considering anisotropy on the skull is also going to influence the temperature variation, as our models show. Moreover, the CSF is also going to be affected by the anisotropy (Figure 5.4b). However, this variation is negligible.

Comparing the two anisotropic methods analysed, *GradT* directionality is larger in the VC cases, although the value of its thermal conductivity is smaller when compared with Wang's constraint. Consequently, Wang's constraint has a bigger RE. Therefore, it is possible to affirm that the maximum temperature gradient is inversely proportional to thermal conductivity.

It is interesting to note that, when comparing the maximum value of directional *GradT* for both constraints, each electrode configuration behaves in a specific manner. The BL has higher values in the horizontal direction; whereas the BF has higher values in the vertical direction; and the RUL is the one with the largest *GradTz* rise. This reinforces the influence of electrode configuration into T and *GradT* behaviour. As specified by Lee et al. (2012), different electrode configurations generate an E-field that might generate fluctuations in diverse regions of the head. Making an analogy between the electrical and thermal fields, *GradT* directionality is changed according to the electrode montage used. In the present study, the RUL has the strongest *GradT* magnitude.

In the case of RFA, most theoretical models have used a constant value for *k*, probably due to the fact that changes in *k* with temperature are not so marked as in σ (Trujillo & Berjano 2013). A rise in *k* similarly involves a decrease in the maximum temperature reached at the end of a pre-set time (Berjano, Saiz & Ferrero 2002). This statement agrees with our study for the BF and BL electrode configurations. However, for the RUL electrode configuration, an increase at T_{max} happens while increasing *k* value. It is possible to state that the position of the electrode configuration influences how the electric field would spread out along the tissues, and consequently, the temperature gradient.

5.5. Conclusions

In this chapter, the SHM_05 model is used to numerically investigate and analyse the profile of temperature and *GradT*, when thermal anisotropy conductivity is considered in the skull layer. From the three electrode montages and the anisotropic relation used, the behaviour of T_{max} varies for RUL, when compared to the BF and BL. The.

GradT varies in the skull and CSF layers, with opposite demeanours. The skull directionality of *GradT* changes according to electrode configurations and, in general, decreases while the σ_T/σ_R increases. From the constraint applied to conductivity used, the VC has higher T and *GradT* increases when compared to Wang.

There is room for improvement with this study. Firstly, the geometry considered was a simplified spherical head model. More accurate and realistic results can be found if a realistic head model is used and if it is possible to consider microstructure information. Apart from that, the study considered a constant value for electrical conductivity. As mentioned by Trujillo and Berjano (2013), the electrical conductivity cannot be constant with temperature, otherwise it is impossible to achieve realistic results. Berjano, Saiz and Ferrero (2002) also established that it is necessary to include the effect of temperature when simulating with the intention of obtaining more realistic temperature profiles in the model, however, these studies are related to RFA. So far, there is a still lack of information and uncertainties about k and the interaction between k and σ. More studies are still necessary to provide more accurate information.

6. HEAT TRANSFER DUE TO ELECTROCONVULSIVE THERAPY: INFLUENCE OF ANISOTROPIC THERMAL AND ELECTRICAL SKULL CONDUCTIVITY AND EFFECT OF BIOLOGICAL PROPERTIES

6.1. Introduction

This chapter is to develop a more realistic head model, to apply anisotropic thermal and electrical conductivities within the skull layer, to examine their influences and to analyze the effect of heat transfer on the brain region due to ECT. The problems are defined for both isotropic and anisotropic versions of a realistic (RHM) and a spherical (SHM) head model using the finite element method, the solutions are computed using the COMSOL package and the results are evaluated by showing the temperature (T) behaviour within the tissues. For the realistic models, how the magnitude and spatial distribution of temperature are affected by biological properties and ECT stimulation parameters is examined.

6.2. Methods

6.2.1. Model Details

A spherical head model (Figure 6.1a-c) with six layers is built using the COMSOL Multiphysics 5.1 (COMSOL Inc.) package. The layers are: scalp; fat; skull; CSF; GM and WM. The model considered is the SHM_06, as described in Section 3.1.

The geometry was discretized and the FEM mesh was generated using the COMSOL package. A convergence analysis was also performed to choose the size of the mesh. The adopted mesh consisted of 93,171 tetrahedral elements.

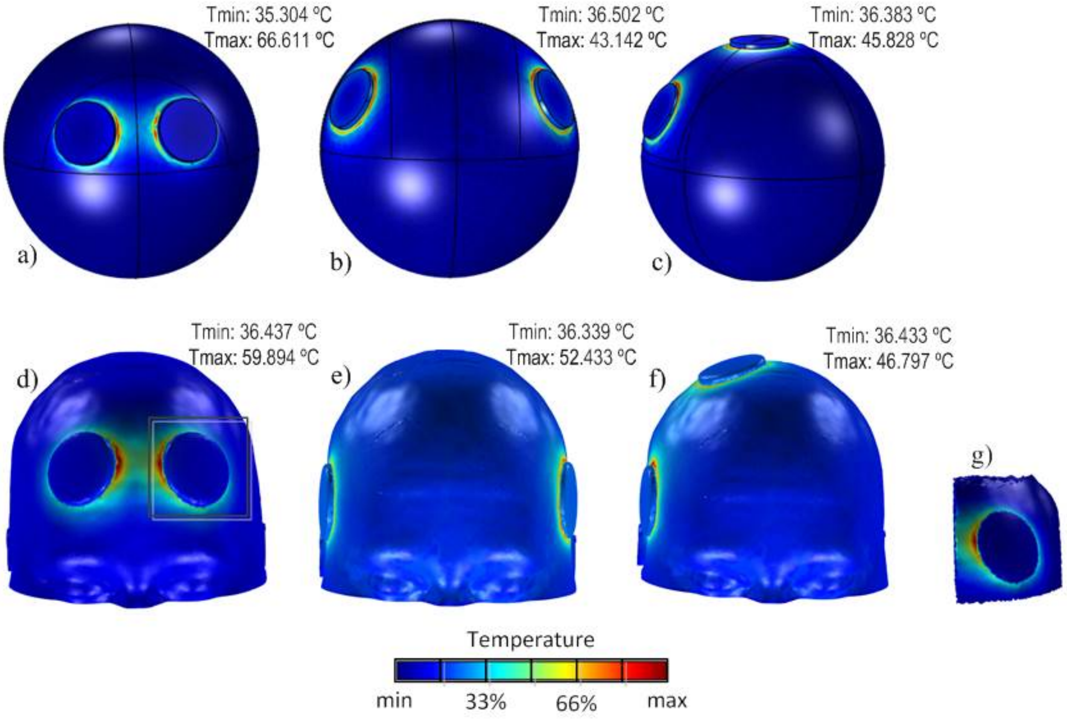

Figure 6.1. Models showing the electrode montage (a) BF, (b) BL and (c) RUL SHM; and (d) BF, (e) BL and (f) RUL RHM. The black box in image (d) represents the (g) ROI. The colour map represents temperature.

The baseline of the RHM used in this study (Figure 6.1d-f) was from a previous model from our research group (Shahid, Wen & Ahfock 2012; Shahid 2013; Song et al. 2016). The volume conductor was generated from MRI images acquired from BrainWeb (McConnell Brain Imaging Center). More details about the model was previously explained in Section 3.2. The model used (RHM_06) here is composed of six types of tissue: scalp; fat; skull; CSF; GM and WM. The volumetric mesh is comprised of about 2 million tetrahedral elements. Finally, it is imported to COMSOL Inc., where the physics and boundary conditions are assigned and defined. Each computation took approximately 17 minutes to run in a 32 GB ram, 4-core laptop workstation.

6.2.2. Volume Conductor Model

The BHTE combined with the Laplace equation, as described in Section 2.4 and rewritten here for better understanding (Equation 4), are used as the physics and as equations to solve the current models. The electrical and the thermophysical properties (Datta, Elwassif & Bikson 2009; Fiala, Lomas & Stohrer 1999; Hasgall PA 2014) for the scalp, skull, CSF, GM and WM are shown in Table 4.1. These properties are shown again here in Table 6.1 with the addition of fat properties.

Table 6.1. Thermophysical and electrical properties of fat.

	k *(W/(m.K))*	***σ*** *(S/m)*	***ρ*** *(Kg/m^3)*	***c_p*** *J/(Kg.K)*	***Q_m*** *(W/m^3)*	***ω_b*** *(1/s)*
Scalp	0.39	0.465	1125	3150	363	0.00143
Fat	0.21	$4.06e^{-2}$	911	2348	464.61	7.7436e-6
Skull	see Table 6.2	see Table 6.2	1850	1300	70	1.43e-4
CSF	0.60	1.654	1000	4200	0	0
GM	0.565	0.33	1035.5	3680	16229	1.3289e-2
WM	0.503	0.65	1027.4	3600	4517.9	3.6956e-3

$$\rho c \frac{\partial T}{\partial t} = \nabla(k\nabla T) + \omega\rho_b c_b\left(T_a\text{-}T\right) + Q_m + \nabla|\sigma\nabla V| \,. \qquad (4)$$

Initial and boundary conditions are assigned for the thermal and electrical physics. For the thermal physics, convection occurs in the external boundaries. It is defined by Equation 7, described previously in Section 2.4.1 and shown again here for better visualization.

$$\text{-}k \cdot \frac{\partial T}{\partial n} = h \cdot \left(T_{amb}\text{-}T\right). \qquad (7)$$

where h is 4 W/m^2.ºC and T_{amb} is 24 ºC. The interfaces between the layers are governed by conduction. Initial temperature is equal to 36.7 °C and the parameters for blood perfusion are assigned as ρ_b = *1050 Kg/m*^{3}, c_b = *3600 J/(Kg.ºC)* and T_a = *36.7 ºC* (Datta, Elwassif & Bikson 2009).

For the electrical physics, the external boundaries are considered electrically insulated and are represented by Neumann BC, $n \cdot (\sigma\nabla V) = 0$. Continuity of the normal component of the current density between regions of different conductivity occurs in the inner boundaries.

Moreover, the external surface of the anode is assigned Dirichlet (V = V_0 volts) BC, where V_0 is the input potential set as the rms value of a biphasic brief pulse of 111.11 Hz (models from Section 6.2.3) or 120 Hz (models from Section 6.2.4) and, 1 millisecond width pulse, and the amplitude is equivalent to 900 mA total current injection. This DC signal has been considered because otherwise the computations expend more than 18 hours to run a single case.

In comparison, the external surface of the cathode is assigned Dirichlet (V = 0 volts) BC. Dirichlet BC is chosen for the active electrode due to limitations of the software when thermal and electrical physics are applied together.

The three conventional electrode configurations (BF, BL and RUL) are modelled as described in Section 3.3.

6.2.3. Skull Conductivity Anisotropy

In this study, the skull is considered as anisotropic. The volume constraint, defined in Section 2.5.1, is used to set up the eigenvalues for the electrical and thermal anisotropic cases, Equation 11 ($\frac{4}{3}\pi\sigma_R(\sigma_T)^2 = \frac{4}{3}\pi\sigma_{iso}^3$) and Equation 18 ($\frac{4}{3}\pi k_R(k_T)^2 = \frac{4}{3}\pi k_{iso}^3$), respectively, as described in Sections 2.5.1 and 5.2.2.

The known common isotropic thermal and electrical conductivities, valued as $k = 0.53\ W/m.K$ and $\sigma = 0.0132\ S/m$ (Lee et al. 2009) are considered respectively. Four different anisotropic ratios (Wolters et al. 2006) are chosen and they are shown in Table 6.2.

Table 6.2. Values used to simulate the skull. Units of *k* and *σ* in *W/m.K* and *S/m*, respectively.

Ratio	**Skull Tensor eigenvalues**			
	Thermal		Electrical	
	k_R	k_T	σ_R	σ_T
1:1 (iso)	0.53	0.53	0.0132	0.0132
1:2	0.335	0.67	8.3e-3	1.6646e-2
1:5	0.181	0.905	4.5e-3	2.2607e-2
1:10	0.114	1.14	2.8438e-3	2.8438e-2
1:100	0.0245	2.45	6.1269e-4	6.1269e-2

6.2.4. Interface Electrode-Skin

For the isotropic case, the range of scalp electrical and thermal conductivities is varied, according to Table 6.3. All other thermophysical values are considered as in Table 6.1.

Firstly, neither the blood perfusion nor metabolic activity are considered. Therefore, in the first iteration, ω_b and Q_b are zero for all tissue layers. Afterwards, a study of how the convection of blood regulates the temperature was performed. In this case, ω_b scalp varied from 0 to 0.00143. Furthermore, the effect of fat is analyzed. The fat thickness in this model is 3.75 mm. For this purpose, a model without a fat layer is constructed. With the intention of retaining the same mesh and properties of the model, the fat layer is assigned scalp properties.

Table 6.3. Thermophysical and electrical properties of the scalp for interface electrode-skin study.

	k	**σ**	**Qm**	**ω_b**
	(W/(m.K))	**(S/m)**	**(W/ m^3)**	**(1/s)**
Scalp	0.33 - 0.45	0.255 - 0.465	0 - 363	0 - 1.43e-3

6.2.5. Measures for Analysis

Firstly, T_{max} against time is calculated. Afterwards, a case of ‘no-stimulation’ (no electrical input current) is conducted and compared with the case of input current using the graphical distribution of temperature profiles. Furthermore, a ROI (Figure 6.1g) is specified to evaluate the temperature near the electrodes. The RE ($RE = \sqrt{\frac{\sum_{i=1}^{n}\left(\nabla T_i^{iso}-\nabla T_i^{aniso}\right)^2}{\sum_{i=1}^{n}\left(\nabla T_i^{aniso}\right)^2}}$, Equation 20) of T is also calculated.

6.3. Results analysis

6.3.1. Temperature Behaviour – Isotropic Case

At first, the behaviour of temperature against time is evaluated. T_{max} occurred on the scalp, near the electrode. The location of T_{max} and its behaviour against time are analyzed and compared for different electrode montages (Figure 6.2a). In all cases, temperature increased exponentially with time, having an essentially first order system behaviour, with the maximum temperature occurring at the end of the stimulation period, on the scalp.

After that, the T_{max} in each layer is considered. Table 6.4 shows the values of T_{max}, at t = 8 s, for the isotropic case, in each tissue layer, with three electrode configurations, at RHM and SHM. The external layers, scalp and fat, experienced a high temperature increase which varied from 5 ºC to 29 ºC. Skull and CSF experienced a variation in temperature from 1 ºC to 3.9 ºC. The inner layers, GM and WM, experienced a rise in temperature from 0.06 ºC to 0.34 ºC. These differences varied according to the electrode configuration or model type used. Figure 6.2. b and c, show for example, the behaviour of each tissue layer and comparison between BF-RHM and BF-SHM. The internal layers did not vary widely in temperature.

Table 6.4. T_{max}, at t=8s, in each tissue layer for isotropic case, RHM and SHM.

	iso					
	RHM			SHM		
	BF	BL	RUL	BF	BL	RUL
Scalp	59.894	52.433	46.797	66.611	43.142	45.828
Fat	50.756	49.442	44.388	54.070	41.852	42.881
Skull	38.839	40.683	38.608	38.541	39.174	38.711
CSF	38.073	39.382	37.912	37.738	38.111	37.896
GM	36.809	37.049	36.880	36.764	36.784	36.779
WM	36.761	36.801	36.766	36.764	36.784	36.779

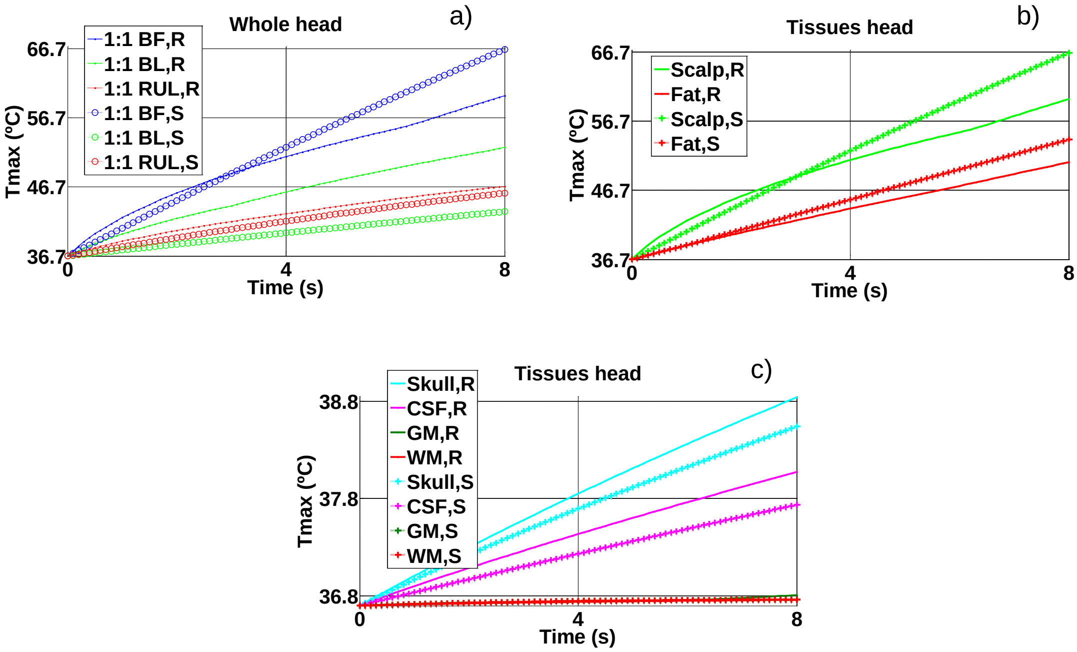

Figure 6.2. T_{max} (ºC) as a function of time for realistic (R) and spherical (S) models, isotropic cases (a) BF, BL and RUL for whole head; each tissue layer for BF electrode configuration (b) scalp and fat, (c) skull, CSF, GM, WM.

The temperature distribution in the radial direction is analyzed to study the behaviour of temperature through all tissues of the head and to see how temperature behaved in response to the electrical stimulation. This behaviour is investigated starting from T_{max}, which exhibits highest temperature and is therefore expected to have more influence on nearby regions. Figure 6.3a shows, as an example, the case for BF-RHM configuration. There is an increase in temperature in the external layers and, in deeper layers, the temperature decreased closer to the reference. In general, the radial distributions of RHM and SHM are similar shapes; any small variation is due to the simplicity of SHM. Figure 6.3b demonstrates the profile of the E-field for the same radial direction. A comparison of the three electrode configurations is made for the isotropic case. In the external layers, BF has a higher E-field, while in the internal layers it is the BL configuration.

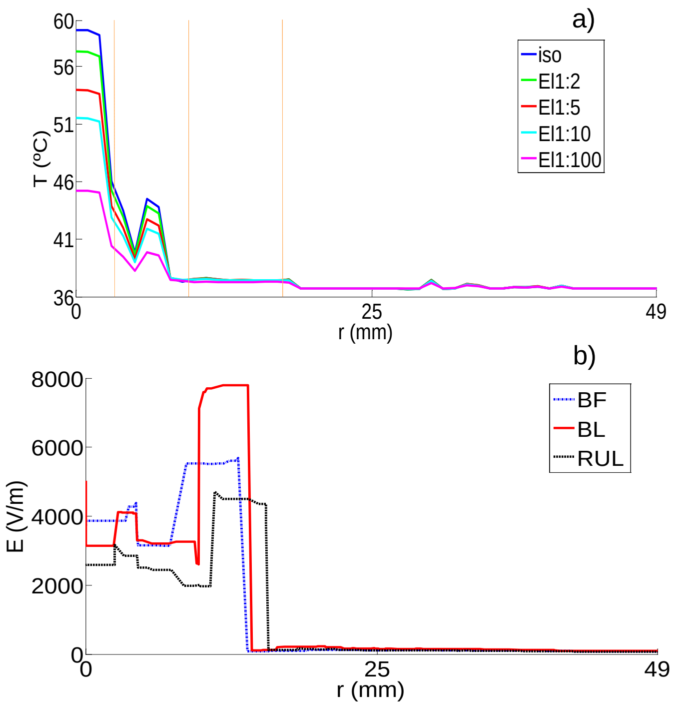

Figure 6.3. Distribution along a radial direction, RHM, t = 8 s: a) Temperature, isotropic and four electrical (El) anisotropy ratios, BF. The orange lines represents boundaries among tissues, 1st: scalp-fat, 2nd: fat-skull, 3rd: skull-CSF, boundaries among CSF, GM and WM are not shown; and b) E-field, isotropic, BF, BL, RUL.

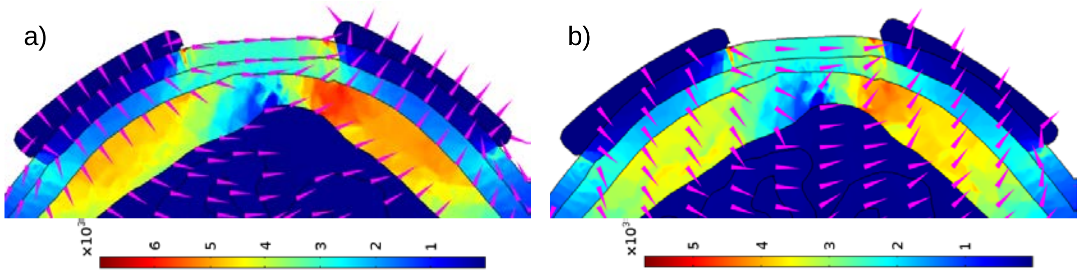

Figure 6.4. E-field distribution in a non-homogeneous medium along axial plane for BF-RHM. The magenta arrows represent current density. a) isotropic and b) El1:10.

6.3.2. Influence of Skull Anisotropy

6.3.2.1. Thermal Skull Anisotropy

The four anisotropic ratios (Table 6.2) are considered to analyze the dependence of temperature profiles on skull thermal anisotropy. For RHM, apart from the skull (Table 6.5), the CSF and GM were also slightly affected. BF configuration also showed a small difference in the fat layer. Increasing tangential to radial skull thermal conductivity, for BF configuration, the temperature decreased at fat, skull and CSF, while it rose at GM. For BL placement, the skull temperature dropped, while the CSF and GM temperature increased. For RUL, at a ratio of 1:2, skull temperature rose and as long as the ratio increased, the temperature started to drop again. In the CSF, temperature dropped for small ratios and rose at a ratio of 1:100. In GM, the temperature increased. Temperature varied up to 0.016 ºC in the fat, 0.575 ºC in the skull, 0.088 ºC in the CSF and 0.037 ºC in the GM, when compared to the isotropic case. BL placement experienced higher variation in comparison to BF and RUL.

For the SHM, increasing tangential to radial skull thermal conductivity, temperature varied only in the skull and in CSF layers. In the case of BF and BL, skull temperature decreased, while the CSF temperature rose. The fat layer at BF also decreased in temperature. However, for the RUL case, skull temperature increased at a ratio of 1:2 and, as long as the ratio increased, temperature decreased. In CSF, the opposite behaviour occurred; a slight drop followed by an increase in temperature. In the scalp, significant variation occurred at a ratio of 1:100 only.

The difference between the RHM and SHM may be due to a difference in geometry. When compared with ‘no-stimulation’, the temperature in GM increased by up to 0.35 ºC.

6.3.2.2. Electrical Skull Anisotropy

When considering electrical anisotropy in the skull (Table 6.5), all layers of the head model were affected. In the RHM, increasing σ_T/σ_R, for the BF and BL cases, the temperature dropped for all layers; except at GM and WM (BF) in which it rose. For the RUL case, in the scalp and fat layers, the temperature began increasing and, from a ratio of 1:10, it fell. In the skull, CSF and WM, temperatures rose, while in the GM, a fall was experienced. When compared with 'no-stimulation', the temperature in the GM increased by up to 0.25 ºC.

Figure 6.3a shows the temperature distribution over the distance for different electrical anisotropy, for the BF-RHM. It shows temperature decreasing as the electrical anisotropy ratio increases, in the external layers.

Table 6.5. T_{max} in the skull layer for isotropic (iso) and skull anisotropic conductivity cases of RHM (thermal (Th), electrical (El) and electrical and thermal (ElTh)).

	Skull								
	BF			BL			RUL		
	Th	El	ElTh	Th	El	ElTh	Th	El	ElTh
iso		38.839			40.683			38.608	
1:2	38.805	38.873	38.843	40.628	40.312	40.243	38.625	38.747	38.760
1:5	38.736	38.774	38.696	40.518	39.841	39.693	38.624	38.800	38.796
1:10	38.671	38.636	38.528	40.406	39.514	39.311	38.609	38.792	38.789
1:100	38.445	38.280	38.142	40.108	38.734	38.444	38.508	38.932	38.840

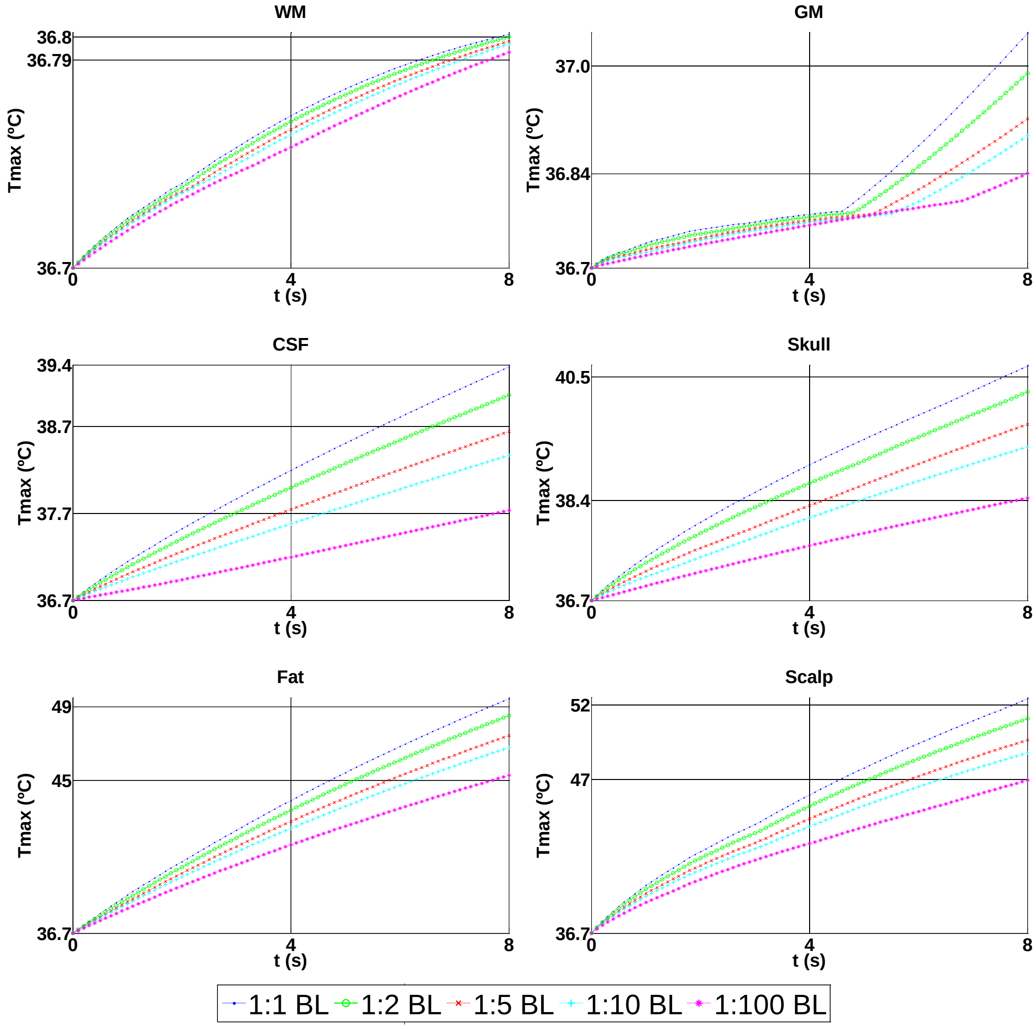

Figure 6.5. Comparison of T_{max} for four different setups (RHM), BL electrode configuration. isotropic (1:1) versus 4 anisotropy ratios (1:2, 1:5, 1:10, 1:100), when considering thermal and electrical conductivity in the skull layer.

The profile of the E-field and the path of current density are shown in Figure 6.4. A comparison is made between the isotropic case and electrical anisotropy for a ratio of 1:10. The E-field intensity is higher and the current density is stronger for isotropic cases, when compared to electrical anisotropy. That occurred for BF and BL configurations, while the opposite behaviour was evident for RUL, corroborating with temperature results, as shown in Table 6.5.

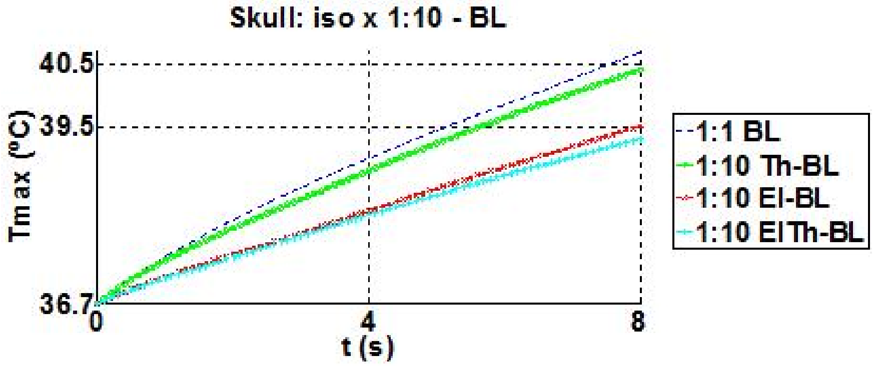

Figure 6.6. Comparison of T_{max} for isotropic versus anisotropic, BL montage – thermal (Th), electrical (El) and thermal-electrical (ElTh), at ratio 1:10, in the skull layer.

6.3.2.3. Electrical and Thermal Skull Anisotropy

While the electrical and thermal anisotropy conductivity of the skull were applied together, the results were similar to those when electrical anisotropy was considered alone. However, for the skull layer, temperature decreased slightly more. Table 6.5 shows the values of T_{max} for the skull, a comparison among isotropic and anisotropic conductivities. This layer is the one which presented greater variation in temperature according to the conductivity applied and electrode configuration used.

Graphs of the behaviour of T_{max} versus time for isotropic, four ratios of electrical and thermal skull anisotropy shows in Figure 6.5, the BL-RHM is chosen as an example. A decrease in temperature can be seen while the ratio increases.

Figure 6.6 demonstrates a comparison among isotropic and three types of skull anisotropy applied. For the skull layer, a ratio of 1:10 is chosen as an example in the BL-RHM case. A higher temperature appears in the isotropic case (40.68 ºC). When considering anisotropy, temperature dropped. The decrease of 0.28 ºC, 1.17 ºC and 1.2 ºC respectively occurs in thermal, electrical and electrical and thermal skull conductivity.

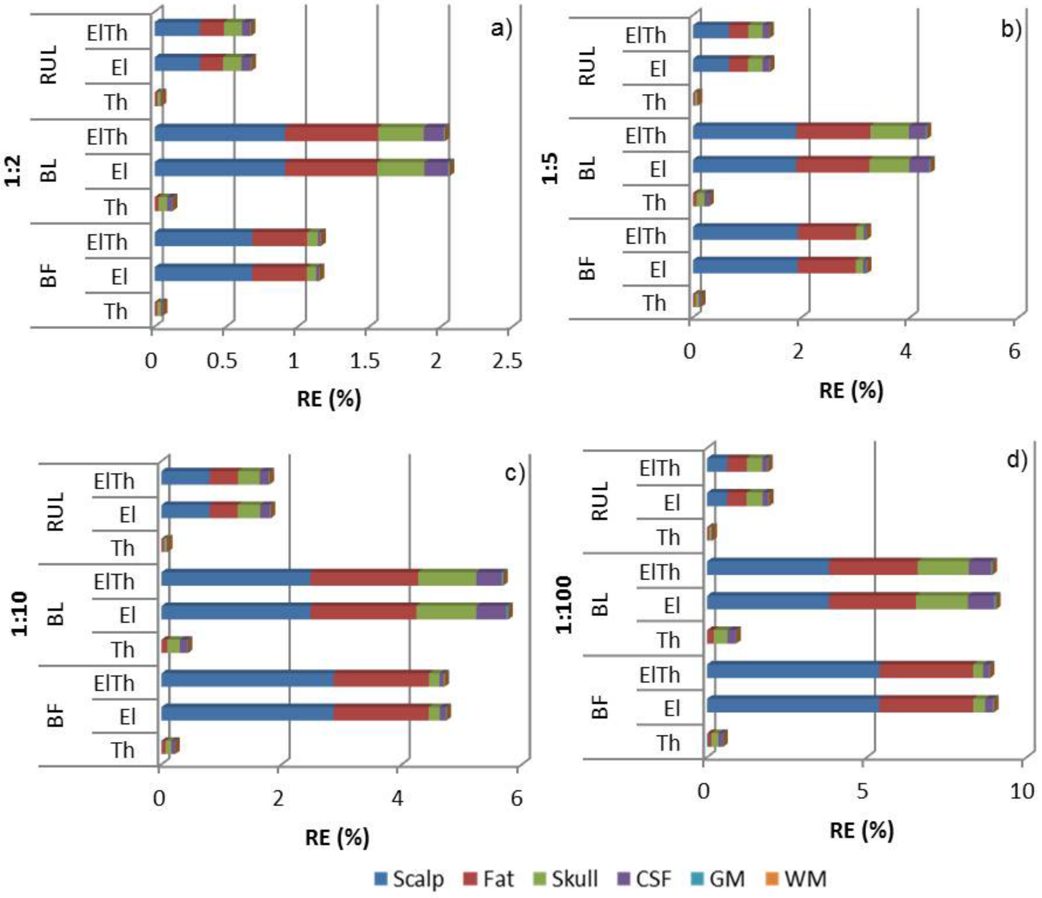

Figure 6.7. Temperature RE (%) of anisotropic (a) 1:2, (b) 1:5, (c) 1:10 and (d) 1:100 models from ROI; thermal (Th), electrical (El) and thermal+electrical (ElTh), for BF, BL and RUL on RHM. Each colour relates to one head tissue, scalp (dark blue), fat (red), skull (green), CSF (purple), GM (light blue) and WM (orange).

The RE (Equation 20) of temperature was calculated from the ROI (Figure 6.1g). Figure 6.7 shows the comparison of RE for all RHM models. As the anisotropy ratio increased, the difference in temperature also increased. Thus, a ratio of 1:100 showed a higher variation in temperature, especially when electrical anisotropy was applied. For all anisotropy ratios, thermal anisotropy showed little deviation. Among layers, the external layers were the ones with a higher variation in temperature. The deeper into the internal tissues, the less difference in temperature occurred. When comparing the electrode configurations, BL placement was the one with a bigger variation in temperature.

6.3.3. Current Input Threshold

A range from 0.4 A to 3.6 A of input current was considered to find the thermally safe current threshold. This range included and went beyond normal ECT limits. The behaviour of temperature while increasing the current for RUL-RHM, at 8 s, can be found in Figure 6.8. Figure 6.9 shows temperature distribution profiles. When the input current increased, temperature rose. The external layers are affected the most. Scalp and fat reach 40 ºC when the current is 0.52 A and 0.58 A, respectively; and 41 ºC, at 0.59 A and 0.74 A, respectively, at the end of 8 s, for RUL-RHM. Temperature at the GM reaches 38 ºC if current applied is 2.48 A (RUL-RHM) (Figure 6.9), 1.75 A (BL-RHM) and 3.33 A (BF-RHM) for 8 s.

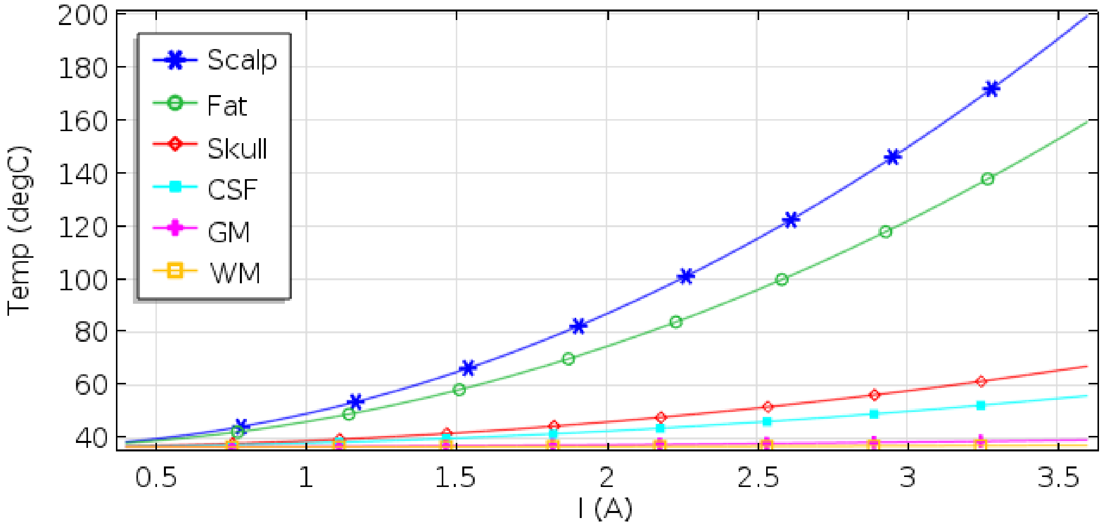

Figure 6.8. Behaviour of T_{max} (ºC), in each tissue layer, for different current (A) input, RUL-RHM, t = 8 s.

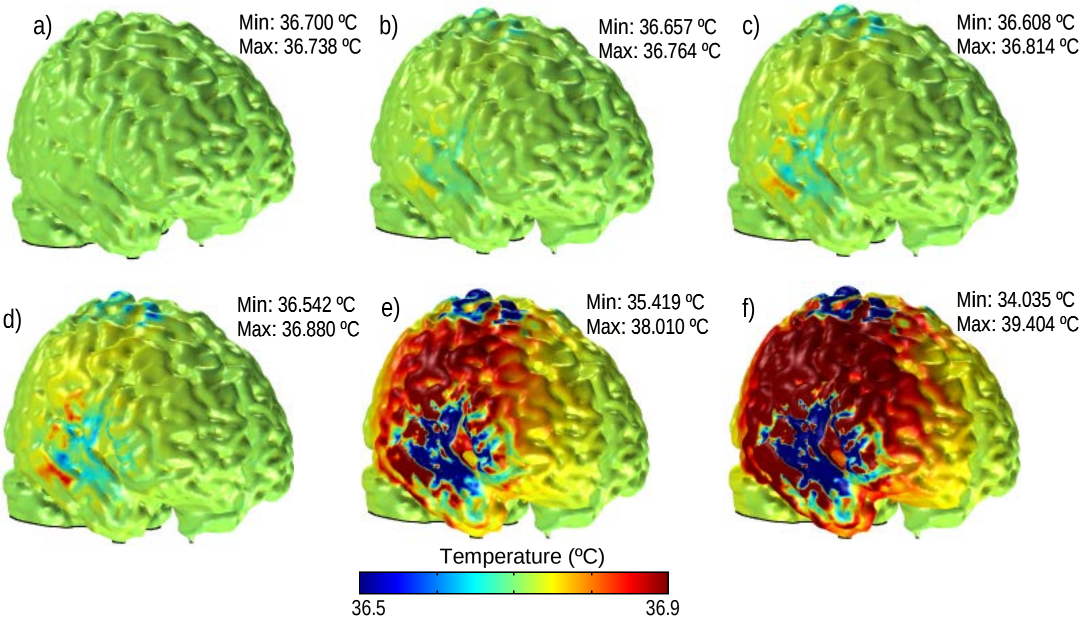

Figure 6.9. Surface temperature distribution of GM for RUL-RHM, at 8 s, for cases: (a) ‘no-stimulation’, (b) 0.5 A, (c) 0.7 A, (d) 0.9 A, (e) 2.5 A and (f) 3.6 A.

6.3.4. Effect of Biological Properties on Induced Temperature Variation

The models considered in this section are isotropic and the thermophysical and electrical parameters are related to Table 6.3. The effect of biological properties during the induced temperature variation is emphasized. Furthermore, analysed the influence of blood perfusion, metabolic heat and the fat layer are analysed.

6.3.4.1. Peak of Temperature and Temperature Distribution Induced by ECT without Blood Perfusion and Metabolic Heat

In the first iteration, the focus is on the temperature increase solely due to ECT-induced heat. In this case, the contributions of blood perfusion and metabolic heat are not accounted for, and for all tissues they are assigned as zero. Three types of electrode montage are modelled, BF, BL and RUL. Figure 6.10a and Table 6.6-I show changes in temperature field distribution and the maximum temperature as a function of scalp electrical conductivity ($\sigma = 0.255\text{-}0.605\ S/m$) with fixed thermal conductivity ($k = 0.39\ W/m.K$). Figure 6.10b and Table 6.6-II show variations in temperature field distribution and peak temperature as a function of scalp thermal conductivity ($k = 0.33\text{-}0.45\ W/m.K$) with electrical conductivity fixed ($\sigma = 0.39\ S/m$). The conductivity variation is considered in the scalp layer. As expected the external layer suffers the highest temperature rise due to ECT electrical stimulation. The peak varied 2.49 ºC for BF, 0.66 ºC for BL and 1.55 ºC for RUL, when thermal conductivity is considered constant (Table 6.6-I); and the peak temperature varied 2.12 ºC for BF, 1.27 ºC for BL and 0.71 ºC for RUL, when electrical conductivity is considered constant (Table 6.6-II). The results demonstrate that temperature increases when thermal and electrical conductivity decrease.

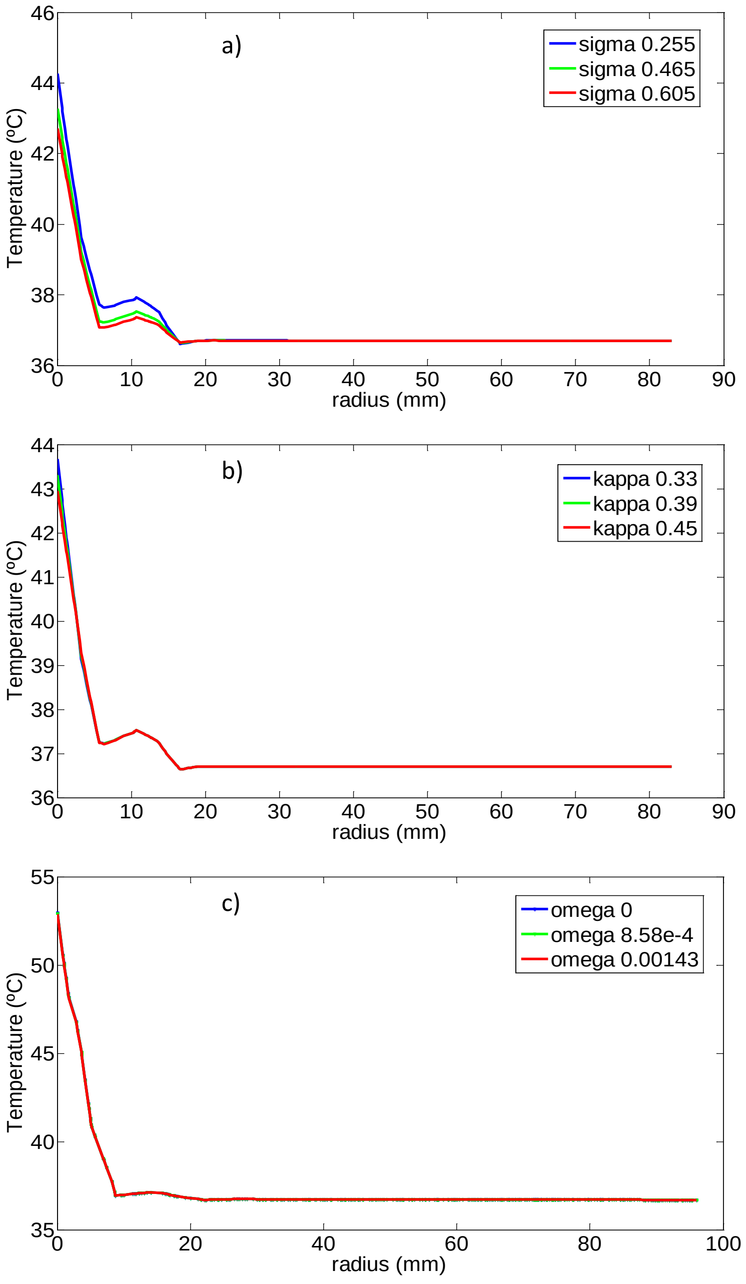

Figure 6.10. Temperature distribution along radius of model after ECT stimulation. The profile begins where peak temperature occurs. (a) Temperature versus scalp electrical conductivity (σ - sigma), for RUL electrode montage; the thermal conductivity (k - kappa) was fixed at 0.39 W/m.K and blood perfusion and metabolic heat are absent. (b) Temperature versus scalp thermal conductivity, for RUL electrode montage; the electrical conductivity was fixed at 0.465 S/m and blood perfusion and metabolic heat are absent. (c) Temperature versus blood perfusion, for BF electrode montage; the scalp electrical and thermal conductivity are fixed at 0.465 S/m and 0.39 W/m.K, respectively. Only slight variations cause graphs to superimpose.

Table 6.6. The effect of biological parameters on maximum temperature by ECT stimulation for BF, BL and RUL electrode configurations.

	σ	k	ω_b	T_{max} (ºC)		
	(S/m)	(W/m.K)	(1/s)	BF	BL	RUL
I	0.255	0.39	0	54.26	47.13	44.28
	0.465			52.96	46.87	43.28
	0.605			51.77	46.46	42.72
II	0.465	0.33	0	54.14	47.42	43.68
		0.39		52.96	46.87	43.28
		0.45		52.02	46.46	42.28
III	0.465	0.39	0	52.96	46.87	43.28
			$8.54e^{-4}$	52.92	46.83	43.26
			0.00143	52.89	46.81	43.25

Table 6.7. The influence of fat and blood perfusion on peak temperature induced by ECT stimulation for BF, BL and RUL electrode configuration.

Fat	Blood perfusion	T_{max} (ºC)		
		BF	BL	RUL
y	*y*	52.89	46.81	43.25
y	*n*	52.96	46.87	43.28
n	*y*	42.51	38.35	38.57
n	*n*	42.53	38.36	38.58

6.3.4.2. Peak Temperature and Temperature Distribution Induced by ECT with Blood Perfusion and Metabolic Heat

Blood perfusion and metabolic heat balance the temperature in the head. To show how the convection of blood plays its role, it is modelled for cases with fixed values for electrical ($\sigma = 0.465$ S/m) and thermal ($k = 0.39$ W/m.K) conductivity and varying values of blood perfusion on the scalp ($\omega = 0\text{-}0.00143$ 1/s). Metabolic heat is considered fixed at 363 W/m^3. The blood temperature is set as 36.7 ºC. In cases where blood perfusion and metabolic heat were not considered (Table 6.6-I and II), the temperature in the scalp increased to 52.96 ºC, 46.87 ºC and 43.28 ºC, for BF, BL and RUL configurations, respectively. When considering metabolic heat and blood perfusion equal to 0.00143 1/s, the peak temperature reached 52.89 ºC for BF, 46.81 ºC for BL and 43.25 ºC for RUL (Figure 6.10c and Table 6.6-III). This shows a drop in temperature of 0.07 ºC for BF, 0.06 ºC for BL and 0.03 ºC for RUL. All three electrode configurations had a slight drop in temperature.

6.3.4.3. Effect of Fat Layer on the Peak Temperature

A model without considering the fat layer was built to investigate the peak temperature, where the fat layer was assigned as scalp, with electrical conductivity of 0.465 S/m, thermal conductivity of 0.39 W/m.K, and considering blood perfusion and metabolic heat equal to 0.00143 1/s and 363 W/m^3, respectively, and without the influence of blood perfusion. Table 6.7 shows the results. When a fat layer is not included in the model, the peak temperature dropped substantially. The variation of temperature was 10.38 ºC for BF, 8.46 ºC for BL and 4.68 ºC for RUL configuration, when blood perfusion was considered. If blood perfusion is not taken into account, only a slight variation between 0.02 ºC to 0.06 ºC was evident.

6.4. Comparisons and Discussions

6.4.1. Behaviour of Temperature in Isotropic Model

During ECT practice, the electrical current applied is high, but only for a short period of time. Current propagates through the head, however the heat generated due to the electrical stimulation influences only specific regions near the electrode; mainly in the scalp and fat. Heat propagation depends on the material constitution and causes temperature change. The change rate depends on the value of thermal capacitance and the rate at which heat is dissipated. For the former, the bigger the thermal capacitance is, the less temperature increases. For the latter, scalp loses heat by two mechanisms, convection on the outer surface and blood perfusion in the inner parts. Figure 6.3 shows the behaviour of temperature along a radial line through the head. At first, the temperature increases with time due to the electrical stimulation, and reaches the

T_{max}, 59.894 ºC for BF, on the scalp, near the electrode. Starting from the scalp, temperature decreases, reaching 46.419 ºC at the scalp-fat boundary. It then has a bigger drop, of 9.054 ºC, in the fat layer. This effect is due to the scalp and fat being poor thermal and electrical conductors, especially fat. Fat has an electrical conductivity approximately 10 times smaller than the scalp and, practically, there is no blood perfusion working as a convection mechanism. In the skull layer, only an insignificant increase (of 0.17 ºC) is found. The current density in this layer is still increasing, but its magnitude is so small that it does not cause a rise in temperature. The blood helps to keep the temperature constant and close to T_{ref}. CSF together with GM and WM behave as a heat sink, keeping the temperature near to 36.7 ºC. In short, the main temperature rise associated with electrical stimulation, is near the electrode itself. This reflects the results found by Kim et al. (2007), where they simulated an implanted microelectrode array and saw a higher temperature near the device which decreased with distance from the electrode.

Electrode montage plays an important role (Table 6.5 and Figure 6.7). The T_{max} rise occurs when the electrodes are closer to each other, like in the BF. The RUL case, which has a unilateral configuration, has the smallest temperature increase. The electrode configuration and the distance between electrodes also influences the E-field, current flow and current density, as demonstrated in other studies (Bai et al. 2012; Lee et al. 2012).

6.4.2. Influence of Electrical and Thermal Skull Anisotropy

Considering electrical anisotropy, the BF case had a higher influence on the temperature increase in the external layers (scalp and fat) with a corresponding smaller effect in the internal layers. In the inner layers, the BL case experienced a greater impact. This happened because the increase in temperature is related to the magnitude and direction of the E-field (Figure 6.3b). The E-field flows from the active to the reference electrode. The BF placement, having the closest distance between electrodes, generates a strong E-field near them, in the external layers of the head. Because of this shunting of current within the scalp and fat layers, the E-field's intensity decreases in the internal layers, resulting in a small rise in temperature. In the BL configuration, the electrodes are further away from each other. Therefore, the E-field reaches deeper tissues causing a rise in temperature. For a voltage-controlled circuit, increasing WM σ makes Joule heat rise and, consequently, the temperature (Elwassif et al. 2006). In this study, when skull electrical anisotropy conductivity is considered, increasing σ ratio, decreases E-field (Figure 6.4) and hence the temperature. It is only in the skull and fat layers of the RUL that this rise occurs.

The results of T_{max} being influenced by the anisotropic ratio agree with other studies such as the findings of Berjano et al. (Berjano, Saiz & Ferrero 2002), on the study of the cornea. They reported a direct relationship between the temperature profile and the choice of anisotropic ratio. From their findings, it is possible to speculate that k at a specific time and position is inversely proportional to the temperature at that position. This also aligns with Watanabe et al. (2010) in their study of radiofrequency ablation.

The BHTE can be translated as a resistance-capacitance network. For a short time, as in the case considered in this study, the thermal capacitances works as a short circuit, allowing thermal charge. The capacitances play the major role because they are not totally charged, reducing the effect of thermal conductances. Therefore, thermal anisotropy is going to have a negligible effect on temperature behaviour. However, if the system reaches steady-state (hypothetical in ECT practice), the thermal capacitances work as an open circuit, and the resistances have a main role in the network. In this instance, it is important to consider thermal anisotropy, as the behaviour and distribution of temperature is going to be affected. This can be applicable in thermotherapy techniques such as thermal ablation and transcutaneous electrical nerve stimulation, or in implanted electronic devices (Kim et al. 2007) such as DBS (Elwassif et al. 2012).

6.4.3. Current Extrapolation

The input current used in ECT practice was extrapolated and the analyzed current range (0.4-3.6A) (Figure 6.8 and Figure 6.9) encompasses actual ECT current levels and beyond. The temperature in the internal layers increases more slowly than in the external layers. Damage and tissue ablation begin at 40 ºC and 41 ºC (Elwassif et al. 2006). These temperatures only occur in the external layers. Changes in cell excitability, network function and blood-brain barrier function occur (Elwassif et al. 2006) if the brain reaches 38 ºC. According to the simulations presented here, the input current needed to be higher than 1.75 A, for that to occur. These currents are not applicable to actual ECT practices and they are not a real case scenario but only for simulation. Therefore, from the simulations performed, within the input current range used during actual ECT practices, the scalp and fat are the only tissues where any damage can potentially occur, as stated by Swartz (1989). A sensitivity analysis which considered the variation of thermal and electrical conductivity values of the scalp, including or not including blood perfusion, metabolic heat and fat layer, was performed.

6.4.4. Temperature Distribution Considering the Effect of Biological Properties in a Realistic Model

The realistic head models in this study analysed the temperature distribution generated due to electrical stimulation, taking into account the effect of biological properties, thermal and electrical conductivity, blood perfusion and metabolic heat and the inclusion or not of a fat layer.

The results obtained partially agree with the findings of Elwassif et al. (2006), where they simulated deep brain stimulation in a cylinder representing WM. Their outcomes show that when increasing the value of σ while k is fixed, the peak temperature will increase. This difference may be due to the one-layer geometry considered in Elwassif et al. (2006), therefore, the influence of adjacent layers was not accounted for. In addition, in the present study where scalp temperature was analysed, the tissue parameters are different and suffer influence from the fat layer and convection to ambient.

BF was the electrode montage which showed highest peak temperature. It was also the configuration where the electrodes were closer to each other, making the E-field stronger. It is known that the electrode montage plays an important role in the behaviour and intensity of the E-field (Bai et al. 2012; Lee et al. 2012).

The brain temperature was unaffected when applying electrical stimulation. On the other hand, the scalp and fat layers had an effect of temperature rise that varied according to the electrode configuration used. Taking this into account, it demonstrates the importance of considering safety limits for each electrode montage (Datta, Elwassif & Bikson 2009).

The addition of metabolic heat and blood perfusion convected Joule heat out of the tissue layers, causing a drop in the peak temperature (Elwassif et al. 2006). In our results, that same behaviour occurs. However, the decrease in temperature is only up to 0.13 %, which equates to less than 2.5 times the drop in temperature found in Elwassif et al. (2006), despite the tissue layers observed exhibiting distinctly different properties.

It is known that current density in the scalp increases if fat is introduced into the model (Shahid, Wen & Ahfock 2011), causing a rise in temperature. The electrical conductivity of the scalp is approximately ten times greater than the electrical conductivity of fat. Current will flow through the least resistive path. This behaviour of the current in the presence of the fat layer can be due to shrinkage of the effective cross-sectional area of the preferential path of current in the scalp (Shahid, Wen & Ahfock 2011). Therefore, the inclusion of fat layer is an important factor to consider in a thermal-electrical human head model.

6.5. Conclusions

This work analyses the profiles of temperatures arising during electroconvulsive therapies when anisotropic thermal and electrical conductivities are considered in the skull layer. The work was conducted using both SHM and RHM, with six layers. The results from both head models show that current ECT practice is safe and no harm is caused to the brain from a thermal point of view. An increase in temperature occurs only in external layers, in specific regions, mainly near the electrodes, in the scalp and fat. The brain will only be affected if currents higher than 1.75 A are applied. The electrode montage influences temperature behaviour. Anisotropic thermal conductivity does not influence the results significantly; however, skull electrical anisotropy is an important aspect to consider. Moreover, the inclusion of blood perfusion leads to slight drop in peak temperature. Finally, the inclusion of fat is highly recommended in order to achieve more realistic results.

7. ECT ELECTRIC FIELD WHEN IN THE PRESENCE OF A BRAIN TUMOR

This chapter investigates the influence of an electric field generated through ECT stimulation in the presence of a tumor. Firstly, numerical head models are developed to include a brain tumor, then the ECT is applied and the electric field is evaluated. The inclusion and influence of WM anisotropy conductivity is also evaluated.

7.1. Introduction

There are more than 120 types of brain tumor which affect us. According to the World Health Organization (Louis et al. 2016), brain tumors can be classified into four different grades which vary in their aggressiveness. Grade I is the least severe, with potential for treatment and survival; while grade IV is the most malignant, with life expectation of only a few months.

A short clinical review by Kast et al. (2013) concluded that ECT can be used to better deliver chemotherapy in gliobastoma cases. They relate that if ECT stimulus is applied before chemotherapy then the blood brain barrier opens what could help the treatment.

Tumor treating field (TTField) (Miranda et al. 2014; Wenger et al. 2015; Wong, Lok & Swanson 2015) is an electrical stimulation technique that has been used for treating gliobastoma multiforme, a grade IV brain tumor. A clinical trial showed that TTField demonstrated similar efficacy to chemotherapy, with the advantage of no side effects (Wong, Lok & Swanson 2015). A numerical study of stimulating tDCS in the presence of a brain tumor (Song et al. 2016) showed that it is safe to apply this treatment when pain is present due to the oedema.

However, the stimulation of ECT on a patient with a brain tumor still presents many uncertainties. Therefore, in order to investigate the behaviour of ECT stimulation with a brain tumor, in this study a computational human head model is developed to include a tumor in the brain. Different model configurations are considered, such as varying grades of tumor (I to IV) and tumor location, influence of WM conductivity and electrode montages.

The aim is to understand the effect of electrical ECT stimulation in the presence of a brain tumor, whilst at the same time understanding how safe it is to administer. As far as we are aware, there is no numerical study which evaluates the use of ECT when considering a brain tumor, and the work in this chapter will try to fill this gap.

7.2. Methods

7.2.1. Modelling Details

The baseline of the realistic human head model was derived from previous studies from our research group (Shahid, Wen & Ahfock 2012; Shahid, Wen & Ahfock 2013; Song et al. 2016). The volume conductor was generated from MRI images from the subject MNI_0591, ICBM database (*ICBM: International Consortium for Brain Mapping* 2014). The model was segmented into 17 different tissues with the aid of the packages FSL and ScanIP. The tissues segmented included: scalp; fat; skull; CSF; GM; WM; eyes (sclera, lens, muscles); muscles of mastication; thalamus; brainstem; hippocampus; amygdala; putamen; pallidum and caudate. The model used here is the RHM_17, and more details are described in Section 3.2.4.

The brain tumor information was acquired from a patient (case 6) with low grade glioma, from the dataset of Surgical Planning Laboratory and Department of Neurosurgery Brain Tumor Database (Kaus et al. 2001; Warfield et al. 2000). The glioma is located in the superficial right frontal lobe (RFL) with a volume of 3.28 x 10^4 mm^3 and surface area of 1.49 x 10^4 mm^2. This location is related to non-literal language, personality, emotions and self-awareness (Shammi & Stuss 1999). Once the brain tumor mask was obtained from the MRI dataset, it was placed in the health model in two different ROIs. The first location was in the RFL region, where the tumor is originally situated. In order to make a comparison, the tumor was placed in a second location, the buried left occipital lobe (LOL), relative to visual processing (Grill-Spector et al. 1998).

WM electrical anisotropy conductivity was considered in the models. The anisotropy information was acquired from the diffusion tensor information of DTI images. To extract the information, the images were processed using FSL and a Matlab program (Bai 2012). It was considered that conductivity tensors share eigenvalues with diffusivity tensors (Basser, Mattiello & LeBihan 1994). The volume constraint (Wolters et al. 2006) was applied to estimate the WM anisotropy conductivity. Hence, the σ_{wm} anisotropy was modelled to be prolate, according to the following equation:

$$\boldsymbol{\sigma_{wm} = S diag(\sigma_{long}, \sigma_{trans}, \sigma_{trans}) S^{-1}} \quad \textbf{(21)}$$

where $\boldsymbol{S}$ is the orthogonal matrix measured from the diffusion tensors; and σ_{long} and σ_{trans} are the longitudinal (parallel) and transversal (perpendicular) conductivity parameters. A fixed ratio of 10:1 was used, given the values of $\sigma_{long} = 0.65\ S/m$ and $\sigma_{trans} = 0.065\ S/m$. More information about the processing of the diffusion to conductivity information was described in Section 3.2.5. In models constructed here, anisotropy was not considered in the tumor region.

The mesh was generated with the software ScanIP. The coarseness was set to -20 and the volumetric mesh comprised of approximately 2 million tetrahedral elements. Afterwards, the mesh was exported to COMSOL Multiphysics 5.1, where the physics and boundary conditions were applied. The models took from 5 to 16 minutes to run, according to the configuration used.

The three conventional electrode configurations BF, BL and RUL are applied. The details of their configurations are described in Section 3.3.

For comparison purposes, one control model and several other models with different tumor grades (from I to IV), and with and without WM electrical anisotropy conductivity, are constructed. In this way, a total of 19 models were generated for each electrode montage.

For the control models, the tumor geometry was included but modelled as health tissue, sot that all the models were similarly generated with the same amount of tetrahedral elements.

7.2.2. Quasi-static Approximation and Boundary Conditions

Biological tissues are typically considered as volume conductors, where there are no inductors, and only resistances and capacitances are distributed throughout a 3D region (Bai, Loo & Dokos 2013; Malmivuo & Plonsey 1995). In low frequencies, a simplification of the Maxwell's equation can be realized, resulting in the Laplace equation (Equation 1).

$$\nabla \cdot \left(-\sigma \nabla V\right) = 0 \quad \text{or} \quad \boldsymbol{\nabla}\cdot \begin{bmatrix} \sigma_{xx} & \sigma_{xy} & \sigma_{xz} \\ \sigma_{yx} & \sigma_{yy} & \sigma_{yz} \\ \sigma_{zx} & \sigma_{zy} & \sigma_{zz} \end{bmatrix} \begin{bmatrix} {\partial V}/{\partial x} \\ {\partial V}/{\partial y} \\ {\partial V}/{\partial z} \end{bmatrix} = 0 \text{ in } \Omega \qquad (1)$$

Electrical conductivity to each tissue was assigned, which is represented in Table 7.1. The electrical conductivity of the electrodes was considered as 9.8×10^5 S/m.

Initial and boundary conditions were applied to formulate the problem. The exposed BC is electrically insulated ($V = 0\ V$); the internal boundaries are ruled by conductivity ($(n \cdot J_1)|_{\Gamma_i} = (n \cdot J_2)|_{\Gamma_i}$); for the electrodes, the exposed surface of the cathode is assigned Dirichlet BC (*V = 0 V*), while the exposed surface of the anode is assigned a voltage equivalent to input current of 800 mA.

Table 7.1. Isotropic electrical conductivity of tissues (Datta, Elwassif & Bikson 2009; Hasgall PA 2014).

	σ (S/m)
Scalp	0.465
Fat	0.0406
Skull	0.0132
Muscles **eye muscles**	0.267
Eyes	0.52
Eye lens	0.2
CSF	1.654
GM	0.33
WM	0.65
Red nucleus	0.109
Putamen	0.32
Thalamus	0.089
Hippocampus	0.089
Fornix crura	0.32
Caudate nucleus	0.32
Hindbrain	0.109
Globus pallidus par externa / par interna	0.32

7.3. Simulations and Results

7.3.1. Realistic Head Model

The spatial distributions of the electric field for the control isotropic and anisotropic models are shown in Figure 7.1.

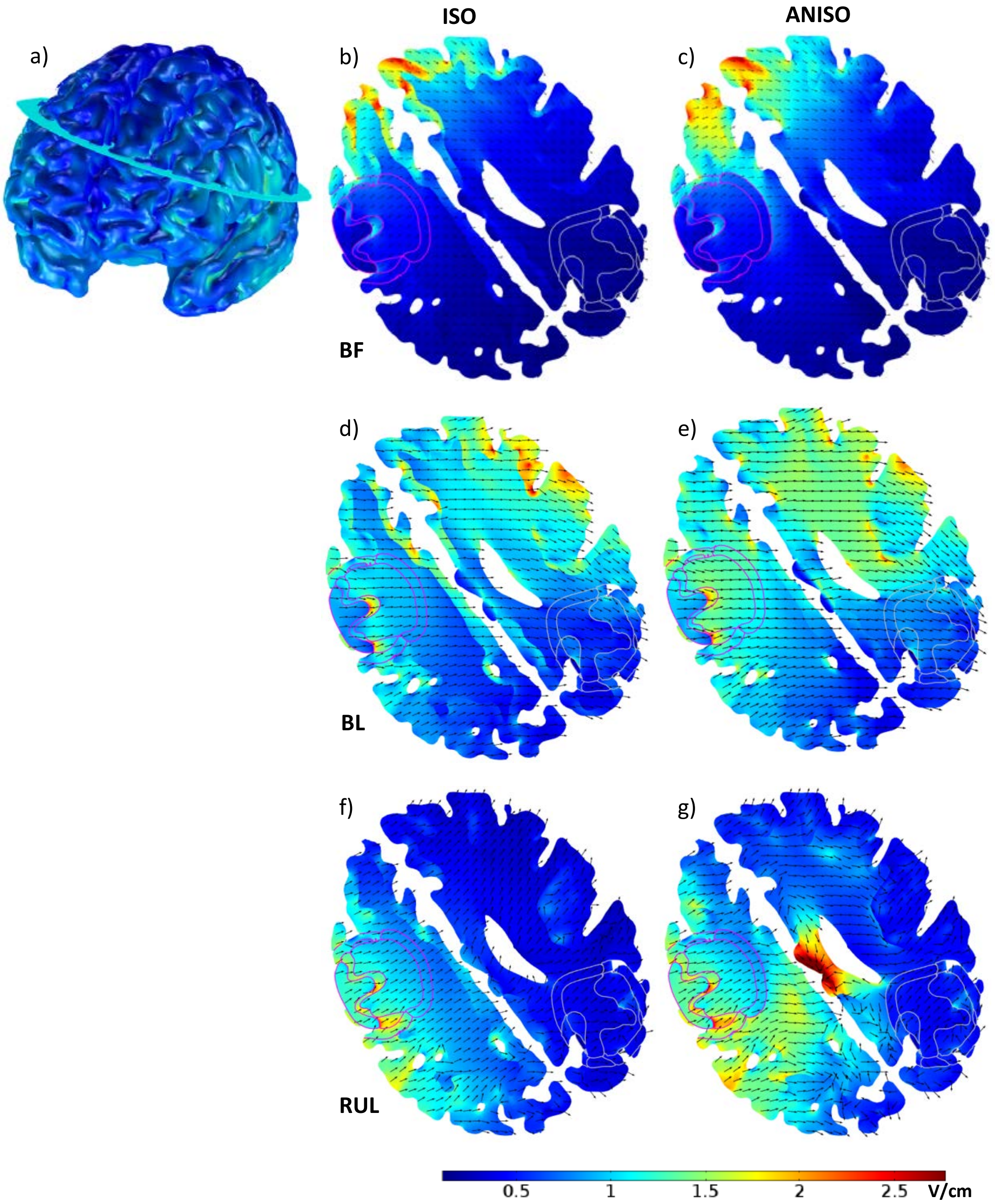

Figure 7.1. 3D brain geometry showing slices of a 30º plane (a) crossing both tumors, delineated magenta area for tumor RFL and grey area for tumor LOL. Slices of brain tumor, with the false color map being the magnitude of E-field and current density represented by the black arrows. (b, c) BF; (d, e) BL and (f, g) RUL. ISO – isotropic; ANISO – anisotropic.

Different behaviour due to the electrode montage and influence of anisotropy could be noticed in Figure 7.1. The E-field is higher in regions closer to the electrode. The region of tumor LOL (delineated at grey colour) does not receive much electrical stimulation, when compared to the strong stimulation received by tumor RFL (delineated in pink colour). The current densities suffer influence of the fiber paths in the anisotropy models.

7.3.2. Evaluation of Electrode Montages and WM Anisotropy Effect

Figure 7.2 and Figure 7.3 show bar plots of the maximum and the median E-field. For different ROIs, a comparison among the electrode configurations and the isotropic and WM anisotropic cases are made. These cases are considered as the control cases, where the tumor is assigned as healthy tissue. The median E-field (E_{med}) for GM is 0.34, 1.01 and 0.61 V/cm; while for WM is 0.30, 0.83 and 0.53 V/cm for BF, BL and RUL isotropic, respectively.

Overall, the BL configuration generates the strongest E-field and highest E_{med}. In the ROIs of hippocampus, thalamus and ventricles, the values with BL are 2 to 3 times stronger than with BF and RUL. However, when analysing the region of tumor RFL, it is RUL configuration which has the highest E_{med}.

The region of tumor RFL receives a stronger field, when compared to the region of tumor LOL. This behaviour is due to the locations of the tumors in the head and the placement of the electrodes. The E-field path is stronger in regions where the electrodes are located. The three electrode configurations used in this study are placed in frontal and medial regions of the head. Therefore, the occipital region, where the tumor LOL is located, will receive a weak E-field.

The RFL tumor has E_{med} of 0.50, 1.09 and 1.19 V/cm in isotropic cases and 0.51, 1.26 and 1.34 V/cm in anisotropic cases, for BF, BL and RUL configurations, respectively; while LOL tumor has E_{med} of 0.17, 0.60 and 0.36 V/cm in isotropic cases and 0.18, 0.68 and 0.43 V/cm in anisotropic cases, for BF, BL and RUL, respectively. Overall, when considering WM anisotropy, the E-field increases in all ROIs. The increase is of 2 to 15 % at tumor RFL, 6 to 19 % at tumor LOL, 4 to 14 % at GM, 33 to 52 % at WM, 7 to 17 % at hippocampus, 4 to 12 % at ventricles, depending on the electrode configuration used. Only at thalamus with RUL does it decrease about 3 %, and with BF and BL it increases 8 to 9 %.

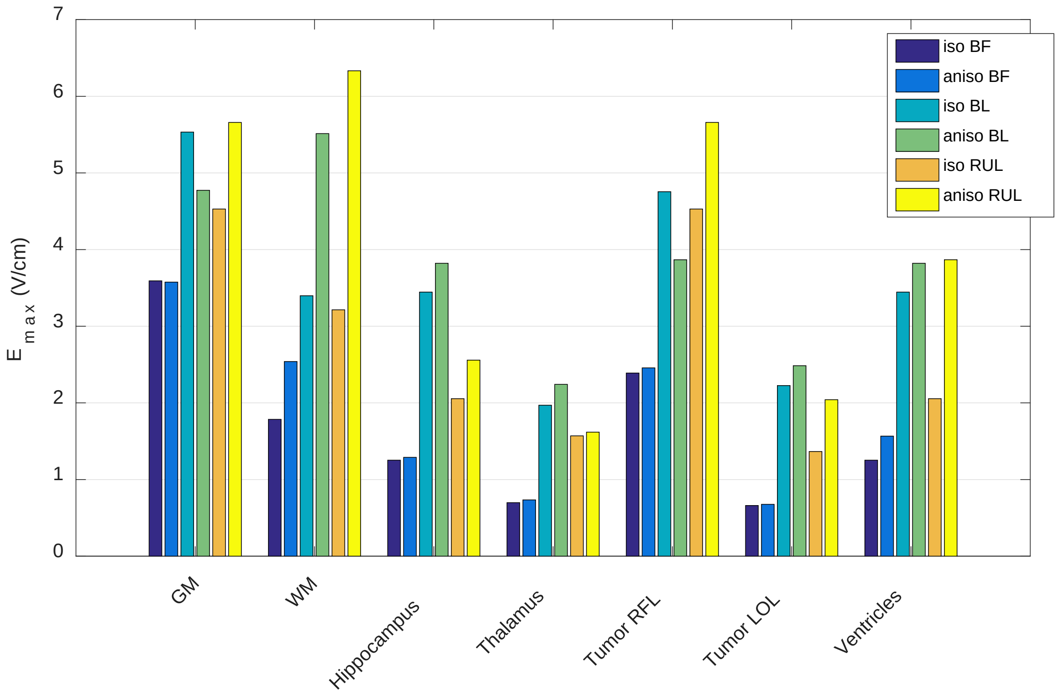

Figure 7.2. Maximum E-field magnitude for the isotropic and anisotropic control cases, at different ROIs (a) GM, (b) WM, (c) hippocampus, (d) thalamus, (e) tumor RFL, (f) tumor LOL and (g) ventricles.

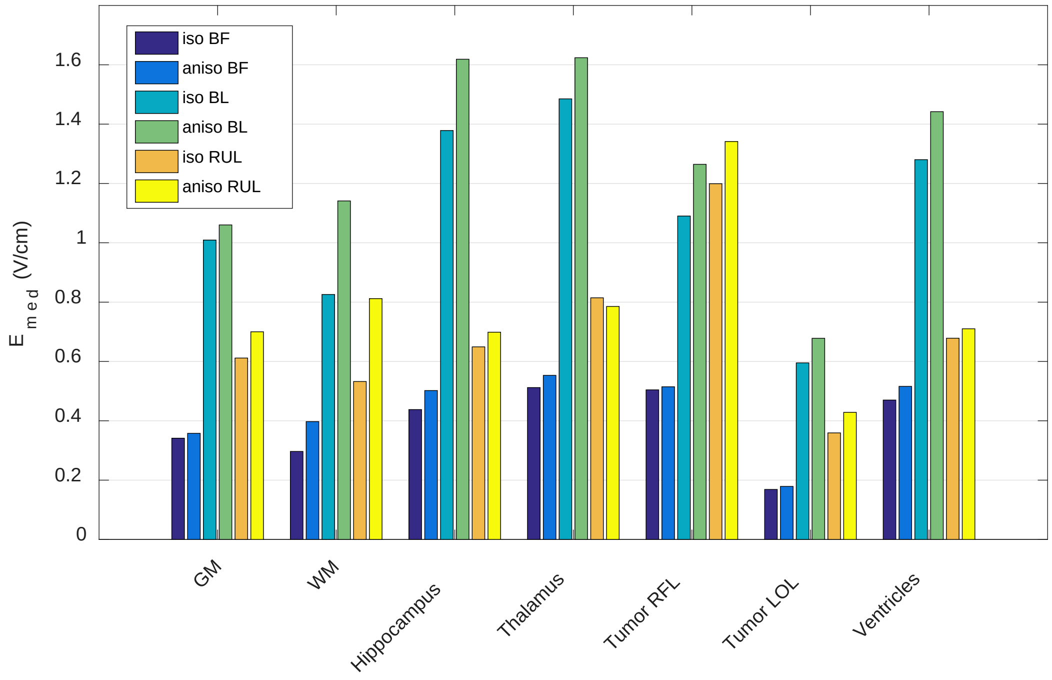

Figure 7.3. Median E-field magnitude for the isotropic and anisotropic control cases, at different ROIs (a) GM, (b) WM, (c) hippocampus, (d) thalamus, (e) tumor RFL, (f) tumor LOL and (g) ventricles**.**

The weaker E-field is generated through BF configuration. For all analysed ROIs, BF montage is the one where the E-field is lowest. This is due to the location of the electrodes. BF is a frontal configuration, making the electric field higher in frontal regions of the model. Therefore, it generates a weak field in the brain and cortical structures. On the other hand, BL configuration has the strongest effect on the brain and cortical structures. As a bilateral montage, placed in a median position of the head, it strongly affects the brain and other structures.

The influence of WM anisotropy conductivity is analysed. Figure 7.4 shows, quantitatively, the relative error of the E-field magnitude for certain ROIs. The variation from the isotropic model to the anisotropic is 11 %, 11 % and 17 % in GM and 33 %, 29 % and 41 % in WM, for BF, BL and RUL configurations, respectively. The highest REs for hippocampus, thamalus and ventricles are 18 %, 12 % and 17 %, respectively. REs in the regions of the tumor vary from 6 % to 18 % for RFL and from 8 %

to 20 % for LOL. As anisotropy is considered only in the WM, this is the tissue with highest effect. However, the E-field changes in the entire model.

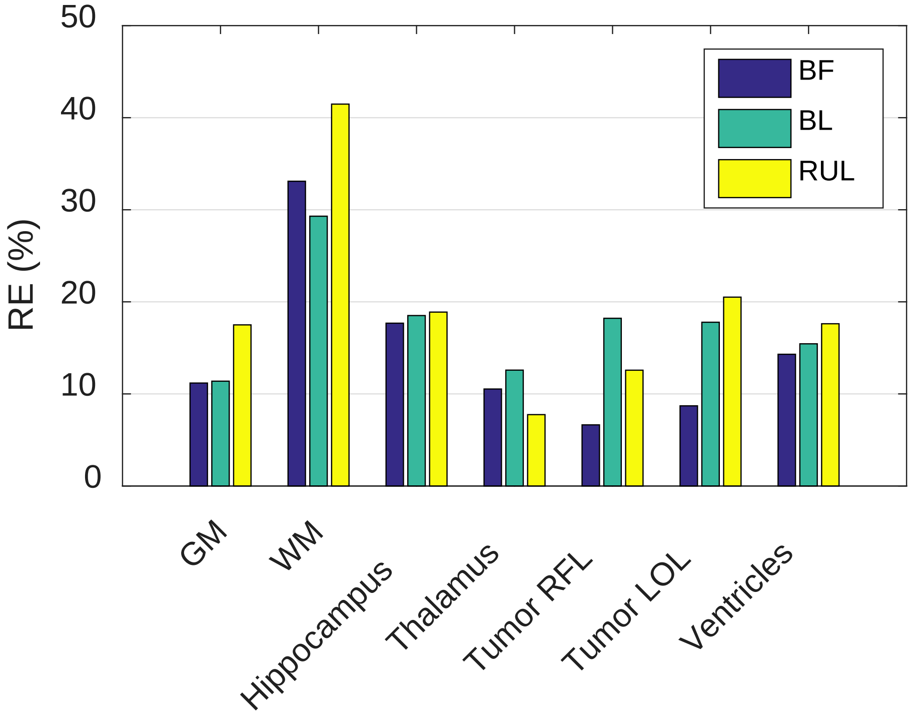

Figure 7.4. RE E-field magnitude at control case for different ROIs (a) GM, (b) WM, (c) hippocampus, (d) thalamus, (e) tumor RFL, (f) tumor LOL and (g) ventricles.

Figure 7.5 shows the percentage of the total volume for specific ROIs in the control cases, with comparisons among isotropic and anisotropic and the electrode montages being made. In general, the percentage is higher for anisotropic cases, when compared to its corresponding isotropic model. As BL has the strongest field, it also has the higher percentage. Correspondingly, BF has the weakest field and the smallest percentage.

In the GM region (Figure 7.5a), the percentage volume that is higher than 1 V/cm is 8.96 %, 50.64 % and 26.62 %, for BF, BL and RUL, respectively, in isotropic cases. The anisotropy models show an increase of 1 – 3 %, when compared to their corresponding isotropic models. On the other hand, at WM (Figure 7.5b) the percentages in isotropic cases are 1.88 %, 29.07 % and 13.33 %, while in anisotropic cases they are 7.88 %, 60.33 % and 33.02 %, for BF, BL and RUL, respectively. Being the region where anisotropy is included, WM suffered the highest variation in RE. It is also noted that when considering isotropy, the BF model has no field higher than 2 V/cm at WM. However, if considering anisotropy, the magnitude of the E-field reaches values higher than 2.5 V/cm.

Hippocampus, thalamus and ventricles (Figure 7.5c, d and g) are regions with higher percentages above 1 V/cm, at least with the BL configuration. For this montage, the percentage is 86.28, 92.95 and 83.56 for isotropy and 88.92, 94.93 and 86.43 for anisotropy, for hippocampus, thalamus and ventricles, respectively. For the RUL case the number is smaller, reaching respectively 11.60 %, 34.38 % and 16.98 %, for isotropy and 25.73 %, 32.92 % and 20.25 % for anisotropy; whereas for BF montage, these numbers are less than 1 % or null.

The region of tumor RFL (Figure 7.5e) also receives high E-field when BL and RUL configurations are applied. The percentage of total volume above 1 V/cm is of 6.98, 61.22 and 75.01 in isotropy, and 7.95, 78.32 and 81.36 in anisotropy, for BF, BL and RUL respectively. On the other hand, the electric field is much smaller in the LOL tumor region (Figure 7.5f). The E-field above 1 V/cm is of 6.12 % for isotropy and 9.96 % for anisotropy, RUL configurations; whereas it is less than 1 % for RUL and null for BF.

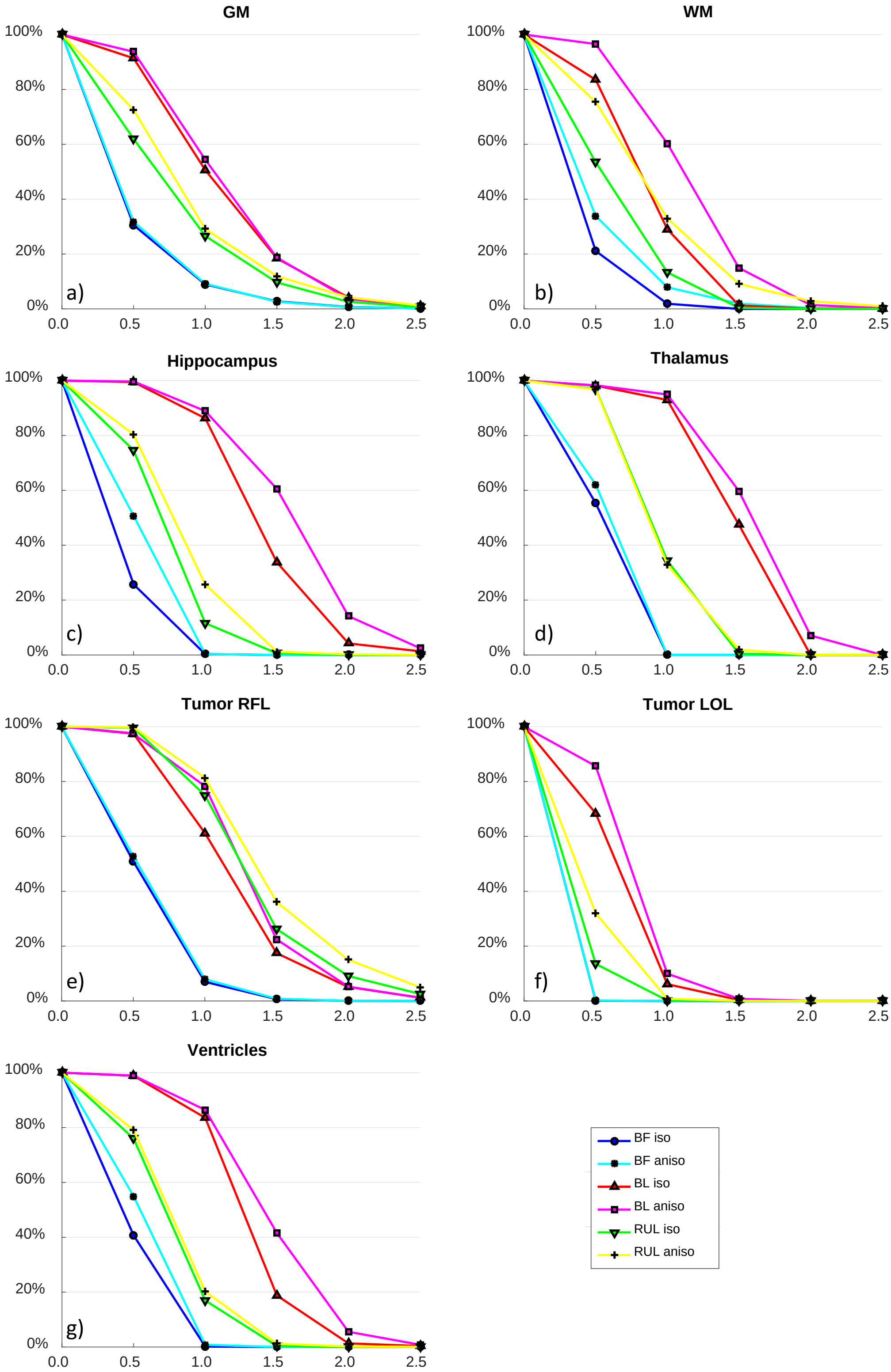

Figure 7.5. Percentage of the total volume that exceeds the E-field in the horizontal axis (V/cm), for three electrode configurations, control isotropic and anisotropic cases and different ROIs (a) GM, (b) WM, (c) hippocampus, (d) thalamus, (e) tumor RFL, (f) tumor LOL and (g) ventricles.

7.3.3. Tumor Grade Influence and Location of Tumor

It is known that tumorous tissues have higher electrical conductivity than healthy tissues (Gabriel, Gabriel & Courhout ; Halter et al. 2011; Zou & Guo 2003). For this reason, here the electrical anisotropy of the tumors is varied and selected higher than the nominal value. The higher value is almost equivalent to CSF electrical conductivity (Van Lier et al. 2011). Figure 7.6 shows the magnitude of the median E-field for the control case and four different tumor grades, and a comparison is made among different electrode configurations and with and without anisotropy, in different ROIs.

7.3.3.1. Tumor RFL

When analysing the effect of tumor RFL, overall BF has a weaker E-field and RUL the strongest E-field. As the tumor grade increases, E_{med} decreases. This behaviour happens in the tumor region and also in its neighbour regions that are directly affected. Therefore, the equivalent behaviour happens at GM, WM, and Hippocampus. On the other hand, regions which are remote from the tumor are only directly affected if the electrode configuration generates a strong field, like in BL and RUL montages. In regions where the E-field is weaker, the E_{med} remains almost the same. This behaviour appears in the region of tumor LOL, thalamus and ventricles with BF stimulation.

7.3.3.2. Tumor LOL

Tumor LOL has different behaviour from that of tumor RFL. In the tumor LOL case, the grade difference mainly impacts on the region of the tumor LOL itself. In the region of the tumor, it is observed that as long as the tumor grade increases, the E_{med} decreases. For other ROIs, the E-field shows variation depending upon the control case and the tumor grade case. When varying the tumor grades, generally the same E-field magnitude is delivered. This behaviour is due to the location of the tumor at the rear area of the head, and the location of the electrodes, on the middle to frontal area.

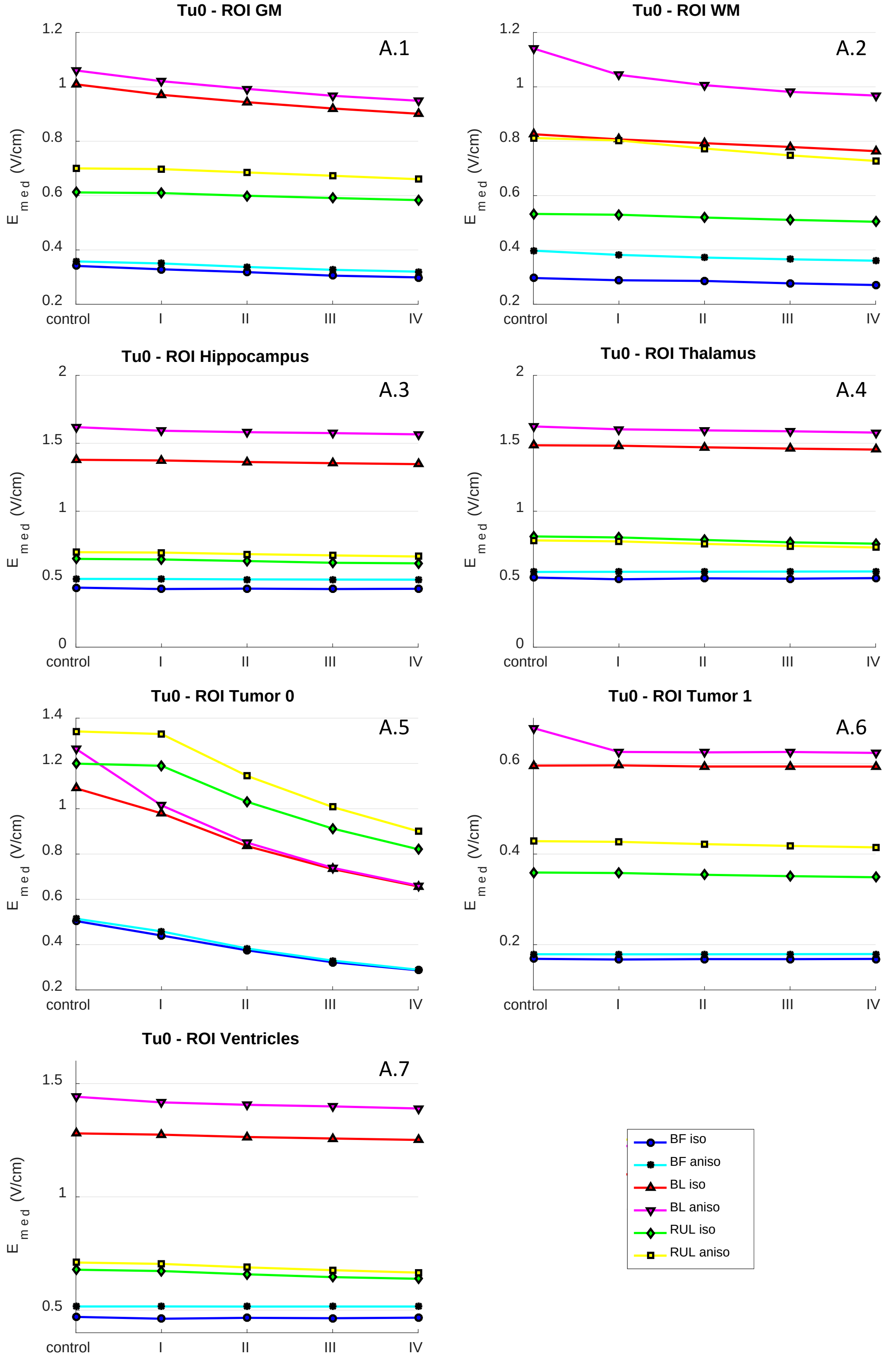
Tu0 - ROI GM
A.1
1.2
1
0.8
0.6
0.4
0.2
E med (V/cm)
control
I
II
III
IV
Tu0 - ROI WM
A.2
1.2
1
0.8
0.6
0.4
0.2
E med (V/cm)
control
I
II
III
IV
Tu0 - ROI Hippocampus
A.3
2
1.5
1
0.5
0
E med (V/cm)
control
I
II
III
IV
Tu0 - ROI Thalamus
A.4
2
1.5
1
0.5
0
E med (V/cm)
control
I
II
III
IV
Tu0 - ROI Tumor 0
A.5
1.4
1.2
1
0.8
0.6
0.4
0.2
E med (V/cm)
control
I
II
III
IV
Tu0 - ROI Tumor 1
A.6
0.6
0.4
0.2
E med (V/cm)
control
I
II
III
IV
Tu0 - ROI Ventricles
A.7
1.5
1
0.5
E med (V/cm)
control
I
II
III
IV
BF iso
BF aniso
BL iso
BL aniso
RUL iso
RUL aniso

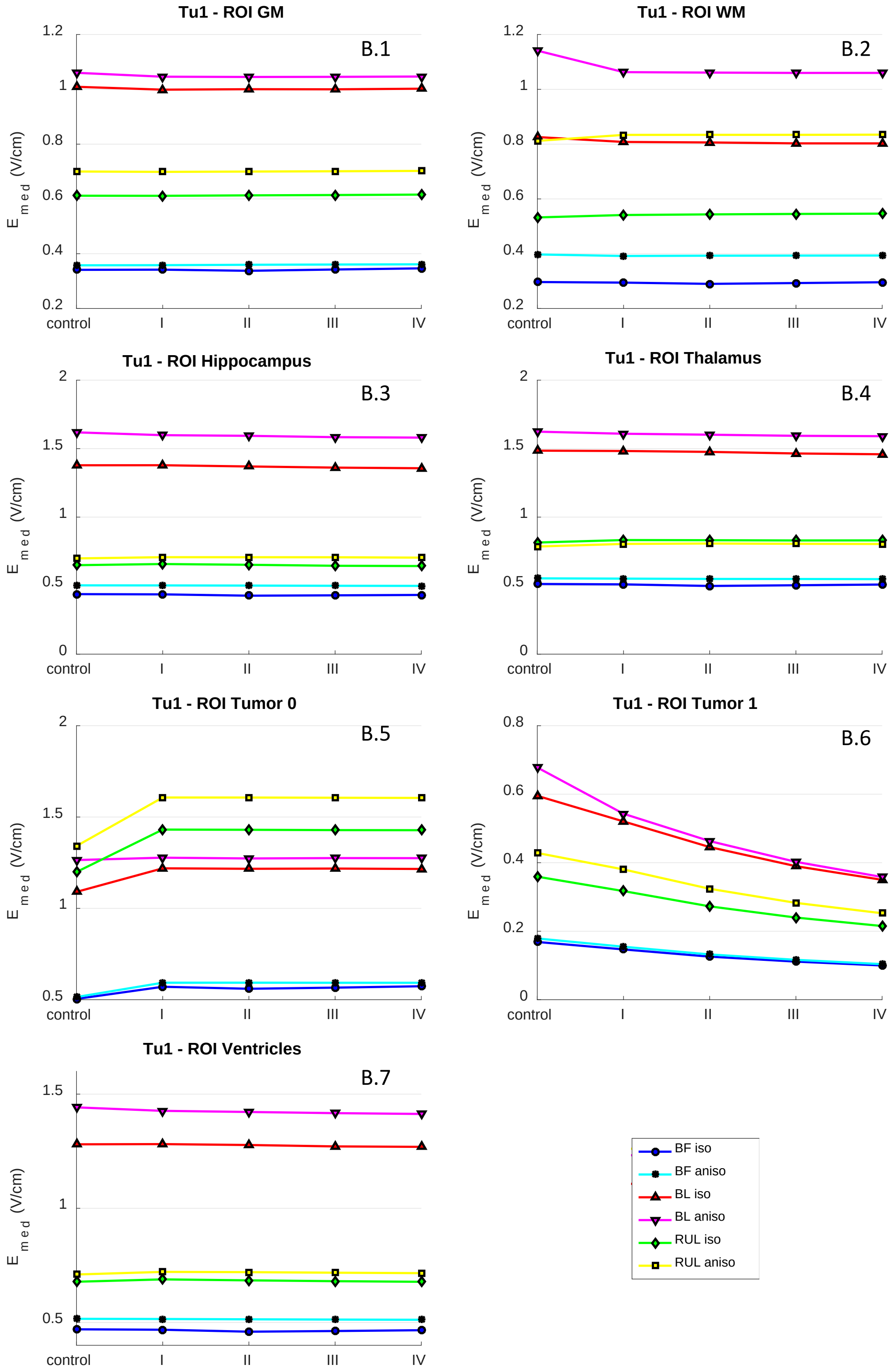

Figure 7.6. Graph of E_{med} for the control case and the four different tumor grades considered, for BF, BL and RUL. (A) Tumor RFL active (Tu0), (B) Tumor LOL active (TU1). (1) GM, (2) WM, (3) hippocampus, (4) thalamus, (5) tumor RFL (tumor 0), (6) tumor LOL (tumor 1) and (7) ventricles.

The percentage of total volume is also calculated for the different grades of tumor. However, as previously mentioned, those differences are normally more evident in the tumor region. Figure 7.7 shows these values for tumor regions and all tumor grades.

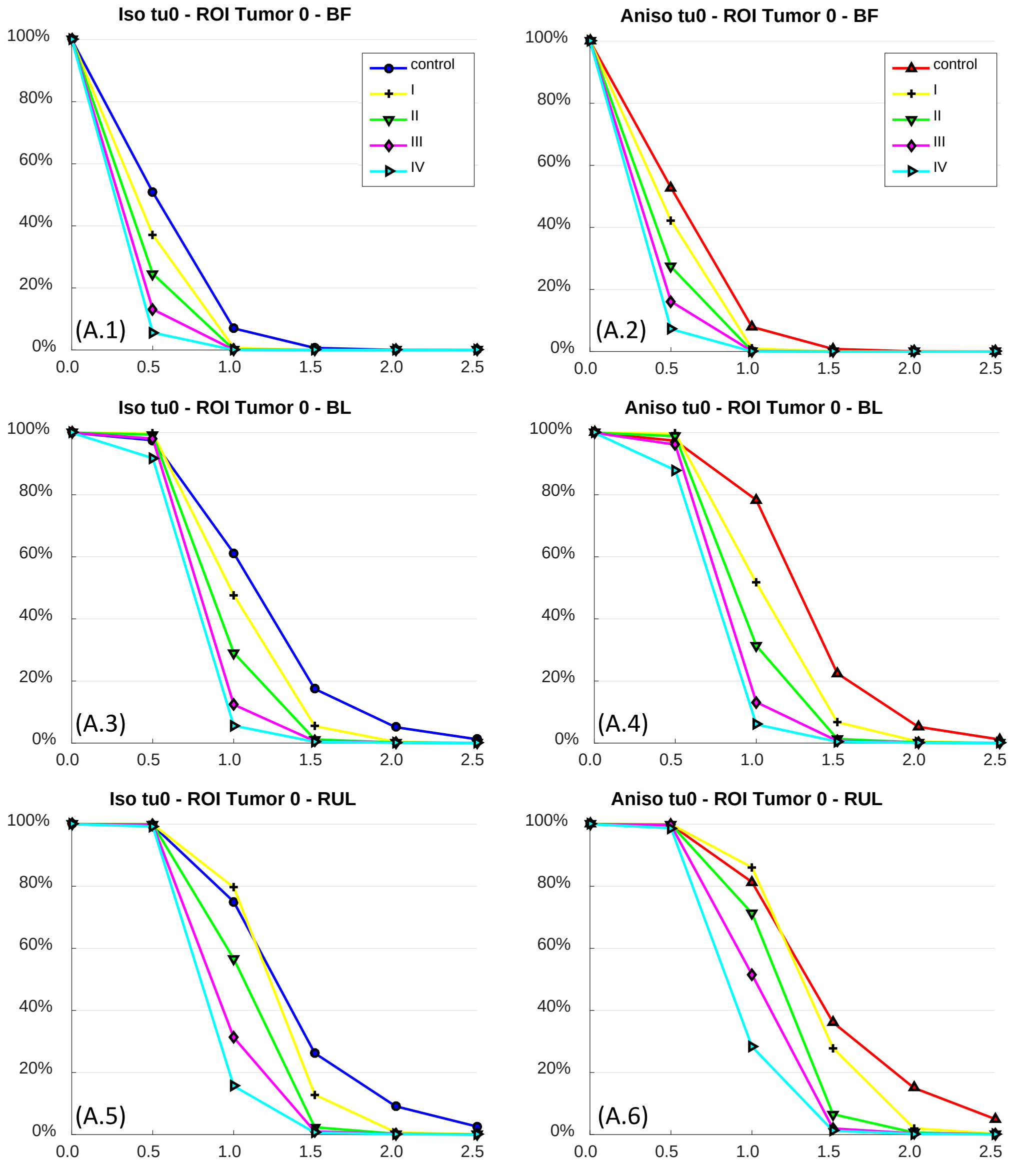

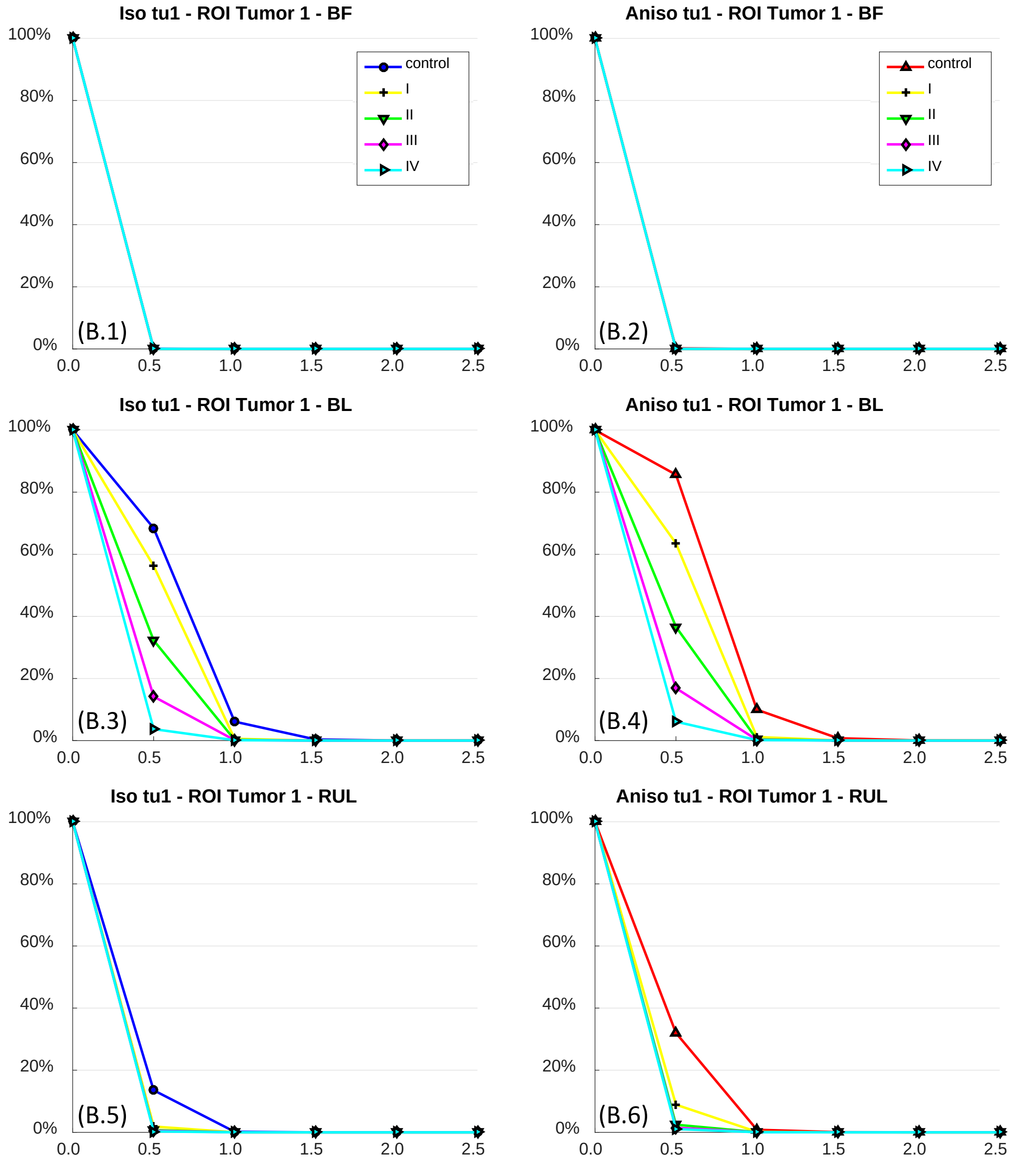

Figure 7.7. Percentage of total volume for tumor region, (A) Tumor RFL (Tumor 0), (B) Tumor LOL (Tumor 1), for BF (first row), BL (second row) and RUL (third row); isotropic (Iso) (first column) and WM anisotropic (Aniso) (second column). tu0 – Tumor 0 active; tu1 – Tumor 1 active.

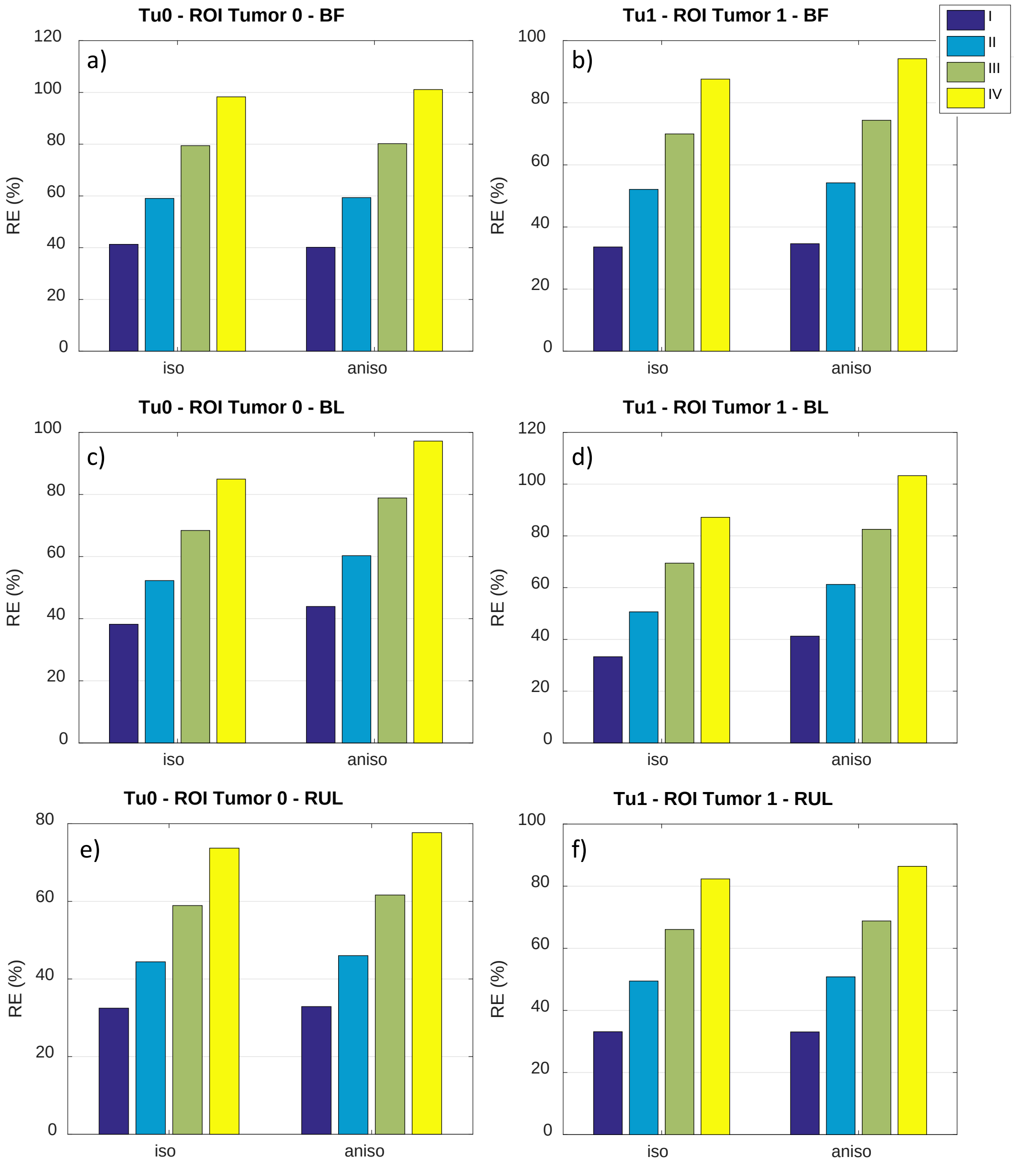

Figure 7.8. E-field RE of ROI Tumor RFL (tumor 0) at first column and Tumor LOL (tumor 1) at second column, for all tumor grades, at BF (first row), BL (second row) and RUL (third row).

When analysing tumor aggression, it can be observed that the effect of the electric field is higher on tumor RFL than on tumor LOL. For tumor RFL, as long as the tumor grade is increased, the E-field decreases. For all electrode configurations, the E-fields are higher than 1 V/cm and the highest is greater than 2.5 V/cm. On the other hand, the equivalent behaviour only happens for electrode configuration BL at Tumor LOL. In the BF montage, the control and all tumor grades have no values higher than 0.5 V/cm; and in RUL only the control cases reach values up to 1 V/cm and the grade difference is negligible.

Figure 7.8 demonstrates the bar graphs of the relative error of E-field in tumors RFL and LOL. The results shown are for the isotropic cases, comparing the control case to the tumor grade cases, as well as to the anisotropic cases. It is observed that RE increases as long as tumor grade increases. Also, when applying WM anisotropy, RE is slightly higher compared with the isotropic study. Besides, for the electrode montages, BF has bigger values for tumor RFL, while BL has greater values for tumor LOL. In general, the values are higher for tumor LOL, with the exception of BF configuration.

7.4. Comparisons and Discussions

At first, the models considered here modelled the tumor as a healthy region, as in the control case (Figure 7.2 and Figure 7.3). Magnitudes higher than 2.5 V/cm can be found in most of the analysed ROIs (Figure 7.5), depending on the electrode montages. BL configuration has a stronger E-field, while BF montage has a weaker one. These results concur with findings in the literature (Bai et al. 2012; Lee et al. 2012; Lee et al. 2011). BL is stronger due to the bilaterality and location of electrodes; it makes the E-field pass through the entire head volume, having a high impact on the brain. Despite having a bilateral location, BF is a frontal montage, so its effect is reflected more on frontal regions of the head (Figure 7.1).

Current flows through the region of lower conductivity and follows the fiber paths in anisotropic models. When WM anisotropy is considered, changes in the E-field occur in all analysed ROIs. In general, an increase happens and the amounts vary from 2 % to 52 % in the E_{med}, being higher at RUL at WM (Figure 7.2 and Figure 7.3). When considering anisotropy, structures that are further from the electrode have higher relative error. As seen in Figure 7.4, RE from hippocampus and ventricles is higher than RE from GM. Also, the relative error at tumor LOL is higher than at tumor RFL. The

RE found in our study was up to 41 %. Lee et al. (2012) also analysing ECT, reported relative errors up to 39 % when considering WM anisotropy. The inclusion of WM anisotropy in the study of electroencephalographic scalp potentials (Wolters et al. 2006), tDCS (Sadleir et al. 2010) and TMS (Thielscher, Opitz & Windhoff 2011) showed RE of 30 %, 39 % and 10 %, respectively. TMS has smaller relative errors as the E-field is more superficial when compared to ECT and tDCS. Thus, our results of 41 % in relative error, when including WM anisotropy, do mirror existing literature findings.

Overall, the E-field decreases when the tumor grade increases (Figure 7.6 and Figure 7.7), and the control cases have higher E-field in the tumor regions, due to increasing electrical conductivity in the tumor. The location of the tumor is another important factor to consider. The effect of E-field in the tumor RFL is higher than that in the tumor LOL (Figure 7.7), due to its location. Tumor LOL is in the rear region of the brain, not exactly in the path of ECT stimulation. Depending of the electrode configuration and tumor location, the grade of tumor appears immaterial. In these cases, the E-field is low, in the range of 0.5 V/cm, as for BF at tumor LOL (Figure 7.7B.1). On the other hand, even the highest tumor grade (IV) may receive an E-field stronger than 1.5 V/cm (Figure 7.7A.3-6) with BL and RUL montages.

Variations of tumor location and grade affect E_{med} mainly in the tumor region. The median E-field is not altered in the other regions such as, GM, WM, hippocampus, thalamus and ventricles due to these configurations, as seen in Figure 7.6.

Hippocampus and thalamus are regions that may change if the patient suffers from depression (Campbell & MacQueen 2004; Schlaepfer et al. 2008). The E-field received from these regions is quite strong, and reached as high as 2.5 V/cm in some cases (Figure 7.5). In the necessity of administering ECT treatment to a depressed patient who has brain tumor, diverse factors need to be taken into consideration. The region of tumor LOL is not strongly affected by the electrical stimulation; while hippocampus, thalamus and ventricles can be stimulated in order to treat any neurological problem.

Laboratory studies in gliobastoma multiforme cells reported that electric field stimulation with frequencies of 200 kHz and amplitudes of 1-3 V/cm cause disruption in the cells (Kirson et al. 2007). ECT stimulations may have E-field magnitudes that reach values higher than 2.0 V/cm in the tumor itself (Figure 7.7A); however, ECT frequencies are low. The low frequencies used in ECT produce seizures, while at high frequencies the triggering of seizures is not effective (Peterchev et al. 2010). However, high frequencies interfere with mitosis and cytokinesis (Miranda et al. 2014), as is used at TTFields.

TTFields (Miranda et al. 2014; Wenger et al. 2015) is an electromagnetic stimulation technique approved by FDA to treat gliobastoma multiforme. It uses high frequencies (200 kHz) and high stimulation (1-3 V/cm), generating mitoses in cells, helping in the treatment and extending life expectancy of a few months. The E-field applied through this technique reaches values above 1 V/cm in the brain. If applying ECT, the equivalent E-field range can be reached, as shown in Figure 7.5. Furthermore, according to Kast et al. (2013), ECT opens the blood brain barrier, helping in chemotherapy treatment if ECT has been previously applied. The high E-field and the possibility of opening the blood brain barrier are an indication that ECT may be helpful in tumor treatment. On the other hand, care should be taken as ECT stimulation may increase intracranial pressure (Huang, Hsieh & Liao 2010) and cause seizures (Peterchev et al. 2010; Weiner 2002).

A tDCS study with a brain tumor (Song et al. 2016) showed that due to the low stimulation of tDCS, it is safe to treat neuropsychiatric problems and cancer pain in patients with a brain tumor. They also stated that current density distributions changed due to the presence of a tumor. In the same way, in our study, the E-field is modified in the presence of a tumor.

Yacoob and Hassan (2012) simulated noninvasive hyperthermia in a head model containing a 3.14 cm^2 brain tumor. An air-filled ellipsoidal chamber, an antenna and a human head model were simulated and used to measure SAR (specific absorption rate) and temperature distribution. Three different models were considered, two simplified spherical models with the tumor in the centre, and one realistic model with the tumor artificially placed in the head. Using this approach, they were able to heat the brain tumor, without harming the normal tissues. This work also analysed the effect of temperature. Temperature increases occurred mainly in areas of the scalp and fat, in regions close to the electrode. Temperature did not increase in brain areas due to ECT electrical stimulation. This similar behaviour was also found in our previous studies.

It is know that the features of T1 and PD from MRI do change in the presence of a brain tumor. As reported in Tofts (2003), PD increases 14 to 20 percentage unit, when compared to normal WM. Also, an increase in T1 appears. Furthermore, in the presence of pathology, the T1 may alter too. An increase in T1 appears in the presence of oedema around tumors (Gowland; & Stevenson 2003). In this study, a realistic tumor was applied to a healthy subject model. Therefore, some small variations may occur if modelling MRI images of a patient with a brain tumor, in which case the geometric shape of brain regions may differ, which may alter the results when ECT stimulation is delivered. However, the different cases modelled and the different tumor grades considered in this study are a good approach to understanding the behaviour and influence of electric field in the presence of a brain tumor. For further studies, MRI and DTI images of a patient with a brain tumor may be developed and compared with the present one.

In summary, in the necessity of applying ECT to a patient with a brain tumor, depending on the location of the tumor, the E-field has little influence on the tumor itself. The electrode configuration also plays a role in the quantity of E-field received. The more malignant the tumor, the less E-field is received in the tumor region.

7.5. Conclusions

Two brain tumors are included in the realistic model RHM_17. Four tumor grade malignancies are considered and WM anisotropy conductivity is also included. In simulations, three different electrode montages are applied. From the results obtained, it is possible to conclude that ECT treatment may be administered to a patient with a brain tumor and the dose parameters are dependent on the tumor location, tumor grade and electrode montages.

8. CONCLUSION AND FUTURE DIRECTION

In this study, an incremental methodology is applied to address the challenges in human head modelling and thermal behaviour for ECT. Firstly, a simplified spherical model is developed and implemented. The temperature behaviour due to ECT electrical stimulation is investigated. Then, the MRI and DTI images are used to construct realistic human head models with detailed anatomical features. With these realistic models, the roles of tissue heterogeneity, electrode montage, thermal and electrical anisotropy conductivity, and structural details are assessed systematically. Finally, brain tumor patients are considered and the effect of brain tumors on electric field under ECT are analysed.

8.1. Main Contributions

1. The structure of how to develop a human head model with thermal and electrical perspectives, under ECT.
    a. A heterogeneous spherical human head model and high-resolution human head model are developed with MRI datasets.

    Models are constructed using the BHTE and Laplace equation to simulate thermal and electrical physics due to ECT stimulation. Three ECT electrode configurations (BF, BL and RUL) are used. The results from the realistic models are compared with the spherical ones.

   b. The effect of temperature variations on both the head and the brain.

From the thermal point of view, the brain is safe and no temperature increase occurs. Rises in temperature will only occur on external layers of the human head in regions near the electrode. The scalp and the skull protect the brain thermally. The brain only reaches temperatures above 38 ºC when high input currents are applied, greater than 1.75 A.

   c. The effect of biological properties on induced temperature variation

By varying parameters in the scalp layer, when increasing the electrical or the thermal conductivity, the temperature drops; also,a rise in blood perfusion occurs with a slight drop in temperature. The non-inclusion of a fat layer in the ECT human head model may result in a 20 % drop in T_{max}.

2. Incorporate tissue anisotropy in spherical and realistic head models and investigate their influences.

   a. Derive and include skull anisotropy thermal conductivity using linearity relationship between thermal and electrical conductivity.

The skull anisotropy thermal conductivity is implemented in the spherical model through correlation with anisotropic electrical conductivity. No significant variation between the volume constraint and the Wang constraint are found. Also, provided the anisotropy ratios increase, the temperature drops slightly.

   b. Inclusion of thermal, electrical and thermal+electrical anisotropy conductivity in the skull.

The three variations of skull anisotropy conductivity are implemented in the spherical and realistic human head models, considering the volume constraint. The outcomes show that thermal anisotropy conductivity does not have a significant influence on temperature behaviour. However, with the inclusion of electrical anisotropy conductivity, temperature rises. Also, as long as the electrical anisotropy ratio increases, the temperature decreases. Additionally, scalp, fat, skull and CSF could reach temperatures above 38 ºC.

3. Influence of a brain tumor in the ECT electrical stimulation.

    a. Develop and construct a realistic head model with a brain tumor and WM anisotropy electrical conductivity.

    Two different brain tumor locations are considered (RFL and LOL). Electrical anisotropy conductivity of white matter is implemented using DTI images and the conductivity information is obtained by applying the volume constraint.

    b. The effects of tumor location, tumor aggressiveness, WM anisotropy electrical conductivity and electrode montage on the E-field in a head model are investigated.

The E-field varies according to the tumor location, tumor aggressiveness, inclusion of anisotropy and electrode montage used. The tumor RFL receives up to 3.33 % higher E-field than tumor LOL, because of its location closer to the electrodes and in the path of current density. Also, the strongest median E-field overall is through BL configuration, due to its bilaterality and median position. The E-field in the analysed ROIs increases from 2 to 52 % with the inclusion of WM anisotropy. In the tumor regions, that rise is from 2 to 19 %, according to the electrode montage used. Finally, the increase in tumor aggressiveness causes a drop in E-field.

8.2. Future Work and Direction

Further work can be done to improve the current work, such as: to include detailed geometry and more tissues in modelling; to position electrodes for focality; to carry out neurochemistry analysis for anesthesia and other drugs and to include blood vessels and tractography. In particular, the author has identified the following topics for further investigations:

- Including the micro-architecture of the skin might explain skin irritation cases in ECT. An analysis can be performed to determine the ideal placement of electrodes accounting for both current magnitude required and temperature rise;
- Despite all efforts which have been made to acquire accurate data for electrical and thermal properties of human tissues, there are still uncertainties. The values may change according to subject, if in the presence of any pathology and the degree of pathology. Subject-specific models are important to analyse in a case by case study. Variations in thermal and electric field may be found due to changes in geometry;
- This study modelled the head from a macroscopic point of view, analysing and investigating the thermal and electric fields due to ECT stimulation. ECT changes some of the neurochemistry of the brain (Njau et al. 2016). The behaviour of neural stimulation and connections among neurons was not considered. Therefore, investigations at microscopic and mesoscopic levels and the effects that ECT electrical stimulation causes, are still unexplored. One way to address this issue is to add neurochemical signals brain information that can be acquired from proton magnetic resonance spectroscopy to the model (Bertholdo, Watcharakorn & Castillo 2013; Njau et al. 2016);
- Prior to ECT stimulation, general anaesthesia and muscle relaxants are given to the patient (Weiner 2002). These drugs cause changes in body temperature. However, the influence and effect of these drugs is not considered in the

models designed in this thesis. In order to acquire more realistic results, these factors should be included in the simulations;

- It is well know that blood vessels may change the temperature of tissues (Wang et al. 2014). In the models considered in this study, the blood vessels are not included. Images of magnetic resonance angiography and automated software may be used to include a vascular network (Prishvin, Manukyan & Zaridze 2009; Van Leeuwen et al. 2000; Van Leeuwen, Kotte & Lagendijk 1998), in order to produce more realistic head models;
- This project is focusing on the modelling and simulation. The future work will be the validation of these numerical studies. Some work has been done using animals such as rat, cat, monkey, etc. by other researchers.

REFERENCES

Aubert-Broche, B, Evans, AC & Collins, L 2006, 'A new improved version of the realistic digital brain phantom', *Neuroimage*, vol. 32, no. 1, pp. 138-45.

Bai, S 2012, 'Computational Models of Electroconvulsive Therapy and Transcranial Direct Current Stimulation for Treatment of Depression', PhD thesis, UNSW, Australia.

Bai, S, Loo, C & Dokos, S 2011, 'Electroconvulsive therapy simulations using an anatomically-realistic head model', in Engineering in Medicine and Biology Society, EMBC, 2011 Annual International Conference of the IEEE: *proceedings of theEngineering in Medicine and Biology Society, EMBC, 2011 Annual International Conference of the IEEE* IEEE, pp. 5484-7.

Bai, S, Loo, C & Dokos, S 2013, 'A review of computational models of transcranial electrical stimulation', *Critical Reviews™ in Biomedical Engineering*, vol. 41, no. 1, pp. 21-35.

Bai, S, Loo, C, Al Abed, A & Dokos, S 2012, 'A computational model of direct brain excitation induced by electroconvulsive therapy: comparison among three conventional electrode placements', *Brain Stimul.*, vol. 5, no. 3, pp. 408-21.

Barton, MD & Trembly, BS 2013, 'Measurement of the anisotropic thermal conductivity of the porcine cornea', *Experimental eye research*, vol. 115, pp. 216-23.

Basser, PJ, Mattiello, J & LeBihan, D 1994, 'MR diffusion tensor spectroscopy and imaging', *Biophysical journal*, vol. 66, no. 1, pp. 259-67.

Berger, SA, Goldsmith, W & Lewis, ER 1996, *Introduction to bioengineering*, Oxford University Press, USA.

Berjano, EJ, Saiz, J & Ferrero, JM 2002, 'Radio-frequency heating of the cornea: theoretical model and in vitro experiments', *IEEE T. Biom. Eng.*, vol. 49, no. 3, pp. 196-205.

Bernardi, P, Cavagnaro, M, Pisa, S & Piuzzi, E 2003, 'Specific absorption rate and temperature elevation in a subject exposed in the far-field of radio-frequency sources operating in the 10-900-MHz range', *Biomedical Engineering, IEEE Transactions on*, vol. 50, no. 3, pp. 295-304.

Bertholdo, D, Watcharakorn, A & Castillo, M 2013, 'Brain proton magnetic resonance spectroscopy: introduction and overview', *Neuroimaging Clinics of North America*, vol. 23, no. 3, pp. 359-80.

Bezerra, L, Oliveira, M, Rolim, T, Conci, A, Santos, F, Lyra, P & Lima, R 2013, 'Estimation of breast tumor thermal properties using infrared images', *Signal Processing*, vol. 93, pp. 2851-63.

Bezerra, LA, Oliveira, MM, Araújo, MC, Viana, MJ, Santos, LC, Santos, FG, Rolim, TL, Lyra, PR, Lima, RC, Borschartt, TB, Resmini, R & Conci, A (eds) 2013, *Infrared imaging for breast cancer detection with proper selection of properties: from acquisition protocol to numerical simulation,* in Multimodality Breast Imaging: Diagnosis and Treatment, EYK Ng, U. Rajendra Acharya.

Boulby;, PA & Rugg, FJ 2003, 'T2: the Transverse Relaxation Time', in P Tofts (ed.), *Quantitative MRI of the Brain*, John Wiley & Sons Ltd., ch 6, pp. 143-201.

Bourantas, GC, Loukopoulos, VC, Burganos, VN & Nikiforidis, GC 2014, 'A meshless point collocation treatment of transient bioheat problems', *International journal for numerical methods in biomedical engineering*, pp. n/a-n/a.

Brown, LG 1992, 'A survey of image registration techniques', *ACM computing surveys (CSUR)*, vol. 24, no. 4, pp. 325-76.

Campbell, S & MacQueen, G 2004, 'The role of the hippocampus in the pathophysiology of major depression', *Journal of psychiatry & neuroscience: JPN*, vol. 29, no. 6, p. 417.

Cancelli, A, Cottone, C, Tecchio, F, Truong, DQ, Dmochowski, J & Bikson, M 2016, 'A simple method for EEG guided transcranial electrical stimulation without models', *Journal of neural engineering*, vol. 13, no. 3, p. 036022.

Casarotto, S, Canali, P, Rosanova, M, Pigorini, A, Fecchio, M, Mariotti, M, Lucca, A, Colombo, C, Benedetti, F & Massimini, M 2013, 'Assessing the Effects of Electroconvulsive Therapy on Cortical Excitability by Means of Transcranial Magnetic Stimulation and Electroencephalography', *Brain Topogr.*, vol. 26, pp. 326-37.

Chen, J-J, Zhao, L-B, Liu, Y-y, Fan, S-H & Xie, P 2017, 'Comparative efficacy and acceptability of electroconvulsive therapy versus repetitive transcranial magnetic stimulation for major depression: a systematic review and multiple-treatments meta-analysis', *Behavioural brain research*.

Christian, MM, Firebaugh, SL & Smith, AN 2012, 'COMSOL Thermal Model for a Heated Neural Micro-Probe', in Proc. COMSOL Conf. : *proceedings of theProc. COMSOL Conf.* pp. n/a-n/a.

Collins, CM, Liu, W, Wang, J, Gruetter, R, Vaughan, JT, Ugurbil, K & Smith, MB 2004, 'Temperature and SAR calculations for a human head within volume and surface coils at 64 and 300 MHz', *Journal of Magnetic Resonance Imaging*, vol. 19, no. 5, pp. 650-6.

Datta, A, Elwassif, M & Bikson, M 2009, 'Bio-heat transfer model of transcranial DC stimulation: comparison of conventional pad versus ring electrode', in EMBC-IEEE Ann. Int. Conf. IEEE. : *proceedings of theEMBC-IEEE Ann. Int. Conf. IEEE.* pp. 670-3.

Datta, A, Bansal, V, Diaz, J, Patel, J, Reato, D & Bikson, M 2009, 'Gyri-precise head model of transcranial direct current stimulation: improved spatial focality using a ring electrode versus conventional rectangular pad', *Brain stimulation*, vol. 2, no. 4, pp. 201-7.

De Munck, J 1988, 'The potential distribution in a layered anisotropic spheroidal volume conductor', *Journal of Applied Physics*, vol. 64, no. 2, pp. 464-70.

Deng, Z-D, Lisanby, SH & Peterchev, AV 2011, 'Electric field strength and focality in electroconvulsive therapy and magnetic seizure therapy: a finite element simulation study', *Journal of neural engineering*, vol. 8, no. 1, p. 016007.

Despotović, I, Goossens, B & Philips, W 2015, 'MRI segmentation of the human brain: challenges, methods, and applications', *Computational and mathematical methods in medicine*, vol. 2015.

Elwassif, MM, Kong, Q, Vazquez, M & Bikson, M 2006, 'Bio-heat transfer model of deep brain stimulation-induced temperature changes', *J. Neural Eng.*, vol. 3, no. 4, pp. 306-15.

Elwassif, MM, Datta, A, Rahman, A & Bikson, M 2012, 'Temperature control at DBS electrodes using a heat sink: experimentally validated FEM model of DBS lead architecture', *J. Neural Eng.*, vol. 9, no. 4, p. 046009.

Esser, AT, Smith, KC, Gowrishankar, T & Weaver, JC 2009, 'Towards solid tumor treatment by nanosecond pulsed electric fields', *Technology in cancer research & treatment*, vol. 8, no. 4, pp. 289-306.

Ezquerro, F, Moffa, AH, Bikson, M, Khadka, N, Aparicio, LV, Sampaio-Junior, Bd, Fregni, F, Bensenor, IM, Lotufo, PA & Pereira, AC 2016, 'The Influence of Skin Redness on Blinding in Transcranial Direct Current Stimulation Studies: A Crossover Trial', *Neuromodulation: Technology at the Neural Interface*.

Ferdjallah, M, Bostick, F & Barr, R 1996, 'Potential and current density distributions of cranial electrotherapy stimulation (CES) in a four-concentric-spheres model', *Biomedical Engineering, IEEE Transactions on*, vol. 43, no. 9, pp. 939-43.

Fertonani, A & Miniussi, C 2016, 'Transcranial Electrical Stimulation What We Know and Do Not Know About Mechanisms', *The Neuroscientist*, p. 1073858416631966.

Fiala, D, Lomas, KJ & Stohrer, M 1999, 'A computer model of human thermoregulation for a wide range of environmental conditions: the passive system', *J. Appl. Physiol.*, vol. 87, no. 5, pp. 1957-72.

Frank, E 1952, 'Electric potential produced by two point current sources in a homogeneous conducting sphere', *Journal of Applied Physics*, vol. 23, no. 11, pp. 1225-8.

Gabriel, C, Gabriel, S & Courhout, E 'l996. The dielectric properties of biological tissues: I. Literature survey', *Phys Med Biol*, vol. 41, no. 223, pp. l-2249.

Glasser, M 2009, *JiscMail, Email discussion lists for the UK Education and Research communities. Available from: <https://www.jiscmail.ac.uk/cgi-bin/webadmin?A2=FSL;3c23f260.0903> Acessed on July 2016.*

Gowland;, PA & Stevenson, VL 2003, 'T1: the Longitudinal Relaxation Time', in P Tofts (ed.), *Quantitative MRI of the Brain: Measuring Changes Caused by Disease*, John Wiley & Sons Ltd., ch 5, pp. 111-41.

Gowrishankar, T, Stewart, DA, Martin, GT & Weaver, JC 2004, 'Transport lattice models of heat transport in skin with spatially heterogeneous, temperature-dependent perfusion', *BioMedical Engineering OnLine*, vol. 3, no. 1, p. 1.

Gowrishankar, TR & Weaver, JC 2003, 'An approach to electrical modeling of single and multiple cells', *Proceedings of the National Academy of Sciences*, vol. 100, no. 6, pp. 3203-8.

Grill-Spector, K, Kushnir, T, Hendler, T, Edelman, S, Itzchak, Y & Malach, R 1998, 'A sequence of object-processing stages revealed by fMRI in the human occipital lobe', *Human brain mapping*, vol. 6, no. 4, pp. 316-28.

Guleyupoglu, B, Schestatsky, P, Edwards, D, Fregni, F & Bikson, M 2013, 'Classification of methods in transcranial Electrical Stimulation (tES) and evolving strategy from historical approaches to contemporary innovations', *Journal of neuroscience methods*, vol. 219, no. 2, pp. 297-311.

Hallez, H, Vanrumste, B, Van Hese, P, Delputte, S & Lemahieu, I 2008, 'Dipole estimation errors due to differences in modeling anisotropic conductivities in realistic head models for EEG source analysis', *Physics in medicine and biology*, vol. 53, no. 7, p. 1877.

Halter, RJ, Schned, AR, Heaney, JA & Hartov, A 2011, 'Passive bioelectrical properties for assessing high-and low-grade prostate adenocarcinoma', *The Prostate*, vol. 71, no. 16, pp. 1759-67.

Hasgall PA, NE, Gosselin MC, Klingenböck A, Kuster N 2014, *IT'IS Database for thermal and electromagnetic parameters of biological tissues*, 24/09/2014, <www.itis.ethz.ch/database>.

Haueisen, J, Tuch, DS, Ramon, C, Schimpf, P, Wedeen, V, George, J & Belliveau, J 2002, 'The influence of brain tissue anisotropy on human EEG and MEG', *Neuroimage*, vol. 15, no. 1, pp. 159-66.

Hewitt, A 2005, 'The effects of curvature on axial flux machine cores', University of Southern Queensland.

Huang, W-L, Hsieh, M-H & Liao, S-C 2010, 'Acoustic neuroma identified after electroconvulsive therapy in a patient with recurrent major depression and undifferentiated somatoform disorder', *The Journal of ECT*, vol. 26, no. 4, pp. 330-1.

Iacono, MI, Makris, N, Mainardi, L, Angelone, LM & Bonmassar, G 2013, 'MRI-based multiscale model for electromagnetic analysis in the human head with implanted DBS', *Computational and mathematical methods in medicine*, vol. 2013.

Iacono, MI, Neufeld, E, Akinnagbe, E, Bower, K, Wolf, J, Oikonomidis, IV, Sharma, D, Lloyd, B, Wilm, BJ & Wyss, M 2015, 'MIDA: a multimodal imaging-based detailed anatomical model of the human head and neck', *PloS one*, vol. 10, no. 4, p. e0124126.

ICBM: International Consortium for Brain Mapping, 2014, <https://ida.loni.usc.edu/>.

Jenkinson, M, Bannister, P, Brady, M & Smith, S 2002, 'Improved optimization for the robust and accurate linear registration and motion correction of brain images', *Neuroimage*, vol. 17, no. 2, pp. 825-41.

Karampatzakis, A & Samaras, T 2010, 'Numerical model of heat transfer in the human eye with consideration of fluid dynamics of the aqueous humour', *Physics in medicine and biology*, vol. 55, no. 19, p. 5653.

Kast, RE, Lewczuk, P, Halatsch, M-E, Karpel-Massler, G, Altschuler, EL & Bolwig, T 2013, 'ECT as used in psychiatry temporarily opens the blood-brain barrier: Could this be used to better deliver chemotherapy for glioblastoma', *British Journal of Medicine and Medical Research*, vol. 3, no. 4, p. 1798.

Kaus, MR, Warfield, SK, Nabavi, A, Black, PM, Jolesz, FA & Kikinis, R 2001, 'Automated segmentation of MR images of brain tumors 1', *Radiology*, vol. 218, no. 2, pp. 586-91.

Khundrakpam, BS, Shukla, VK & Roy, PK 2010, 'Thermal Conduction Tensor Imaging and Energy Flow Analysis of Brain: A Feasibility Study using MRI', *Ann. Biom. Eng.*, vol. 38, no. 10, pp. 3070-83.

Kim, D, Seo, H, Kim, H-I & Jun, SC 2014, 'Computational study on subdural cortical stimulation-the influence of the head geometry, anisotropic conductivity, and electrode configuration', *PloS one*, vol. 9, no. 9, p. e108028.

Kim, S, Tathireddy, P, Normann, R & Solzbacher, F 2007, 'Thermal impact of an active 3-D microelectrode array implanted in the brain', *IEEE T. Neural Syst Rehab. Eng.*, vol. 15, no. 4, pp. 493-501.

Kingsley, PB 2006a, 'Introduction to diffusion tensor imaging mathematics: Part I. Tensors, rotations, and eigenvectors', *Concepts in Magnetic Resonance Part A*, vol. 28, no. 2, pp. 101-22.

Kingsley, PB 2006b, 'Introduction to diffusion tensor imaging mathematics: Part III. Tensor calculation, noise, simulations, and optimization', *Concepts in Magnetic Resonance Part A*, vol. 28, no. 2, pp. 155-79.

Kingsley, PB 2006c, 'Introduction to diffusion tensor imaging mathematics: Part II. Anisotropy, diffusion-weighting factors, and gradient encoding schemes', *Concepts in Magnetic Resonance Part A*, vol. 28, no. 2, pp. 123-54.

Kirson, ED, Dbalý, V, Tovaryš, F, Vymazal, J, Soustiel, JF, Itzhaki, A, Mordechovich, D, Steinberg-Shapira, S, Gurvich, Z & Schneiderman, R 2007, 'Alternating electric fields arrest cell proliferation in animal tumor models and human brain tumors', *Proceedings of the National Academy of Sciences*, vol. 104, no. 24, pp. 10152-7.

Kostelec, PJ & Periaswamy, S 2003, 'Image registration for MRI', *Modern Signal Processing*, vol. 46, pp. 161-84.

Lee, W, Kim, T-S, Kim, AT & Lee, S 2008, '3-D diffusion tensor MRI anisotropy content-adaptive finite element head model generation for bioelectromagnetic imaging', in Engineering in Medicine and Biology Society, 2008. EMBS 2008. 30th Annual International Conference of the IEEE: *proceedings of theEngineering in Medicine and Biology Society, 2008. EMBS 2008. 30th Annual International Conference of the IEEE* IEEE, pp. 4003-6.

Lee, W, Lisanby, S, Laine, A & Peterchev, A 2016, 'Comparison of electric field strength and spatial distribution of electroconvulsive therapy and magnetic seizure therapy in a realistic human head model', *European Psychiatry*, vol. 36, pp. 55-64.

Lee, WH, Liu, Z, Mueller, BA, Lim, K & He, B 2009, 'Influence of white matter anisotropic conductivity on EEG source localization: comparison to fMRI in human primary visual cortex', *Clin. Neurophysiol.*, vol. 120, no. 12, pp. 2071-81.

Lee, WH, Deng, Z-D, Laine, AF, Lisanby, SH & Peterchev, AV 2011, 'Influence of white matter conductivity anisotropy on electric field strength induced by electroconvulsive therapy', in Engineering in Medicine and Biology Society, EMBC, IEEE: *proceedings of theEngineering in Medicine and Biology Society, EMBC, IEEE* IEEE, pp. 5473-6.

Lee, WH, Deng, Z-D, Kim, T-S, Laine, AF, Lisanby, SH & Peterchev, AV 2012, 'Regional electric field induced by electroconvulsive therapy in a realistic finite element head model: Influence of white matter anisotropic conductivity', *Neuroimage*, vol. 59, no. 3, pp. 2110-23.

Leigh Morrow, PMaCR 2016, 'DTI analysis', *Center for Advanced Brain Imaging. Available from: http://www.cabi.gatech.edu/CABI/archives/resources/dti-analysis/. Accessed on January*.

Lewis, RW, Morgan, K, Thomas, H & Seetharamu, K 1996, *The finite element method in heat transfer analysis*, John Wiley & Sons.

Lillicrap, T, Tahtali, M, Neely, A, Lueck, C & Wang, X 2012, 'Finite element modelling of heat exchange in the stroke-affected brain during therapeutic hypothermia', in 7th Australasian Congress on Applied Mechanics (ACAM 7): *proceedings of the7th Australasian Congress on Applied Mechanics (ACAM 7)* Engineers Australia, University of Adelaide, North Terrace Campus/National Committee on Applied Mechanics of Engineers Australia, p. 657.

Loo, CK, Katalinic, N, Martin, D & Schweitzer, I 2012, 'A review of ultrabrief pulse width electroconvulsive therapy', *Therapeutic advances in chronic disease*, vol. 3, no. 2, pp. 69-85.

Louis, DN, Perry, A, Reifenberger, G, von Deimling, A, Figarella-Branger, D, Cavenee, WK, Ohgaki, H, Wiestler, OD, Kleihues, P & Ellison, DW 2016, 'The 2016 World Health Organization classification of tumors of the central nervous system: A summary', *Acta neuropathologica*, vol. 131, no. 6, pp. 803-20.

Malmivuo, J & Plonsey, R 1995, *Bioelectromagnetism: principles and applications of bioelectric and biomagnetic fields*, Oxford University Press.

Marin, G, Guerin, C, Baillet, S, Garnero, L & Meunier, G 1998, 'Influence of skull anisotropy for the forward and inverse problem in EEG: simulation studies using FEM on realistic head models', *Human brain mapping*, vol. 6, no. 4, pp. 250-69.

McConnell Brain Imaging Center, MNI, McGill University. *BrainWeb: Simulated brain database.*, <<http://www.bic.mni.mcgill.ca/brainweb/>>.

McIntosh, RL, Anderson, V & McKenzie, RJ 2005, 'A numerical evaluation of SAR distribution and temperature changes around a metallic plate in the head of a RF exposed worker', *Bioelectromagnetics*, vol. 26, no. 5, pp. 377-88.

Miranda, PC, Mekonnen, A, Salvador, R & Basser, PJ 2014, 'Predicting the electric field distribution in the brain for the treatment of glioblastoma', *Physics in medicine and biology*, vol. 59, no. 15, p. 4137.

Mori, S & Zhang, J 2006, 'Principles of diffusion tensor imaging and its applications to basic neuroscience research', *Neuron*, vol. 51, no. 5, pp. 527-39.

Nadobny, J, Szimtenings, M, Diehl, D, Stetter, E, Brinker, G & Wust, P 2007, 'Evaluation of MR-induced hot spots for different temporal SAR modes using a time-dependent finite difference method with explicit temperature gradient treatment', *Biomedical Engineering, IEEE Transactions on*, vol. 54, no. 10, pp. 1837-50.

NIMH, NIoMH 2016, *Brain Stimulation Therapies*, viewed 17 April 2014, <http://www.nimh.nih.gov/health/topics/brain-stimulation-therapies/brain-stimulation-therapies.shtml>.

Njau, S, Joshi, SH, Espinoza, R, Leaver, AM, Vasavada, M, Marquina, A, Woods, RP & Narr, KL 2016, 'Neurochemical correlates of rapid treatment response to electroconvulsive therapy in patients with major depression', *Journal of psychiatry & neuroscience: JPN*, vol. 41, no. 5, p. 150177.

Oostendorp, TF, Hengeveld, YA, Wolters, CH, Stinstra, J, van Elswijk, G & Stegeman, DF 2008, 'Modeling transcranial DC stimulation', in Engineering in Medicine and Biology Society, 2008. EMBS 2008. 30th Annual International Conference of the IEEE: *proceedings of theEngineering in Medicine and Biology Society, 2008. EMBS 2008. 30th Annual International Conference of the IEEE* IEEE, pp. 4226-9.

Pennes, HH 1948, 'Analysis of tissue and arterial blood temperatures in the resting human forearm', *J. Appl. Physiol.*, vol. 1, no. 2, pp. 93-122.

Peterchev, AV, Rosa, MA, Deng, Z-D, Prudic, J & Lisanby, SH 2010, 'ECT stimulus parameters: rethinking dosage', *The Journal of ECT*, vol. 26, no. 3, pp. 159-74.

Peterchev, AV, Wagner, TA, Miranda, PC, Nitsche, MA, Paulus, W, Lisanby, SH, Pascual-Leone, A & Bikson, M 2012, 'Fundamentals of transcranial electric and magnetic stimulation dose: definition, selection, and reporting practices', *Brain stimulation*, vol. 5, no. 4, pp. 435-53.

Positano, V 2005, 'Image Registration in MRI', in LLVPMF Santarelli (ed.), *Advanced Image Processing in Magnetic Resonance Imaging*, Taylor & Francis Group, LLC, ch 7, pp. 189-221.

Prishvin, M, Manukyan, L & Zaridze, R 2009, 'Vascular structure model for improved numerical simulation of heat transfer in human tissue', in Electromagnetic Compatibility, 2009 20th International Zurich Symposium on: *proceedings of theElectromagnetic Compatibility, 2009 20th International Zurich Symposium on* IEEE, pp. 261-4.

Pujol, S, Wells, W, Pierpaoli, C, Brun, C, Gee, J, Cheng, G, Vemuri, B, Commowick, O, Prima, S & Stamm, A 2015, 'The DTI challenge: toward standardized evaluation of diffusion tensor imaging tractography for neurosurgery', *Journal of Neuroimaging*, vol. 25, no. 6, pp. 875-82.

Rorden, C, Karnath, H & Bonilha, L 2016, 'MRIcron dicom to nifti converter', *Neuroimaging Informatics Tools and Resources Clearinghouse (NITRC). Available from: http://www. nitrc.org/projects/mricron. Accessed on February*, vol. 7.

Rosa, MA & Lisanby, SH 2012, 'Somatic treatments for mood disorders', *Neuropsychopharmacol.*, vol. 37, no. 1, pp. 102-16.

Rush, S & Driscoll, DA 1968, 'Current distribution in the brain from surface electrodes', *Anesthesia & Analgesia*, vol. 47, no. 6, pp. 717-23.

Rush, S & Driscoll, DA 1969, 'EEG electrode sensitivity-an application of reciprocity', *IEEE T. Biom. Eng.*, no. 1, pp. 15-22.

Sackeim, HA, Long, J, Luber, B, Moeller, JR, Prohovnik, I, Devanand, D & Nobler, MS 1994, 'Physical properties and quantification of the ECT stimulus: I. Basic principles', *The Journal of ECT*, vol. 10, no. 2, pp. 93-123.

Sadleir, RJ, Vannorsdall, TD, Schretlen, DJ & Gordon, B 2010, 'Transcranial direct current stimulation (tDCS) in a realistic head model', *Neuroimage*, vol. 51, no. 4, pp. 1310-8.

Salerian, AJ, Saleri, NG & Salerian, JA 2008, 'Brain temperature may influence mood: a hypothesis', *Medical hypotheses*, vol. 70, no. 3, pp. 497-500.

Salu, Y, Cohen, LG, Rose, D, Sxato, S, Kufta, C & Hallett, M 1990, 'An improved method for localizing electric brain dipoles', *Biomedical Engineering, IEEE Transactions on*, vol. 37, no. 7, pp. 699-705.

Schlaepfer, TE, Cohen, MX, Frick, C, Kosel, M, Brodesser, D, Axmacher, N, Joe, AY, Kreft, M, Lenartz, D & Sturm, V 2008, 'Deep brain stimulation to reward circuitry alleviates anhedonia in refractory major depression', *Neuropsychopharmacology*, vol. 33, no. 2, pp. 368-77.

Scott, J 1988, 'A finite element model of heat transport in the human eye', *Physics in medicine and biology*, vol. 33, no. 2, p. 227.

Seo, H, Kim, D & Jun, SC 2015, 'Computational Study of Subdural Cortical Stimulation: Effects of Simulating Anisotropic Conductivity on Activation of Cortical Neurons', *PloS one*, vol. 10, no. 6, p. e0128590.

Shahid, S, Wen, P & Ahfock, T 2011, 'Effect of fat and muscle tissue conductivity on cortical currents-a tDCS study', in Complex Medical Engineering (CME), 2011 IEEE/ICME International Conference on: *proceedings of theComplex Medical Engineering (CME), 2011 IEEE/ICME International Conference on* IEEE, pp. 211-5.

Shahid, S, Wen, P & Ahfock, T 2012, 'Effects of model complexity and tissue anisotropic conductivity on cortical modulation during transcranial direct current stimulation', *IET Science, Measurement & Technology*, vol. 6, no. 6, pp. 464-73.

Shahid, S, Wen, P & Ahfock, T 2013, 'Numerical investigation of white matter anisotropic conductivity in defining current distribution under tDCS', *Comput. Meth. Prog. Biomed.*, vol. 109, no. 1, pp. 48-64.

Shahid, SS 2013, 'Numerical Investigation of transcranial Direct Current Stimulation on Cortical Modulation', University of Southern Queensland, Australia.

Shahid, SS, Song, B, Salman, H, de Oliveira, MM & Wen, P 2015, 'Use of electric field orientation as an index for estimating the contribution of model complexity in transcranial direct current stimulation forward head model development', *IET Science, Measurement & Technology*, vol. 9, no. 5, pp. 596-605.

Shammi, P & Stuss, DT 1999, 'Humour appreciation: a role of the right frontal lobe', *Brain*, vol. 122, no. 4, pp. 657-66.

Silay, KM, Dehollain, C & Declercq, M 2008, 'Numerical analysis of temperature elevation in the head due to power dissipation in a cortical implant', in Engineering in Medicine and Biology Society, 2008. EMBS 2008. 30th Annual International Conference of the IEEE: *proceedings of theEngineering in Medicine and Biology Society, 2008. EMBS 2008. 30th Annual International Conference of the IEEE* IEEE, pp. 951-6.

Smith, SM 2002, 'Fast robust automated brain extraction', *Human brain mapping*, vol. 17, no. 3, pp. 143-55.

Smith, SM, Jenkinson, M, Woolrich, MW, Beckmann, CF, Behrens, TE, Johansen-Berg, H, Bannister, PR, De Luca, M, Drobnjak, I & Flitney, DE 2004, 'Advances in functional and structural MR image analysis and implementation as FSL', *Neuroimage*, vol. 23, pp. S208-S19.

Soares, J, Marques, P, Alves, V & Sousa, N 2013, 'A hitchhiker's guide to diffusion tensor imaging', *Frontiers in neuroscience*, vol. 7, p. 31.

Song, B, Wen, P, Ahfock, T & Li, Y 2016, 'Numeric Investigation of Brain Tumor Influence on the Current Distributions During Transcranial Direct Current Stimulation', *Biomedical Engineering, IEEE Transactions on*, vol. 63, no. 1, pp. 176-87.

Standring, S 2015, *Gray's anatomy: the anatomical basis of clinical practice,* Elsevier Health Sciences.

Suh, HS, Lee, WH & Kim, T-S 2012, 'Influence of anisotropic conductivity in the skull and white matter on transcranial direct current stimulation via an anatomically realistic finite element head model', *Physics in medicine and biology*, vol. 57, no. 21, pp. 6961-80.

Swartz, CM 1989, 'Safety and ECT stimulus electrodes: I. Heat liberation at the electrode-skin interface', *J. ECT*, vol. 5, no. 2, pp. 171-5.

Thielscher, A, Opitz, A & Windhoff, M 2011, 'Impact of the gyral geometry on the electric field induced by transcranial magnetic stimulation', *Neuroimage*, vol. 54, no. 1, pp. 234-43.

Tofts, PS 2003, 'PD: Proton Density of Tissue Water', in P Tofts (ed.), *Quantitative MRI of the Brain: Measuring Changes Caused by Disease*, John Wiley & Sons Ltd., ch 4, pp. 85-109.

Trembly, BS & Keates, RH 1991, 'Combined microwave heating and surface cooling of the cornea', *Biomedical Engineering, IEEE Transactions on*, vol. 38, no. 1, pp. 85-91.

Tromp, D, 2015, 'Diffusion Imaging', <http://www.diffusion-imaging.com/2015/10/dti-tutorial-1-from-scanner-to-tensor.html>.

Trujillo, M & Berjano, E 2013, 'Review of the mathematical functions used to model the temperature dependence of electrical and thermal conductivities of biological tissue in radiofrequency ablation', *Int. J. Hyperth.*, vol. 29, no. 6, pp. 590-7.

Utz, KS, Dimova, V, Oppenländer, K & Kerkhoff, G 2010, 'Electrified minds: transcranial direct current stimulation (tDCS) and galvanic vestibular stimulation (GVS) as methods of non-invasive brain stimulation in neuropsychology—a review of current data and future implications', *Neuropsychologia*, vol. 48, no. 10, pp. 2789-810.

van den Broek, SP, Reinders, F, Donderwinkel, M & Peters, M 1998, 'Volume conduction effects in EEG and MEG', *Electroencephalography and clinical neurophysiology*, vol. 106, no. 6, pp. 522-34.

Van Leeuwen, GM, Kotte, AN & Lagendijk, JJ 1998, 'A flexible algorithm for construction of 3-D vessel networks for use in thermal modeling', *IEEE transactions on biomedical engineering*, vol. 45, no. 5, pp. 596-604.

Van Leeuwen, GM, Hand, JW, Lagendijk, JJ, Azzopardi, DV & Edwards, AD 2000, 'Numerical modeling of temperature distributions within the neonatal head', *Pediatric Research*, vol. 48, no. 3, pp. 351-6.

Van Lier, A, Hoogduin, J, Polders, D, Boer, V, Hendrikse, J, Robe, P, Woerdeman, P, Lagendijk, J, Luijten, P & van den Berg, C 2011, 'Electrical conductivity imaging of brain tumours', in Proc. of ISMRM: *proceedings of theProc. of ISMRM* p. 4464.

Vilanova, A, Zhang, S, Kindlmann, G & Laidlaw, D 2006, 'An introduction to visualization of diffusion tensor imaging and its applications', in *Visualization and Processing of Tensor Fields*, Springer, pp. 121-53.

Wagner, T, Valero-Cabre, A & Pascual-Leone, A 2007, 'Noninvasive human brain stimulation', *Annu. Rev. Biomed. Eng.*, vol. 9, pp. 527-65.

Wang, H, Wang, B, Normoyle, KP, Jackson, K, Spitler, K, Sharrock, MF, Miller, CM, Best, C, Llano, D & Du, R 2014, 'Brain temperature and its fundamental properties: a review for clinical neuroscientists', *Frontiers in neuroscience*, vol. 8, p. 307.

Wang, Y, Haynor, DR & Kim, Y 2001, 'An investigation of the importance of myocardial anisotropy in finite-element modeling of the heart: methodology and application to the estimation of defibrillation efficacy', *IEEE transactions on biomedical engineering*, vol. 48, no. 12, pp. 1377-89.

Warfield, SK, Kaus, M, Jolesz, FA & Kikinis, R 2000, 'Adaptive, template moderated, spatially varying statistical classification', *Medical image analysis*, vol. 4, no. 1, pp. 43-55.

Watanabe, H, Yamazaki, N, Kobayashi, Y, Miyashita, T, Hashizume, M & Fujie, MG 2010, 'Temperature dependence of thermal conductivity of liver based on various experiments and a numerical simulation for RF ablation', in EMBC-IEEE Ann. Int. Conf. IEEE *proceedings of theEMBC-IEEE Ann. Int. Conf. IEEE* IEEE, pp. 3222-8.

Weiner, RD 2002, *The practice of electroconvulsive therapy: Recommendations for treatment, training, and privileging: A Task Force Report of the American Psychiatric Association*, Second edn, American Psychiatric Association.

Wenger, C, Salvador, R, Basser, PJ & Miranda, PC 2015, 'The electric field distribution in the brain during TTFields therapy and its dependence on tissue dielectric properties and anatomy: a computational study', *Physics in medicine and biology*, vol. 60, no. 18, p. 7339.

Wolters, C, Anwander, A, Tricoche, X, Weinstein, D, Koch, M & MacLeod, R 2006, 'Influence of tissue conductivity anisotropy on EEG/MEG field and return current computation in a realistic head model: a simulation and visualization study using high-resolution finite element modeling', *Neuroimage*, vol. 30, no. 3, pp. 813-26.

Wong, ET, Lok, E & Swanson, KD 2015, 'An evidence-based review of alternating electric fields therapy for malignant gliomas', *Current treatment options in oncology*, vol. 16, no. 8, pp. 1-11.

Yacoob, SM & Hassan, NS 2012, 'FDTD analysis of a noninvasive hyperthermia system for brain tumors', *Biomedical engineering online*, vol. 11, no. 1, p. 1.

Zaridze, R, Gritsenko, N, Kajaia, G, Nikolaeva, E, Razmadze, A, Shoshiashvili, L, Bijamov, A, Bit-Babik, G & Faraone, A 2005, 'Electro-thermal computational suit for investigation of RF power absorption and associated temperature change in human body', in Antennas and Propagation Society International Symposium, 2005 IEEE: *proceedings of theAntennas and Propagation Society International Symposium, 2005 IEEE* IEEE, pp. 796-9.

Zhou, H & van Oosterom, A 1992, 'Computation of the potential distribution in a four-layer anisotropic concentric spherical volume conductor', *Biomedical Engineering, IEEE Transactions on*, vol. 39, no. 2, pp. 154-8.

Zou, Y & Guo, Z 2003, 'A review of electrical impedance techniques for breast cancer detection', *Medical engineering & physics*, vol. 25, no. 2, pp. 79-90.

APPENDIX I: BIO-HEAT TRANSFER STUDY USING RESISTIVE-CAPACITIVE NETWORK MODEL

A not so common technique for thermo-electrical analysis is the coupled network method. In this appendix, the bio-heat transfer equation coupled with the Laplace equation is evaluated through a resistive-capacitive network model. Same parameters and configurations were used to solve the problem, using electric circuit techniques.

I.1. Introduction

The coupled network method uses theory and elements from electric circuit to define a model. This is a different approach to system modelling, which can be found in different application areas, such as in electromagnetic analysis (Hewitt 2005), heat conduction and nanosecond pulsed electric field. Gowrishankar et al. (2004) modelled the spatially heterogeneous blood perfusion temperature-dependent transport of heat conduction through a transport lattice approach. In the area of nanosecond pulsed electric field, Esser et al. (2009) modelled rabbit liver tissue as a multicellular model of irregular cells and considered their electrical and thermal responses. The models were generated through the method of transport lattice and the aim was to treat solid tumors. Apart from that, Gowrishankar and Weaver (2003) developed a transport lattice method to understand the effects of electric fields on single and multiple cells.

The nature of a coupled network forces one physics approach to influence an other, then reverse this process repeatedly. In the present work, a resistive-capacitive network is developed, where the electrical physics influences the thermal. However, there is no influence in return to the electrical physics, due to the small variations in temperature.

In this appendix, the ECT temperature rise using the resistive-capacitive network method is investigated. Firstly, a simplified 1D thermal resistive-capacitive network (RCN_1D) is built. Then, for comparison, a 2D FEM axisymmetric model (AXM_2D) is also modelled. In these models, only the BHTE equation was analysed. Afterwards, a 3D five layers spherical thermo-electrical resistive-capacitive network (RCN_3D) model is developed and evaluated. The resistive-capacitive network models help with the understanding of temperature and electric fields but also with the much faster generation of results. They can also serve as a part-validation for the results from FEM models.

I.2. Methods

This section will cover the design of the head model in a resistive-capacitive network manner and finite element method, considering the equations for modelling, configurations, parameters, initial and boundary conditions.

i. Head Model Design

Two different types of model were considered in this section. A resistive-capacitive network model was designed in Matlab through the method of finite difference method (FDM). Then, equivalent models were simulated in COMSOL through finite element methods (FEM).

APPENDIX I: BIO-HEAT TRANSFER STUDY USING RESISTIVE-CAPACITIVE NETWORK MODEL

1. Resistive-Capacitive Network Model

In the resistive-capacitive approach, circuit elements are used to solve the model. In this way, the domains are represented in terms of resistors, capacitors and sources elements.

The human head model for this work is also developed using this approach. The Matlab software is used to develop a script and Simulink generates some of the results. This method is solved through FDM and this type of analysis assists in the understanding of electrical and thermal behaviour through the layers.

The BHTE is solved using components from an electrical circuit. Kirchhoff's laws are applied to solve the circuit. In this case, tension (V) is equivalent to temperature (T), resistance (R) is equivalent to thermal conductivity (*k*), capacitance as thermal capacity (*c*), and heat generation is represented as current source.

To begin with, a linear problem is created, with one node being considered for each tissue type (scalp, skull, CSF, GM and WM). This is the model RCN_1D. It is represented in Figure I.1 and the schematic circuit diagram is shown in Figure I.2.

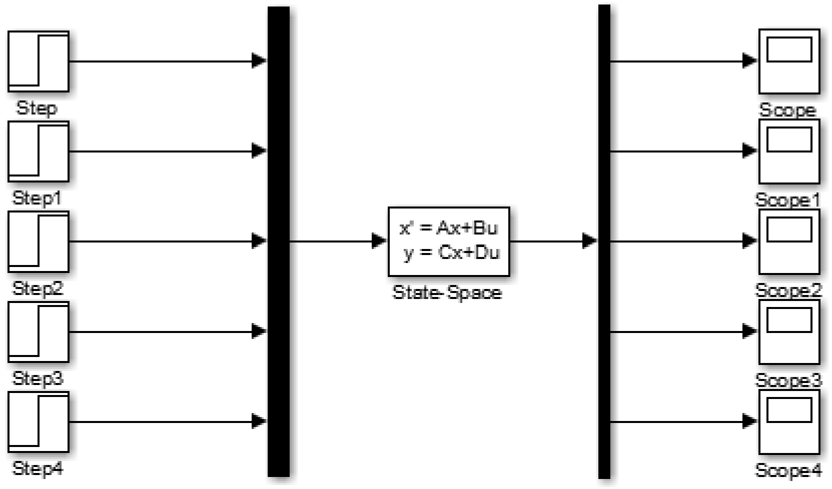

Figure I.1. Simulink circuit for 1D resistive network model.

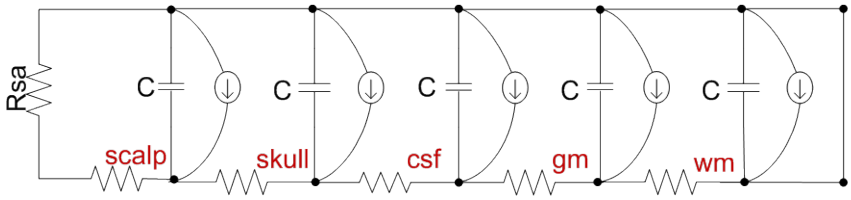

Figure I.2. Schematic circuit diagram for RCN_1D model.

Later on, multiple nodes and layers are assumed, simulating a spherical model (model RCN_3D). Thereby, each layer contains three sublayers; each sublayer contains 361 nodes; which gives a total of 5,415 elements in the entire model. Each layer represents one of the five tissues of the head. The thermo-electrical nodes are considered at the centroid of the element, as shown in Figure I.3 and Figure I.4.

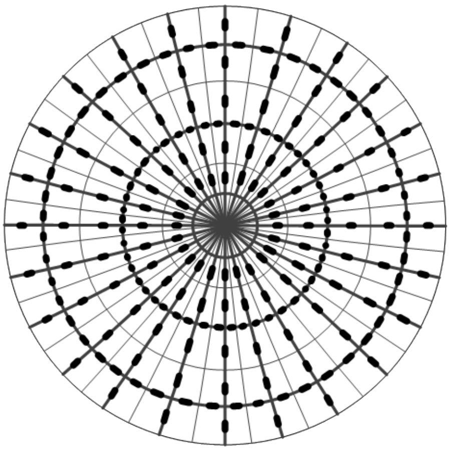

Figure I.3. Core discretization slice of spherical resistive-capacitive network model.

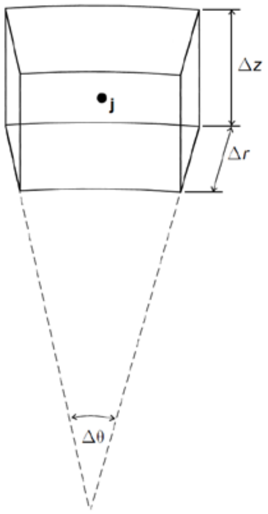

Figure I.4. Shape of element and positioning of node at centroid (Hewitt 2005).

Figure I.5 shows a simplified schematic of the 3D circuit, where only one node from each sublayer is shown.

If electric potential and temperature are independent of azimuthal and polar angles, then the 3D model in Figure I.3 and Figure I.4 can be simplified to the model shown in Figure I.5. The equation below defines the BHTE for the circuit, where the sub-script ‘i’ denotes the tissue layer.

$$\boldsymbol{c_{tissue_i}\frac{dT_{tissue_i}}{dt} = \left(T_{tissue_{i+1}} - T_{tissue_i}\right)\Big/\left(\frac{R_{tissue_{i+1}} + R_{tissue_i}}{2}\right) - \left(T_{tissue_i} - T_{tissue_{i-1}}\right)\Big/\left(\frac{R_{tissue_i}+R_{tissue_{i-1}}}{2}\right) + H_{tissue_i}} \quad (22)$$

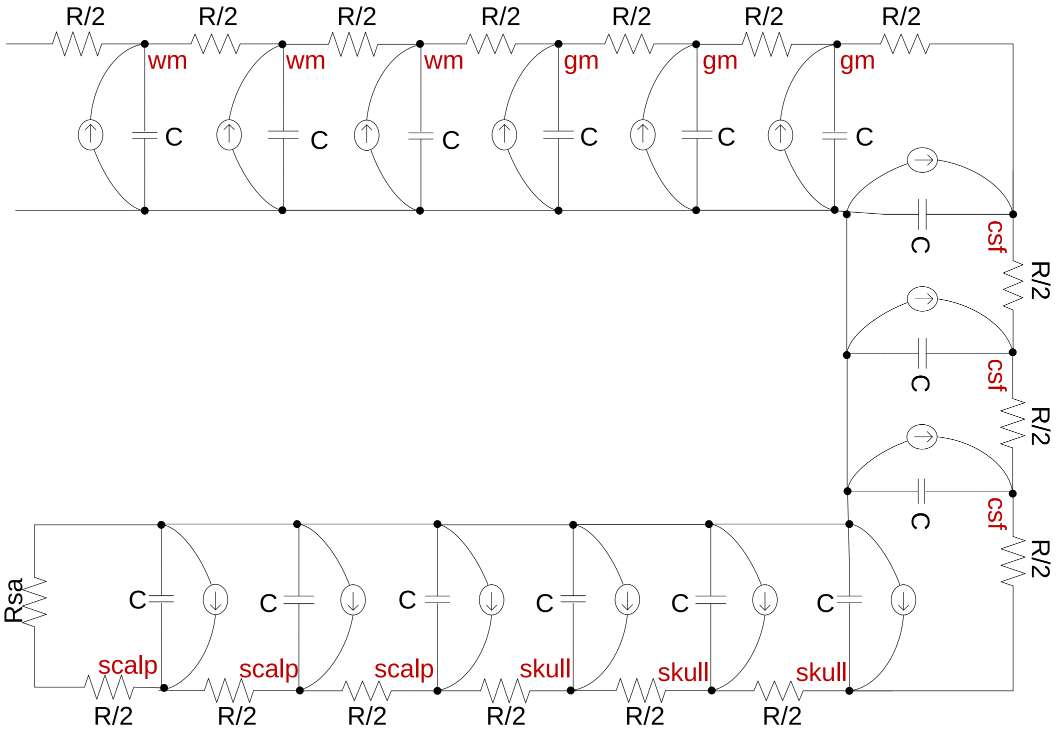

Figure I.5. Simplified schematic of the resistive network model, RCN_03.

State equations are used to represent and enable an analysis of the problem. At any point of the model, the solution is given by: $T = T_\infty + A_1 e^{-t/\tau_1} + \cdots + A_n e^{-t/\tau_n}$, where τ_i is a time constant.

In this type of model, the electrodes are considered to be placed directly over the head. Therefore, the electrical stimulation is applied over five nodes, in a cross shape. The distance considered is equivalent to the one used during ECT, which could fit the present model.

2. Finite Element Model

For comparison with the resistive-capacitive models, equivalent FEM models are created. A 2D axisymmetric model (AXM_2D) is developed in COMSOL, which is used to directly compare with RCN_1D. Later, the 3D spherical FEM (FEM_3D) is modelled in COMSOL. This model also consists of five tissue layers with dimensions and configurations equivalent to RCN_3D. The model FEM_3D will be directly compared with RCN_3D.

For the models designed in COMSOL, the mesh is generated using FEM and the calculation of such problems is solved using the same method.

Table I.1 summarizes the models used in this section.

Table I.1. Summary of the human head models considered in Appendix I.

MODEL	ACRONYM	SOFTWARE MODELLED	PHYSICS - METHOD	FUNCTION
1D resistive-capacitive network model	RCN_1D	Matlab + Simulink 5 layers – 5 nodes	Thermal only – FDM	Assist in understanding of thermal behaviour through tissue layers
2D axisymmetric model	AXM_2D	COMSOL	Thermal only – FEM	Comparison with RCN_1D
3D resistive-capacitive network model	RCN_3D	Matlab 5 layers – 5415 nodes	Thermal + electrical – FDM	Assist in understanding of thermal and electrical behaviour through tissue layers
3D FEM spherical model	FEM_3D	COMSOL 5 layers	Thermal + electrical – FEM	Comparison with RCN_3D

3. Model Configurations and Conductivity Assignment

In a similar way, each layer represents one type of head tissue. The diameter of the external layer for the spherical models is considered to be 21 cm; and the thickness of scalp, skull, CSF and GM are 1 cm. The assumed electrical and thermophysical properties (Datta, Elwassif & Bikson 2009; Fiala, Lomas & Stohrer 1999; Hasgall PA 2014) of these tissues are given in Table I.2.

Table I.2. Electrical and thermophysical properties of head tissues.

	k (W/(m.K))	***σ*** (S/m)	***ρ*** (Kg/m3)	***cp*** J/(Kg.K)	***Qm*** (W/m3)	***ωb*** (1/s)
Scalp	0.39	0.465	1125	3150	363	0.00143
Skull	1.15	0.0132	1850	1300	70	1.43e-4
CSF	0.60	1.654	1000	4200	0	0
GM	0.565	0.33	1035.5	3680	16229	1.3289e-2
WM	0.503	0.65	1027.4	3600	4517.9	3.6956e-3

ii. Heat Transfer Model

For the RCN_1D and the AXM_2D models, only thermal physics is considered. In these cases, the BHTE (Pennes 1948) (Equation 2) alone is applied. The state space equations shown in Figure I.1 represent the BHTE. The equations are defined equivalently to the one shown in Equation 22. In this case, parameter ‘A’ is the state space matrix, defined for each node/tissue and its neighbors in terms of resistance and capacitance. The thermal sources of each node/tissue are defined at the parameter ‘u’. The parameters ‘B’ and ‘C’ are identity matrices, while ‘D’ is the null matrix.

For the RCN_3D and FEM_3D models, the physics applied involves heat transfer and electrical potential simultaneously. The bio-heat transfer equation is combined to Laplace equation (Datta, Elwassif & Bikson 2009; Elwassif et al. 2006) (Equation 4), as described in Section 2.

$$\rho c\frac{\partial T}{\partial t} = \nabla(k\nabla T) + \omega\rho_b c_b\left(T_a\text{-}T\right) + Q_m + \nabla|\sigma\nabla V|\,. \qquad (4)$$

Time dependent domain is applied for the thermal physics. The range simulated varies from 0 to 8 s (ECT safety values); but also, for some models an extrapolation of these values is considered, modelling up to 3000 s.

In the thermo-electrical models, the electrodes are also modelled. The configurations are the conventional BL ECT, as described in Section 3.

iii. Initial and Boundary Conditions

Initial and boundary conditions are assigned for the thermal and electrical physics to formulate the problem.

For the thermal physics:

- External BC: governed by heat flux ($-k \cdot \frac{\partial T}{\partial n} = h \cdot (T_{amb} - T)$, Equation 7), where h is assigned as $4\ W/m^2.^oC$; and T_{amb} as $24\ ^oC$.
- Internal BC, interfaces between two layers: conduction.
- Initial temperature: $36.7\ ^oC$.

For the electrical physics:

- Exposed BC: electrically insulated (Neumann BC, $n \cdot (\sigma \nabla V) = 0$).
- Inner BC, between regions of different tissues: continuity.

For the exposed surfaces of electrodes:

- Cathode: Dirichlet ($V = 0$ volts) BC.
- Anode: Dirichlet ($V = V_0$ volts) BC., where V_0 is the input applied to the active electrode, equivalent to the rms value of a biphasic brief pulse of 120 Hz, 1 millisecond width pulse, and the amplitude equivalent to 800 mA total current injection.

I.3. Simulation and Results

The simulations are developed and designed to evaluate these models and their functions. It starts with the simplest RCN_1D and AXM_2D models, then the RCN_3D and the equivalent FEM_3D when the BL electrode stimulation is applied.

i. Thermal Physics Behaviour

These were the most simplified models, where only thermal physics is considered. The intention here is to analyse the temperature changes in each tissue layer, during an extended period of time, to compare the resistive-capacitive network model and FEM models. In a step-by-step fashion, the interpretation of more complex models is made easier, when joining electrical physics and considering realistic geometries in the following sections.

The models are simulated for longer than the normal ECT period to investigate the process thoroughly. Here, $t = 1000$ s is considered. Graphs of temperature against time, for each tissue layer, are shown in Figure I.6 and Figure I.7, for the models RCN_1D and the equivalent AXM_2D, respectively.

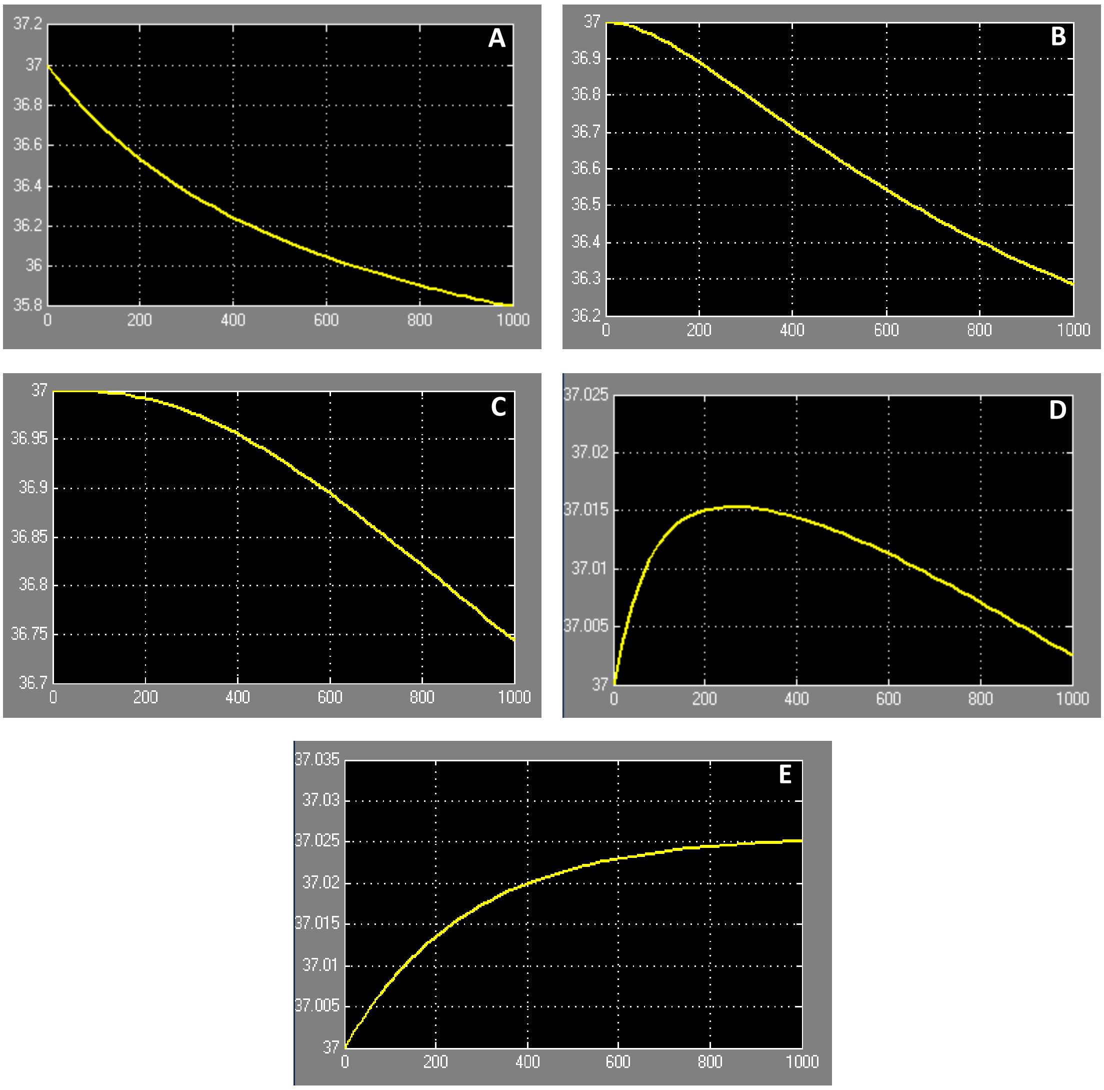

Figure I.6. Temperature behaviour versus time, during 1000 s, model RCN_1D, for layers of (a) scalp, (b) skull, (c) CSF, (d) GM and (e) WM.

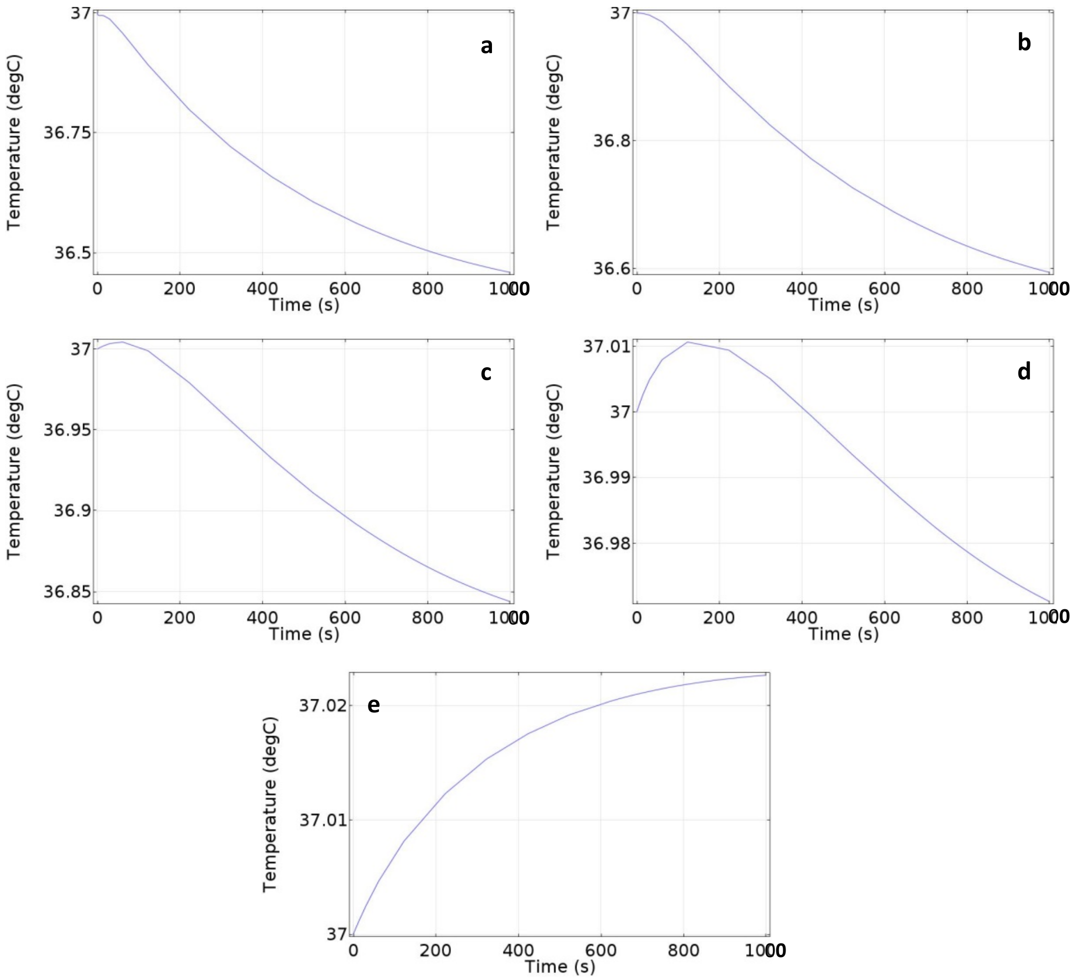

Figure I.7. Temperature versus time, during 1000 s, for COMSOL 2D sphere thermal model (AXM_2D); results for layers (a) scalp, (b) skull, (c) CSF, (d) GM and (e) WM.

In Figure I.6 and Figure I.7, it can be seen that the temperature at both scalp and skull layers decreases, due to ambient convection; at CSF, the temperature correlates with blood temperature, while at GM and WM the temperature stays constant, with a slight increase due to the high metabolic heat.

It is observed that the results from FDM and FEM are remarkably similar to each other. However, there are still some small variations. This could be due to the refinement of the models. The FDM model considered here is an extremely simplified one, with only one node per layer; whereas the FEM model, while still simplistic, has thousands more nodes than RCN_1D.

The above simulations are a starting point to understand the temperature behaviour of the human head at each layer. It helps to understand and to interpret the results in more difficult geometries, as the realistic geometries seen in the previous chapters.

ii. 3D Resistive-Capacitive Network Models

In the models considered here, both thermal and electrical physics are applied. Also, the electrodes receive an input equivalent to 800 mA of electrical stimulation.

With the 3D spherical resistive-capacitive network modelled (RCN_3D model), it is possible to find out when the system will reach a stationary state. For this purpose, the eigenvalues and the eigenvectors of the system are calculated and compared with the final temperature. Once they have an equivalent result, that means the system has reached a steady state. This happens at approximately t = 3000 s, as shown in Figure I.8a.

As can be seen from this figure, due to the extended time and the electrical stimulation, the temperature at the scalp layer is extremely high; afterwards, the temperature starts to drop as long as it penetrates deeper into the tissues, and also because of variation in the conductivities between tissues. Of course, this time period is not realistic for ECT practices; however, it is important for understanding the behaviour of the model over extended periods.

For better understanding, as an example, a comparison by using two extra different time frames. In Figure I.8b-c, the behaviours at times 1000 s and 8 s are seen. The latter is a realistic time for ECT. It is shown that the two curves, in each case, are not equivalent; which means they did not reach a steady-state. Also, the quicker the time frame, the further it will be to reach a stationary state.

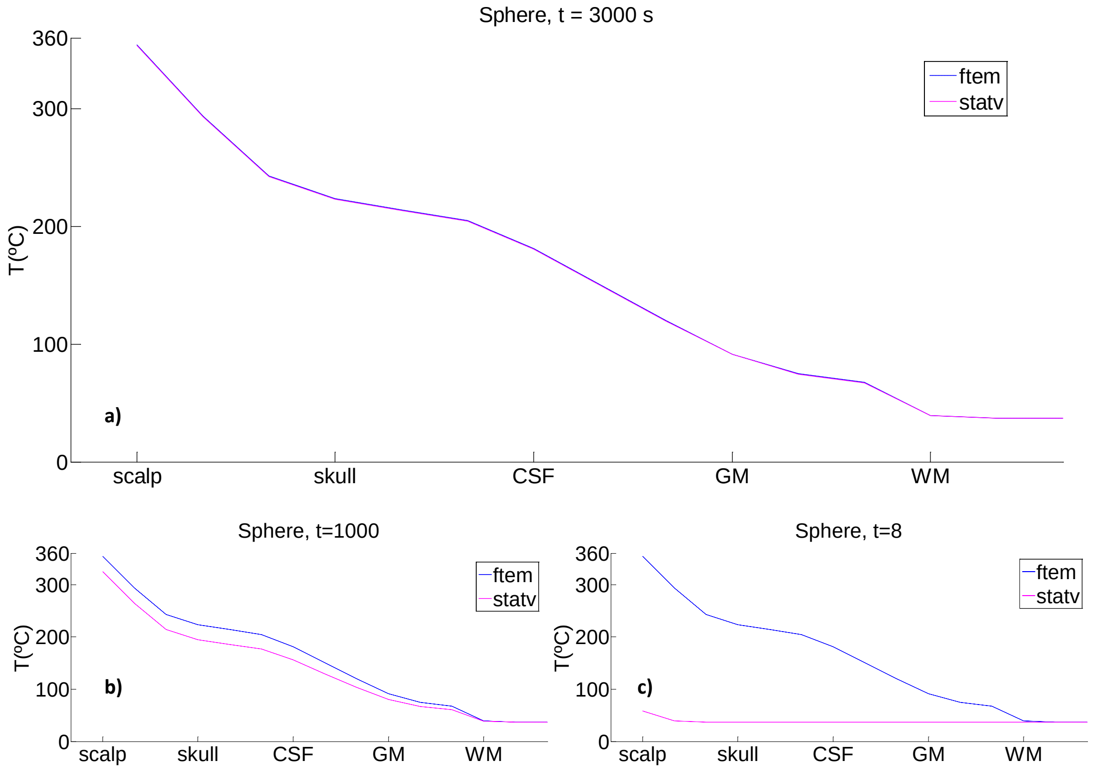

Figure I.8. Final temperature (ftem) compared with absolute temperature (statv) along radial line of 3D resistive-capacitive network model at (a) t = 3000 s, time to reach a steady state; (b) t = 1000 s; and (c) t = 8 s.

Furthermore, it is also a way to evaluate and select a suitable time for ECT practice. Figure I.9a shows the estimation of temperature for cases where the stimulation is at BL ECT position; this radial line starts from the scalp (in the middle of the electrode) and ends at WM (at the centre of the sphere) during the time of 8 s period. The equivalent model is simulated using COMSOL (FEM_3D model). In this case, a 3D five layers spherical head model is considered with the same tissue parameters and input stimulations. The results can be visualized in Figure I.9b.

The starting point of this radial line is in the electrode region. As soon as it reaches the scalp, the temperature starts to increase. When it reaches the skull, it keeps increasing, due to the high conductivity in this layer. However, the low thermal time constant does not allow high temperature to propagate, therefore the temperature starts to drop and keeps on dropping when in CSF, due to its low conductivity. The high metabolic heat at GM, generates a slight increase in temperature; but the blood perfusion maintains the equilibrium. Finally, at WM, the equilibrium continues.

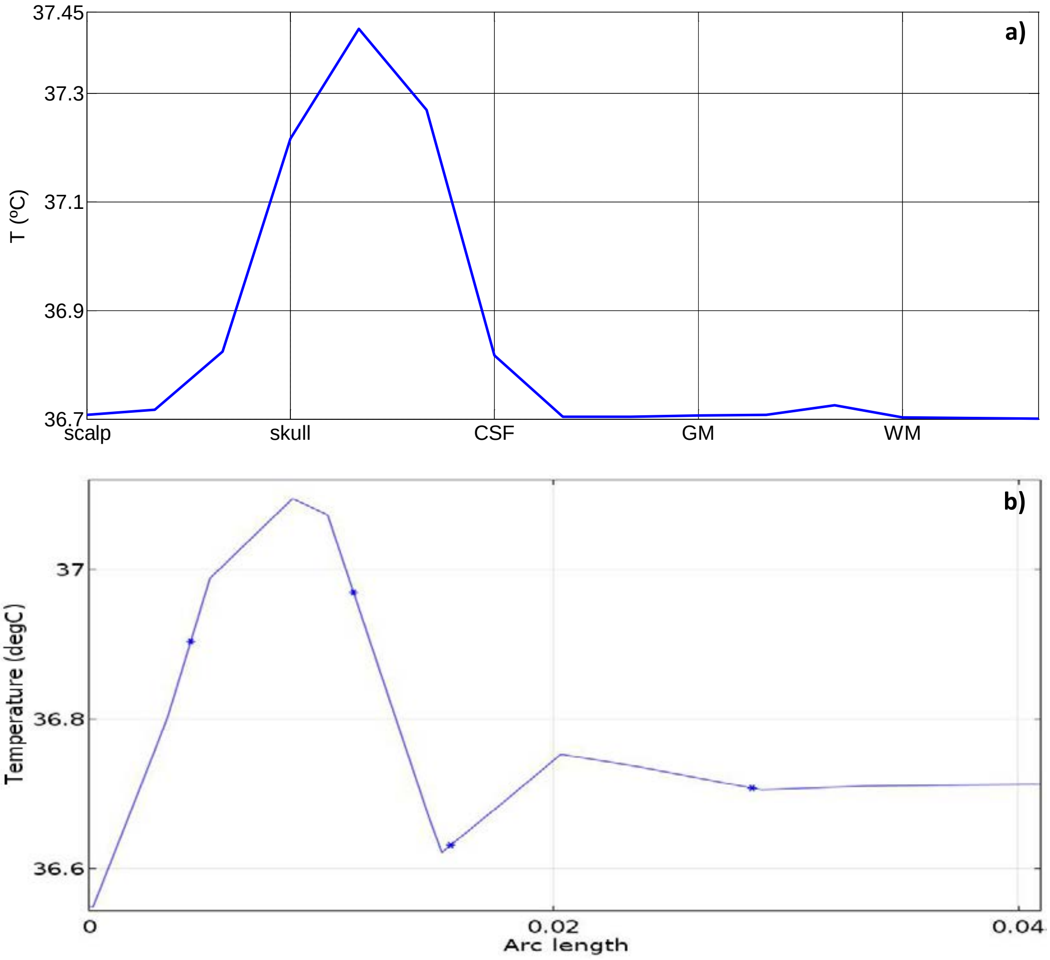

Figure I.9. Estimation of temperature through a radial line of (a) 3D resistive network (RCN_3D) and (b) equivalent COMSOL 3D spherical model (FEM_3D); BL ECT stimulation at t = 8 s.

I.4. Discussions

i. Comparison between Resistive Network and FEM Models

Modelling using thermal physics only and using a longer period of time helps to understand the behaviour of temperature in each tissue layer, due to the thermophysical characteristics. As observed in Figure I.6 and Figure I.7, the temperature at both scalp and skull layers starts to decrease, due to convection to ambient; at CSF the temperature goes up to blood temperature, while at GM and WM the temperature remains constant.

The use of thermal results only supports the understanding for the thermo-electrical stimulation models. When considering electrical stimulation, one would expect an increase in temperature. This rise follows an equivalent pattern of thermal only results. As demonstrated in Figure I.9, the temperature increases from scalp to skull layers. This rise is due to the electrical stimulation and the high thermal conductivity value of the skull. Correspondingly, a decrease occurs from skull to CSF. This drop happens due to the small period of time stimulated, only 8 seconds. The thermal time constant is not achieved during this short period and the electrical heat does not propagate to deeper tissues. Therefore, the temperature starts to stabilize to blood temperature. At GM, a small lump appears, due to the high metabolic heat at this layer. But this is stabilized with blood perfusion; and the stability maintains at WM layer.

These similar results are obtained using both the 3D resistive-capacitive network, RCN_3D, and the FEM model, FEM_3D. Therefore, the resistive-capacitive network model, using finitely different methods, works as a part-validation to the FEM model. The advantage of the RCN models is that the analysis occurs over an extended period of time, consuming only seconds for computation. Therefore, results can be obtained and interpreted more quickly. However, for more sophisticated and realistic geometries and inclusion of anisotropy conductivity, this method is not viable.

ii. Steady-State

ECT electrical stimulation is measured in the range of seconds of time (Weiner 2002). Therefore, the thermo-electrical models also need to be simulated during this short period. At this point in time, it is insufficient for the system to reach a thermal stationary state. In order to better understand the behaviour of temperature distribution and to make sure the developed system provides suitable results, steady-state is calculated using the RCN_3D model, as seen in Figure I.8, although this is unrealistic for ECT purposes, for which, the eigenvalues and eigenvectors of the system have been calculated. From there, it is possible to find the thermal time constant, and when the model reaches its stationary state. This is another advantage of developing the resistive-capacitive network models, as the FEM models take too long to run and it will be harder to find the steady state time.

I.5. Conclusions

With the RC network models, it is also possible to simulate the rise in temperature due to ECT electrical stimulation. The advantages of these models are the quicker run times and faster results processing; the possibility of finding the stationary state; and to partially validate the FEM models. However, there are also some disadvantages with the RC models, as it is harder to simulate anisotropic structures and more complex and realistic geometries. Meanwhile, it is well known how difficult it is to validate the simulations with human head models in tES and the RC developed here works as a part-validation for these models.